AN ABSTRACT OF THE DISSERTATION OF

Kai Zhan for the degree of Doctor of Philosophy in Electrical and Computer Engineering presented on March 13, 2019.

Title: Low-Power Millimeter-Wave Transceiver for Short-Range Wireless and Guided Wave Links

Abstract approved: _____

Arun S. Natarajan

Low-power millimeter-wave (mm-wave) transceivers are of interest for achieving energy-efficient high data rate short-reach wireless and guided-wave links.

Spatial modulation or space-shift keying (SSK) can provide energy efficiency improvements by using antenna-switching or transmission direction switching for data modulation. Such links are particularly attractive at millimeter-wave frequencies due to small physical antenna size and large available bandwidths at mm-wave. SSK links are particularly suitable for slowly-varying channels and have potential applications on mm-wave wireless links within server chassis. A low-power pulsed two-element mm-wave transmitter (TX) is demonstrated that maintains energy-efficiency while enabling spatial modulation. A pulsed mm-wave digitally-controlled oscillator (DCO) provides low-power pulsed frequency-shift keying (FSK) capability, while variable DCO trigger pulse delay achieves controlled relative phase shift between TX elements for low-power space-shift keying (SSK). A two-element FSK/SSK 65nm CMOS TX prototype is packaged with PCB antennas to demonstrate a 2-FSK/4-SSK 3Gb/s TX with 21.4mW power consumption, achieving $\sim$7.1pJ/bit. Two different implementations of two-element mm-wave FSK-SSK receiver (RX) are presented using 65nm CMOS that concurrently demodulate FSK and SSK, with series-FSK-SSK and parallel-FSK-SSK configurations.

SSK demodulation is achieved using relative outputs of a two-element quadrature hybrid to detect angle of incidence. The 65nm CMOS 68GHz 2-element RX prototype is packaged with aperture-coupled PCB antennas to demonstrate >2Gb/s data rates while consuming <30mW across both elements. The first end-to-end CMOS FSK-SSK link using CMOS TX and RX is demonstrated with 2Gb/s data transfer across ∼6cm in a reflective channel.

Guided mm-wave links over metal wire waveguides have been proposed and promise another direction for achieving energy-efficient high data rate links. The low loss and wide dispersion-flat bandwidth of Sommerfeld-wave propagation on a single conductor wire (SCW) and TEM-wave propagation on a two-metal-wire (TMW) make such guided mm-wave electrical links promising. The first fully-integrated end-to-end low-power wireline transceiver system on a SCW using Sommerfeld-wave propagation mode is demonstrated using a 60GHz carrier frequency. Implemented in 65nm CMOS, the proposed system includes on-chip radial-mode antennas as well as integrated serializer, 60GHz OOK modulator, demodulator, deserializer and clocking. The link achieves 7Gb/s data rate across 20cm of 26AWG bare copper wire (diameter = 0.4mm), while consuming 70.9mW of power. Operating at 6Gb/s and 7Gb/s, this demonstration achieves BER $< 10^{-12}$ and 10^{-5} respectively. The two-metal-wire waveguide also has the low loss that are measured to be ∼0.2dB/cm at 60GHz and relative flat group delays. A 60GHz continuous-phase frequency shift keying (CPFSK) transceiver is implemented in 65nm CMOS as a prototype to potentially enable energy efficient high data rates guided mm-wave links over two-metal-wire and multi-lane two-metal-wire waveguides.

Low-Power Millimeter-Wave Transceiver for Short-Range Wireless and Guided Wave Links

by

Kai Zhan

A DISSERTATION

submitted to

Oregon State University

in partial fulfillment of
the requirements for the
degree of

Doctor of Philosophy

Presented March 13, 2019
Commencement June 2019

Doctor of Philosophy dissertation of Kai Zhan presented on March 13, 2019.

APPROVED:

Major Professor, representing Electrical and Computer Engineering

---

Head of the School of Electrical Engineering and Computer Science

---

Dean of the Graduate School

I understand that my dissertation will become part of the permanent collection of Oregon State University libraries. My signature below authorizes release of my dissertation to any reader upon request.

Kai Zhan, Author

ACKNOWLEDGEMENTS

I always have great curiosity for expanding my knowledge about science and technology, about how things work, about how to make things work and about how to build new things that work in a better way. I love Optics and spent four years in college studying optical information science and technology. I love Physics and spent two years in graduate school studying physics. I love integrated circuit design and electrical engineering. In June 2014, I decided to pursue a PhD degree in electrical engineering. Throughout my PhD journey of last five years, I have got tremendous help and guidance from my advisor, my committee members, professors of all the courses I have taken, colleagues that have or haven't worked on the same projects. These help and guidance have greatly assisted and helped me especially for a student who changed the major from Physics to electrical engineering. Now approaching the finish line of my PhD journey and in the process of writing a dissertation, I would like to express my sincere appreciation and gratitude to everyone that have helped, guided and supported me throughout my study as PhD candidate.

Firstly, I am greatly grateful for the opportunity offered by my advisor Dr. Arun Natarajan that allowing me pursuing the PhD degree in electrical engineering. I especially appreciated and am thankful for his continuous academic guidance and help, his great patience in the beginning of my PhD study, his great depth of knowledge in the field that I can keep learning from, his way of thinking innovative and identifying problems quickly that has gradually shape me into a better IC engineer. I am also greatly thankful to Intel, National Science Foundation and CDADIC for providing the financial support for multiple research projects and study throughout my PhD.

It is my great honor to have Dr. Karti Mayaram, Dr. Gabor Temes, Dr. Andreas Weisshaar and Dr. Tejasvi Anand on my PhD program committee and I thank them for valuable suggestions and helpful advice throughout my PhD journey.

I also appreciated the opportunity to learn CMOS Integrated Circuits from Dr. Un-Ku Moon and Dr. Pavan Hanumolu, learning network theory and analog CMOS circuit design from Dr. Gabor Temes, learning analytical techniques in electromagnetic fields

and microwave design techniques from Dr. Andreas Weisshaar, learning radio frequency IC design from my advisor Dr. Arun Natarajan, learning phase lock loop from Dr. Tejasvi Anand. I learned great amount of knowledge from these courses. Given my academic background, their courses were greatly valuable and I learned immersively from their teaches.

I am also greatly thankful to have the opportunity study and work with my colleagues in High Speed Integrated Circuit (HSIC) group: Yunqi Wang, Yao Liu, Jian Kang, Abhishek Agrawal, Sanket Jain, Manoj Johnson, Kamala Raghavan Sadagopan, Robin Garg, Anoop Sheokand, Anindita Borah, Siyuan Cheng and Hayden Bialek. Especially Jian Kang helped me greatly in my first tapeout. And Abhishek Agrawal, Jian Kang, Yao Liu, Manoj Johnson and Sanket Jain have worked on the same ICs with me. I have learned a lot from them and had a great study experience with them.

I am greatly thankful to Dr. Telesphor Kamgaing, Dr. Rahul Khanna and Dr. Georgios Dogiamis from Intel, Arizona for technical discussion throughout the Intel project. I am also greatly thankful to Guangxin Wang and Dr. Huaping Liu for having the opportunity working with them on the Intel project. I am also very grateful to Ashwin Ramachandran and Dr. Tejasvi Anand for their technical discussion, measurement support and their great knowledge of SerDes design. I am also greatly thankful to Professor Harish Krishnaswamy of Columbia University for technical discussion and having the opportunity to collaborate with his students Armagan Dascurcu, Arman Galioglu and Naresh Adepu. I am also grateful to Dr. Matthew Johnston for technical discussions and measurement support. Special thanks to Professor Hossein Hashemi and Dr. Alireza Imani of University of Southern California for providing measurements assistance with laser trimming of IC.

The six-month internship at Qualcomm was a great experience for me. I am greatly thankful to Dr. Bhushan Asuri, Dr. Chinmaya Mishra, Dr. Jagdish Pandey, Dr. Chuan Wang and Dr. Li Liu for letting me have a more comprehensive understanding of non-idealities and trade-offs in IC design and trends in the IC industry.

I would also want to thank my M.S. degree advisor Professor Janet Tate for her great help during my M.S and guidance and support in my desire to change my major and

pursue a PhD in electrical engineering.

I am greatly thankful and grateful to my parents, my mom Dongrong and my dad Xiaochun. They have always been continuously supportive to me in every aspect. Their attitudes towards life and family have continuously guided me along my journey.

I am also greatly thankful to my girlfriend Fay. Studying as PhD candidate often need continuously hard work in various research projects all year long. Maintaining a long distance relationship in such a scenario is extremely difficult. I am grateful to her for being supportive and being helpful especially when I was frustrated with my PhD.

As my PhD approaches the finish line, I know this is just the exciting beginning. I am confident that my continuous curiosity will guide me forward. I will always continuing to learn about science and technology, about how things work, about how to make things work and about how to build new things that work in a better way.

TABLE OF CONTENTS

TABLE OF CONTENTS (Continued)

LIST OF FIGURES

LIST OF FIGURES (Continued)

LIST OF FIGURES (Continued)

LIST OF FIGURES (Continued)

LIST OF FIGURES (Continued)

Figure Page

LIST OF FIGURES (Continued)

LIST OF FIGURES (Continued)

LIST OF FIGURES (Continued)

LIST OF TABLES

Chapter 1: Introduction

1.1 Overview

Data rates in both wireless and wireline communication links are rapidly increasing every year for accommodating large data throughput required by emerging applications such as Internet of things (IoT) [8], 5G [9] and Cloud AI [10]. Improving the energy-efficiency of such links is of great interest to reduce or at least maintain overall power consumption with increasing data rates, especially for communication units battery-powered. Communication links utilizing mm-wave frequencies are particularly attractive for achieving high data rates because of the large available bandwidths at mm-wave and the small physical size of multiple-antennas systems at mm-wave enabling multiple-input multiple-output (MIMO) systems [11, 12]. Wireless communication standards such as 802.11ad [13], 802.11ay [14, 15] and 5G [9, 16] all use mm-wave frequency bands for achieving multi-Gb/s data rates. This research is focused on improving energy efficiency of scalable, reconfigurable, short-range, multi-Gb/s mm-wave communication links. Given communication links consist of the transceiver and the channel, this research focuses on both improving energy efficiency with improved modulation schemes and techniques for low-power mm-wave transceiver design. The other part of this research focuses on potential low-loss and dispersion-flat channels that can further improve link energy efficiency.

Given large bandwidths, energy-efficient mm-wave links can use simple modulation schemes to achieve high data rates enabling low-power non-coherent detection and low-power transceiver design with simple architectures. On-off-keying (OOK) links at mm-wave have been proposed to achieve energy-efficient short-range applications [17–20]. OOK links are susceptible to multipath and interferers. Frequency-shift keying (FSK) links can provide improved robustness to multipath and interferers but at the cost of higher consumption compared to OOK [21]. Non-coherent demodulation of FSK at

mm-wave [22] has been proposed to reduce power consumption of FSK links. Pulse-based links at mm-wave [23,24] further improve energy efficiency for scalable data rates since the links only consume power when data is being transmitted. Spatial modulation or space shift keying (SSK) is a transmission technique [2] achieved by mapping information bits to specific antennas or by mapping information bits to specific transmission directions. SSK can be combined with other simple modulation schemes such as FSK to further improve energy efficiency by take advantage of spatial multiplexing and are particularly well-suited for communication in slowly-varying channels.

Wireless links at mm-wave or even sub-mm-wave has significant free-space path loss. Guided mm-wave links have been proposed to provide a weakly-guided mm-wave channel in free space or dielectric with lower loss compare to wireless channels. mm-Wave links have been demonstrated over polymer waveguide channels [22, 25]. Single conductor wire has been used as a low loss and dispersion free channel for THz pulse transmission [26]. Air-spaced two-metal-wire waveguide have been observed to essentially support undistorted transmission of 1.8ps electrical pulses over propagation distances up to 200 cm [27]. Conventional electrical links at high frequencies have high channel loss and high group-delay that are increasing with channel length. Therefore the equalization required to achieve high date rates is challenging to design while maintaining good overall link energy efficiency, especially for 10cm to meter scale links. Optical interconnects have low channel-loss even for long distances. But optical links suffer from poor laser energy efficiency and the need for precision physical packaging. Guided mm-wave electrical links are potential solutions for achieving energy efficiency links in the gap between conventional electrical and optical links. Guided mm-wave links over single-metal-wire and multi-metal-wire waveguides are particularly promising due to low loss and especially large flat dispersion bandwidth of these waveguides. Building fully-integrated low power transceivers that can efficiently couple mm-wave signals from the IC to TM/TEM propagation modes on metal-wire waveguides are of great interest and critical for building energy-efficient guide mm-wave links.

1.2 Organization

Chapter 2 introduces the concept of placing mm-wave wireless links within server chassis. The channel inside a server chassis is multi-path rich and relative static or slowly varying. mm-Wave channel measurements and channel analysis within server chassis are shown in this chapter. Such measurements and analysis enable energy-efficient multi-Gb/s mm-wave FSK-SSK link within server chassis.

Chapter 3 presents a two-element 68GHz FSK-SSK transmitter (TX) prototype implemented in 65nm CMOS. A pulsed mm-wave digitally-controlled oscillator (DCO) provides low-power FSK capability, while variable pulse trigger delay achieves controlled relative phase-shift between TX elements for low-power space-shift keying (SSK).

Chapter 4 describes two CMOS implementations of low-power two-element FSK-SSK receiver (RX) with series-FSK-SSK and parallel-FSK-SSK configurations. TX-RX end-to-end measurements in reflective channel are described. The first SSK-FSK link in CMOS and the feasibility of using SSK improving energy efficiency are demonstrated.

Chapter 5 presents the first demonstration of a mm-wave data link using Sommerfeld-wave propagation on a single conductor wire using a fully-integrated end-to-end prototype implemented in 65nm CMOS. The feasibility of energy-efficient high data rate links over low-loss and low-dispersion metal wire waveguide is demonstrated.

Chapter 6 describes the design and measurements of a 60GHz continuous phase frequency shift keying (CPFSK) transceiver proposed for guided mm-wave links over multi-lane two-metal-wire waveguide.

Chapter 7 concludes the research of low-power mm-wave transceiver design for short-range wireless and guided mm-wave links and ends with a brief discussion of potential future work.

Chapter 2: Millimeter-Wave Channel Analysis in Enclosed Server Chassis

Placing wireless links within server chassis is of interest to provide a re-configurable communication path between different server boards for short-range data links as well as establish a control infrastructure for low data-rate management and monitoring (Fig. 2.1). The mm-wave channel within server chassis is multipath-rich due to the reflections from both the metal enclosure and the dense micro-server boards installed inside. Such a channel is also relatively static or slowly-varying because both server boards and the proposed mm-wave transceiver are physically fixed within the server chassis.

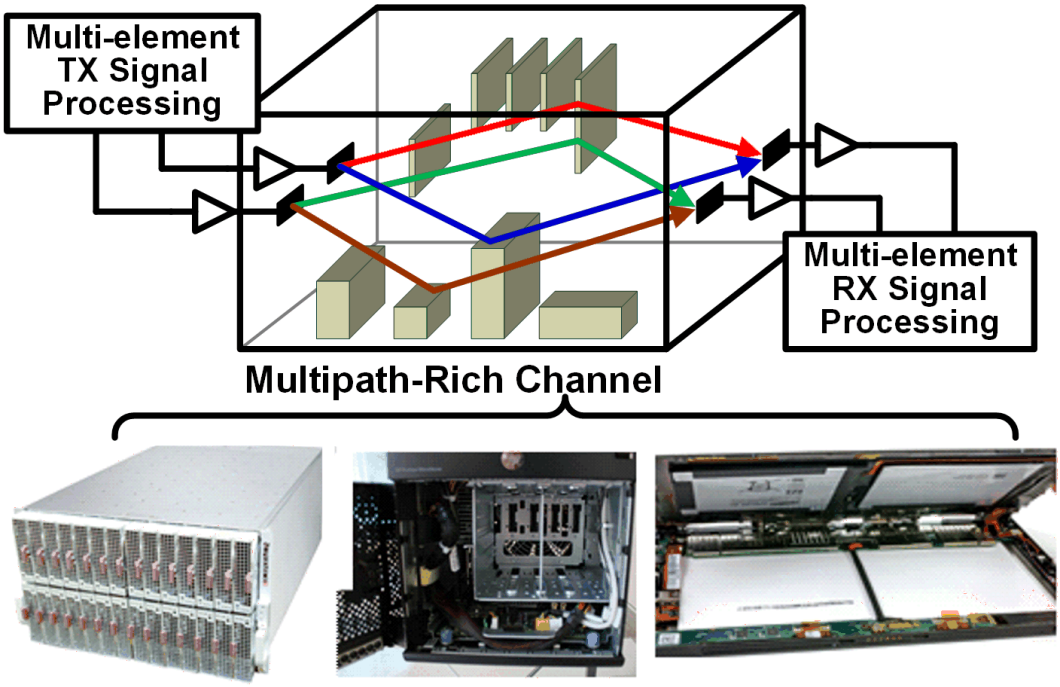

Figure 2.1: System overview of low-power mm-wave wireless interconnect within enclosed platforms using spatial modulation/space-shift keying (SSK).

In order to take advantage of the slowly-varying feature as well as to be compatible with the multipath-rich environment, understanding the channel within enclosed server

chassis is essential for building wireless links. mm-Wave channel measurements are performed at around 56GHz using the connectorized bowtie and patch antennas developed and fabricated on Rogers laminates using lithography at an in-house cleanroom (Fig. 2.2). Fig. 2.3 shows the server chassis provided by Intel and a custom-fabricated metal cover with slots enabling mm-wave channel measurements within server chassis.

Figure 2.2: Broadband 56-62GHz bowtie and 55-57GHz patch antennas fabricated on Rogers substrate and connectorized with V-band end launches; Simulated radiation pattern of the bowtie antenna.

With the custom test setup developed for in-situ channel measurements, the path loss of both line-of-sight (LOS) and non-line-of-sight (NLOS) links across different TX-RX separations and different antenna inserted depths. Fig. 2.4 shows the measured channel frequency response with 80mm TX-RX separation and different insertion depths for three different scenarios: No server boards installed in Scenario 1 (LOS), server boards installed between TX and RX in Scenario 2 (special-LOS) and Scenario 3 (NLOS). With server boards fully populated, 1cm head room is existing between the top of microserver boards and the metal cover. Scenario 2 is the case where TX and RX antennas are inserted 5mm into the chassis utilizing such headroom to create a special-LOS channel. The measured path loss in dB is fitted as a function of distance d (unit: mm) and given by [1]

$$\begin{aligned} PL_{LOS,Scenario1}(d) &= 29.6 + 1.66 \times 10log_{10}d \\ PL_{NLOS,Scenario3}(d) &= 57.6 + 0.096 \times 10log_{10}d \\ PL_{special-LOS,Scenario2}(d) &= 28.1 + 1.49 \times 10log_{10}d \end{aligned} \tag{2.1}$$

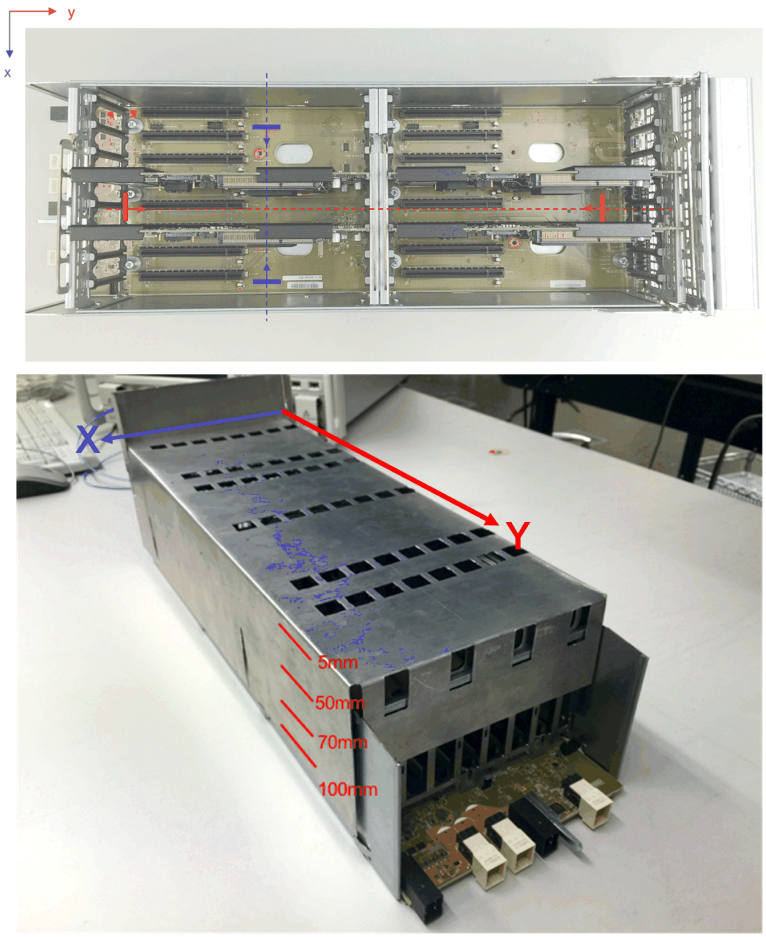

Figure 2.3: Microserver chassis provided by Intel and custom-fabricated metal cover with slots for inserting connectorized antennas to evaluate millimeter-wave channel inside enclosed server chassis. Courtesy of [1].

Fig. 2.5 shows the measured RMS delay spread for special-LOS and NLOS cases. NLOS links show RMS delay spread of 32ns @ 50% CDF (200ns @ 90% CDF) with path loss $>$ 55dB, indicating a challenging environment for low-power high-speed links. A modified chassis with 10mm headroom between the top of the boards and chassis cover can enable a special-LOS channel with 35dB loss and RMS delay spread of 14ns @ 50% CDF (20ns @ 90% CDF) [1].

We propose the modulation using the spatial dimension in such slowly-varying chan-

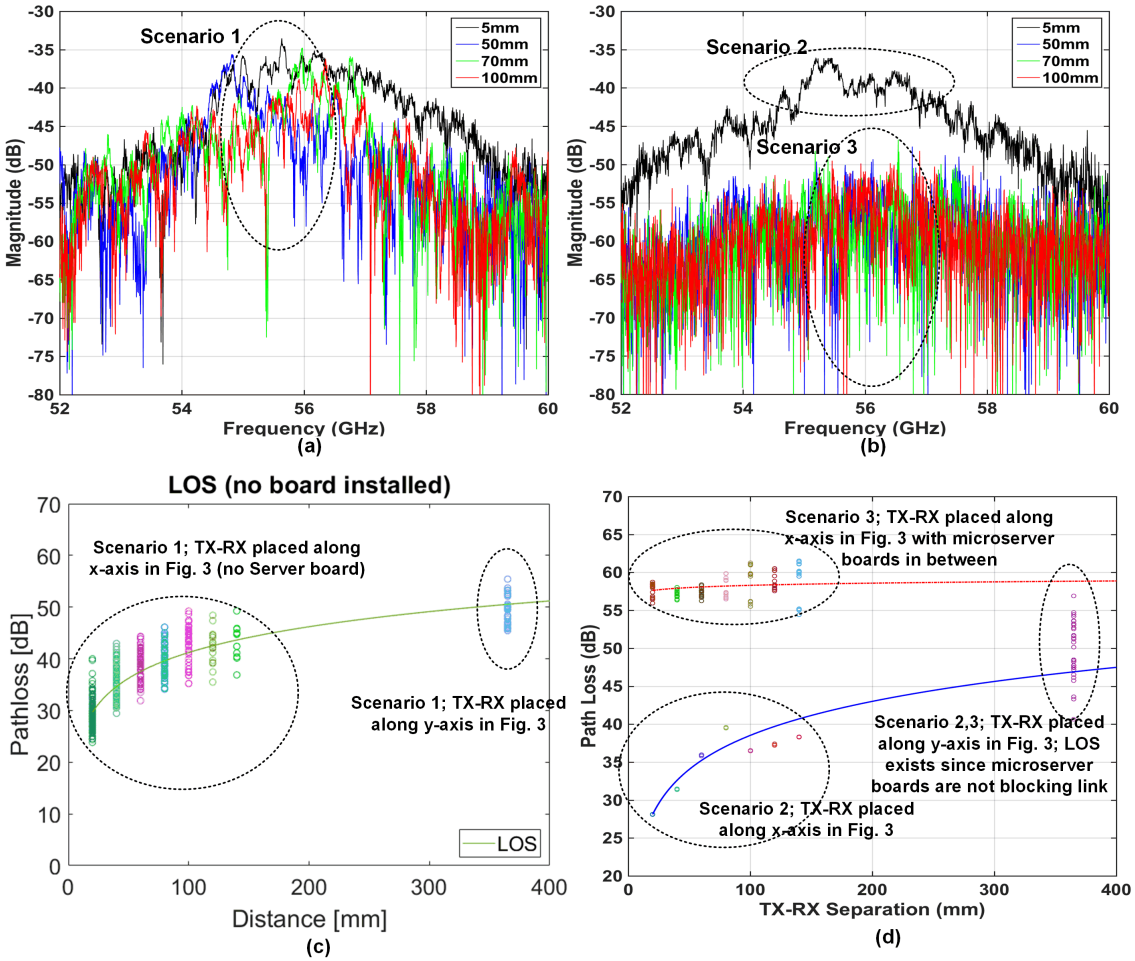

Figure 2.4: Measured channel frequency response with the 55-57GHz patch antenna with 80mm TX-RX separation and different insertion depth for (a) Scenario 1; (b) Scenario 2 & 3; (c) Measured path loss in scenario 1; (d) Measured path loss in Scenario 2 & 3. Courtesy of [1].

nels to improve the energy efficiency. As shown in Fig. 2.6, multiple antennas in the TX launch signals into different transmission directions based on baseband data. The transmission direction is a spatial parameter and the transmission-direction switching technique is equivalent to space-shift keying (SSK). The corresponding RX needs to detect incident signal direction by looking at the relative strength and phase of signals at different antennas to demodulate SSK signals. Fig. 2.7 shows a SSK receiver scheme

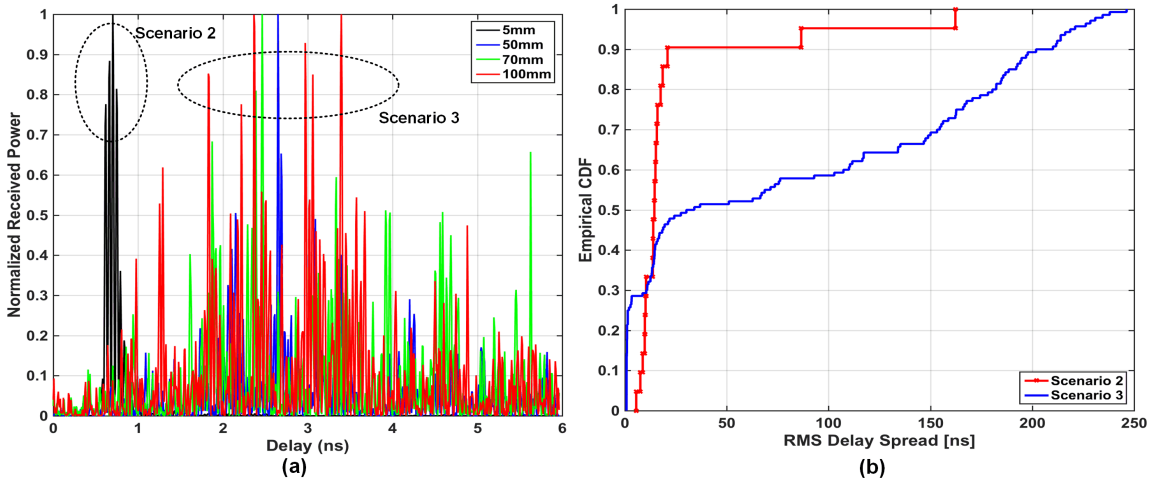

Figure 2.5: Measured RMS Delay Spread (RDS) in Scenarios 2 and 3. Courtesy of [1].

utilizing Butler matrix as SSK demodulator. The received signals coming from different TX antennas has different phase information at *RX1* and *RX2*. Such phase information is directly related to the spatial parameters of the TX and RX antennas. Using the Butler matrix which provide 0° relative phase shift from *RX1*-to-*Out1* and *RX2*-to-*Out2*, and $(\pi - \phi)$ phase shift from *RX1*-to-*Out2* and *RX2*-to-*Out1*, *Out1* only detects signal come from TX2 and *Out2* only shows signal come from TX1.

Consider a MIMO system with 2-element TX and 2-element RX within enclosed server chassis (Fig. 2.8) and the 2-element TX capable of radiating into four different directions θ_1, θ_2, $-\theta_2$ and θ_2 based on baseband data. Also, assume the TXs are pulsed with 25% duty-cycle and 250ps ON time to wait for the echoes became weaker before the transmission of the next symbol. The received time-domain waveforms at *RX1* can be expressed as

$$U_{RX1}(t) = \frac{A}{Path_{LOS}} U_{TX}(t - \frac{Path_{LOS}}{c}) + \sum_{k=1}^{4} \frac{A \times \Gamma^k}{Path_{top,ref,k}} U_{TX}(t - \frac{Path_{top,ref,k}}{c}) + \sum_{k=1}^{4} \frac{A \times \Gamma^k}{Path_{bot,ref,k}} U_{TX}(t - \frac{Path_{bot,ref,k}}{c}) \tag{2.2}$$

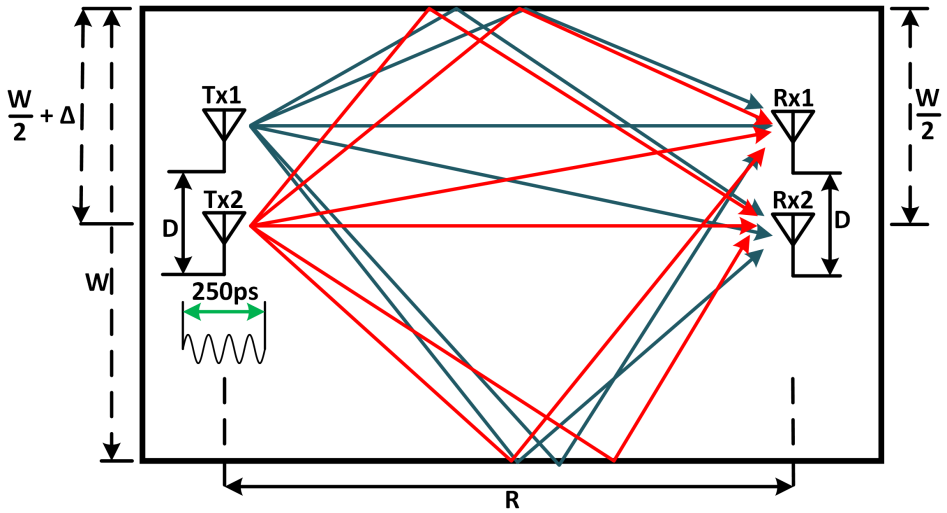

Figure 2.6: Space-shift keying transceiver approach for low-power mm-wave links in a slowly-varying channel.

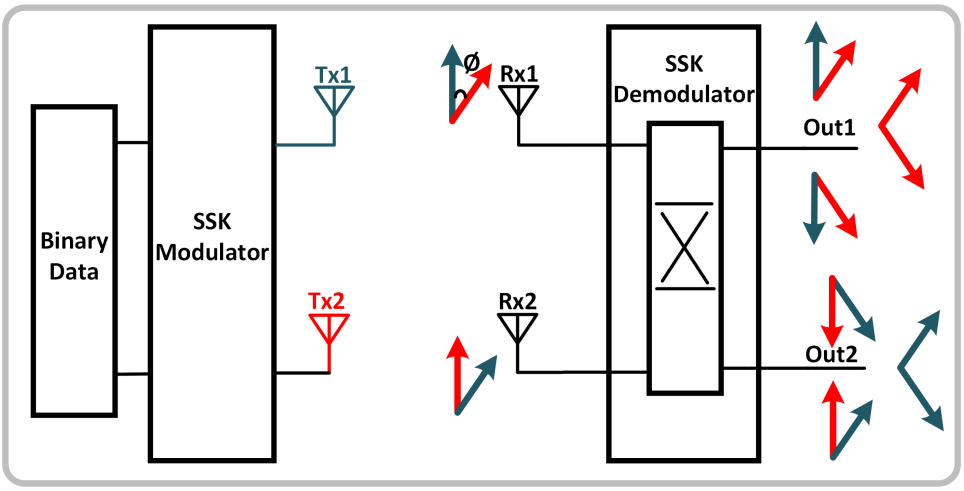

Figure 2.7: SSK receiver scheme utilizing Butler matrix based spatial filter for spatial modulation detection [2, 3].

where c is the speed of light in air, Γ is the reflection loss, A is constant and $Path_{LOS}$ is the distance of LOS path. $Path_{top,ref,k}$ and $Path_{top,bot,k}$ are the distances of NLOS path with k times reflections starting from top metal reflector and bottom metal reflector respectively. The reflection loss is assumed to be independent of incident angles and polarization. The TX and RX antennas are also assumed to be radiating equally in all

directions. Only echoes corresponding to four times reflections are considered here. The time-domain waveforms at *RX2* can also be expressed by Eq. 2.2 with all the $Path_{LOS}$, $Path_{top,ref,k}$ and $Path_{bot,ref,k}$ slightly different (Fig. 2.8). Once the TX/RX antennas and the server chassis enclosure are physically fixed, the magnitudes and the delays of the signals and the echoes are merely determined by the spatial parameters of the channel, such as TX/RX antenna separation, the choices of SSK directions, TX-RX separation, the dimension of the server chassis and locations of the TX/RX antennas within server chassis.

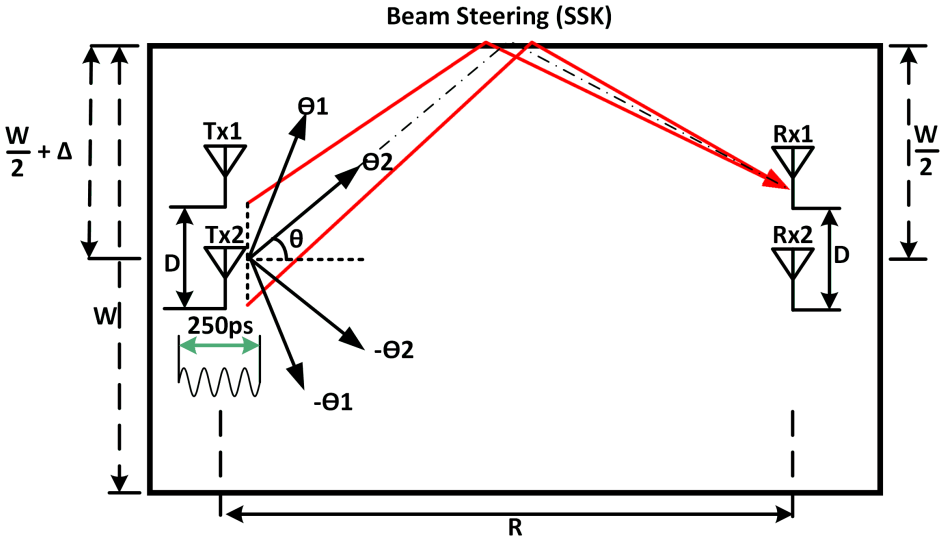

Figure 2.8: Channel analysis for 2-element TX and 2-element RX MIMO system in enclosed server chassis.

Fig. 2.9 shows the simulated time domain waveforms at *RX1* and *RX2* based on 2.2 for *D*=5mm, *R*=50cm, *W*=15cm,Δ=0cm,Γ=0.5 and SSK directions $\Delta\phi$=$\pm 0.6\pi$,$\pm 1.2\pi$. The 1ns symbol duration can be divided into four 250ps-windows, leading to 8 such windows across *RX1* and *RX2*. The relative signal strength in each 250ps-window is only determined by the spatial parameters or the signatures/fingerprints of the channel. It is possible to detect four SSK directions with a minimum Hamming distance of 2 only using two RXs. Making the locations of TX/RX antennas less symmetrical can potentially improve the SSK modulation depth supported by the channel.

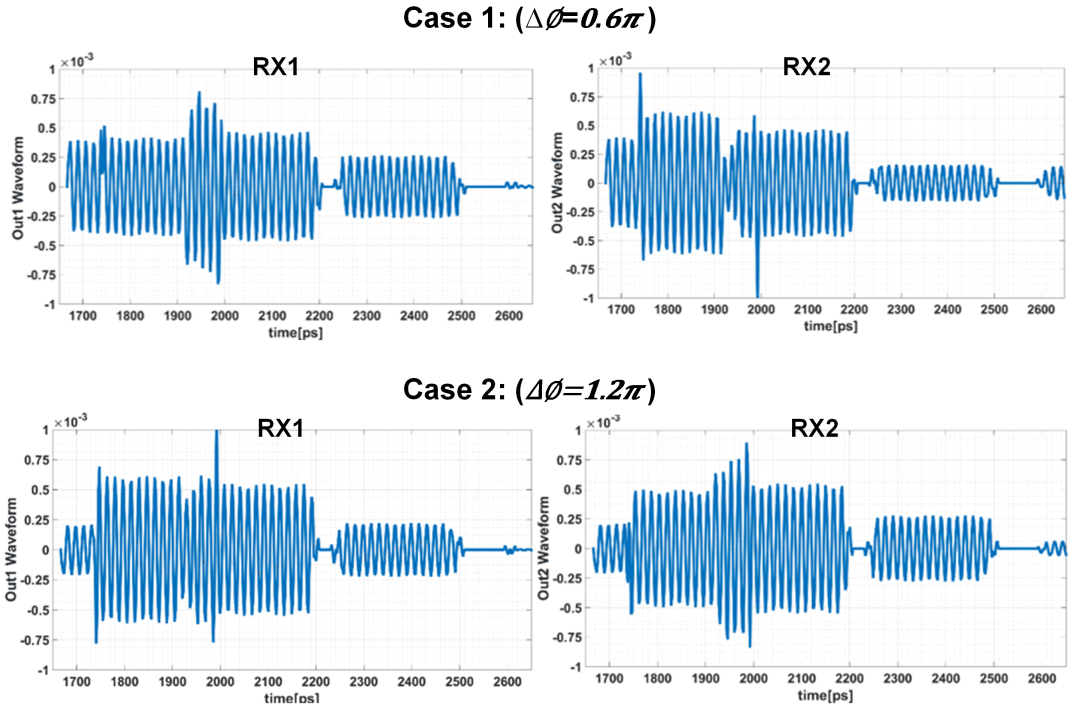

Figure 2.9: Simulated time domain waveforms of *RX1* and *RX2* in Fig. 2.8 with 4-SSK in enclosed platforms.

Chapter 3: A Low-Power FSK/Spatial Modulation Transmitter for mm-Wave Wireless Links

3.1 Introduction to Energy-Efficient Spatial Modulation TX

The small physical size of integrated mm-wave wireless links make them attractive for energy-efficient Gb/s wireless links with $\sim$10 cm to 50 cm range. Links with low-complexity OOK [18]/FSK modulation [21] as well as coherent QPSK modulation [28] have been proposed. The wide available bandwidth at mm-wave and the absence of PLLs makes OOK/FSK attractive for energy efficiency. In addition, pulse-based transmitters (TX) with duty-cycling can be used to lower TX power consumption (Fig. 3.1(a)). This can also be considered in terms of transmitter efficiency η and the targeted radiated power (Fig. 3.1(b)). Spatial modulation offers further improvements in energy efficiency over a single-element TX in slow-varying channels by using multiple antennas to encode information in addition to OOK/FSK/PSK constellations [2].

Spatial modulation or space shift keying (SSK) can be achieved by mapping bits to specific antennas (Fig. 3.1(c)) or by mapping bits to specific transmission directions using TX arrays, particularly if the RX has multiple antennas that provide TX-RX direction discrimination (Fig. 3.1(d,e)). In the first case, adding SSK modulation increases the number of bits in each TX symbol without increasing power consumption, leading to lowered TX energy/bit (E/b). However, the phased-array approach in (Fig. 3.1(d,e)) is desirable since effective isotropic radiated power (EIRP) for given DC power is improved by the array, leading to further decrease in energy/bit (E/b). In addition, the array approach allows higher-order SSK even with two antennas. Fig. 3.1 shows the improved E/b by adding SSK to FSK TX. It can also be shown that RX E/b, even in the two-element RX case, is marginally better with 4-SSK leading to overall improved E/b. Notably, such SSK links are well suited for board-to-board communication in reflective computing chassis where channels are slow-varying and contain transmit-direction

dependent multi-path components [1].

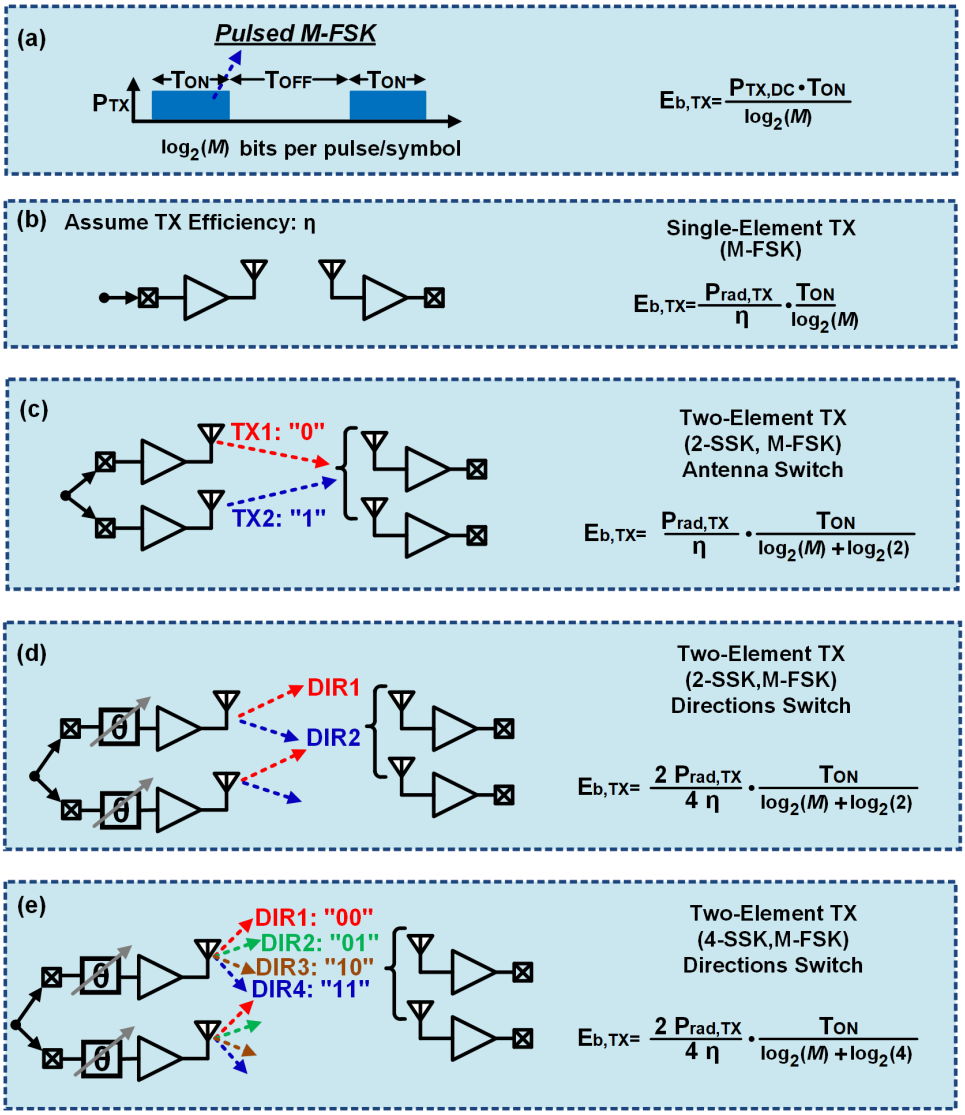

Figure 3.1: Low-power mm-wave TX with spatial modulation/space-shift keying (SSK) added to pulsed-FSK for higher energy efficiency.

Pulsed-FSK signals can be generated efficiently by duty-cycling a PA following a always-ON digitally-controller oscillator (DCO) or by directly duty-cycling a DCO (Fig. 3.2). Achieving pulsed operation with the PA at Gb/s data rates is challenging. We

proposed to use a pulsed DCO directly driving the antenna to generating the pulsed-FSK signals. This can not only avoid the challenging design of duty-cycling PA as well as decrease the power consumption of the DCO and eliminate the energy inefficient PA from TX. In addition, SSK as described in Fig. 3.1(d,e) requires variable phase shift in each TX element (Fig. 3.3(a)). Active phase shifters consume significant power relative to the duty-cycled DCO, particularly since duty-cycling active phase shifters with $<$300 ps settling times is unfeasible. Passive phase shifters do not consume power but result in $>$5 dB insertion loss at mm-wave leading to poorer E/b for a given TX EIRP. As shown in Fig. 3.3(b), the relative delay between trigger signals to pulsed-DCOs can be used to control the starting phase difference between DCOs and thus achieve low-power phased-array operation [28]. A key challenge of such approach is the phase between the oscillators lose coherence due to noise across time. However as long as the DCO is ON for relatively short impulses and is restricted to a few oscillator cycles, the phase different between the two-element TX can be controlled deterministically by varying the relative delay of the trigger. In the following section, this approach is used to demonstrate low-power SSK in a 2-element mm-Wave CMOS TX.

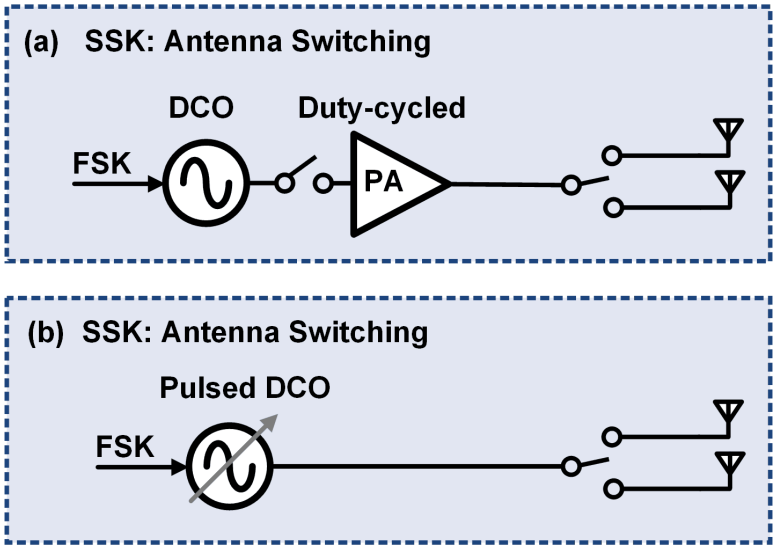

Figure 3.2: Architecture of Pulsed FSK Generation: (a) Duty-cycled PA at Gb/s, (b) Pulsed power DCO.

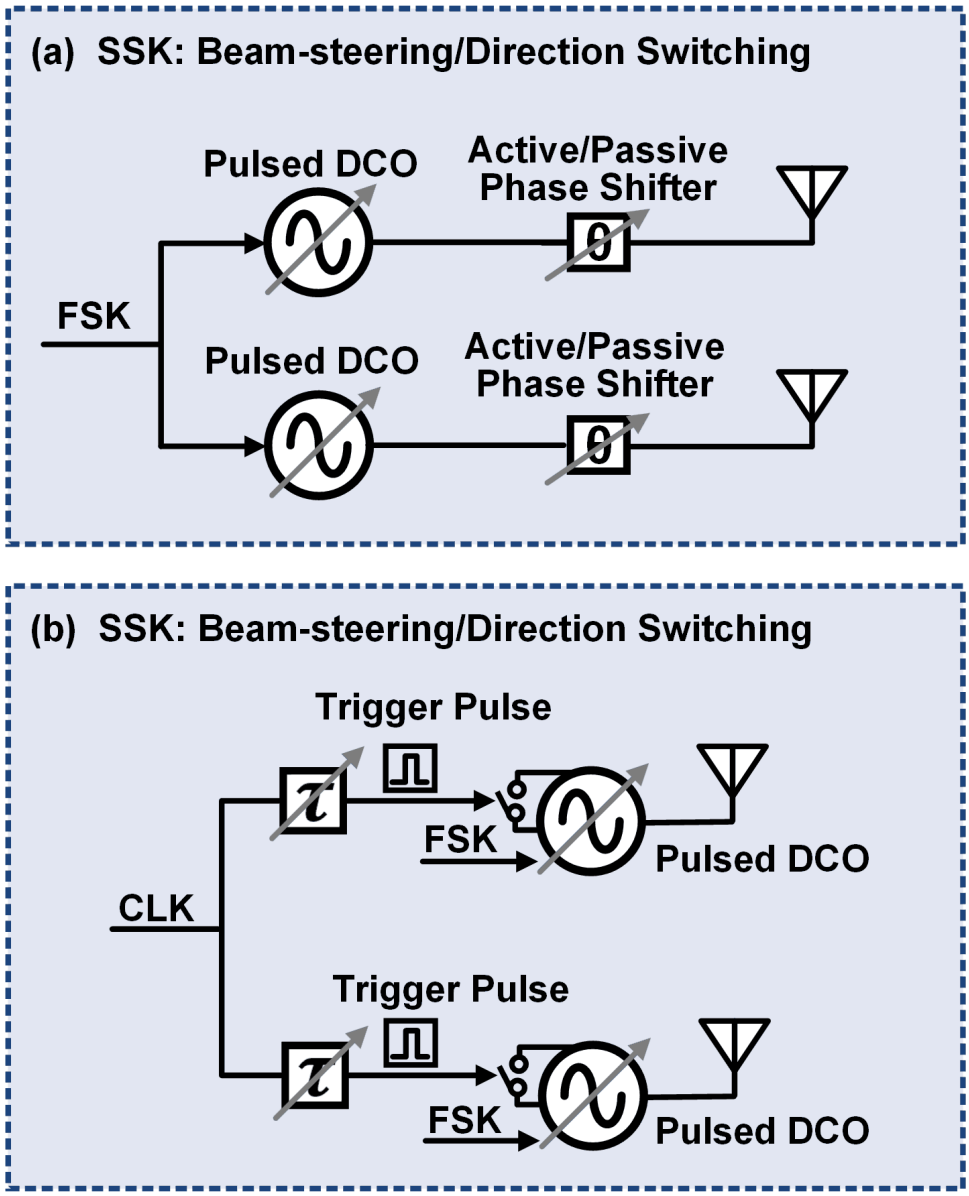

Figure 3.3: Phase shift for low-power SSK TX (a) Active/passive RF-path phase shifting, (b) Phase shift by changing trigger delays in pulsed DCO.

3.2 Low-Power FSK-SSK Transmitter Design

The proposed 2-element FSK-SSK TX is shown in Fig. 3.4.

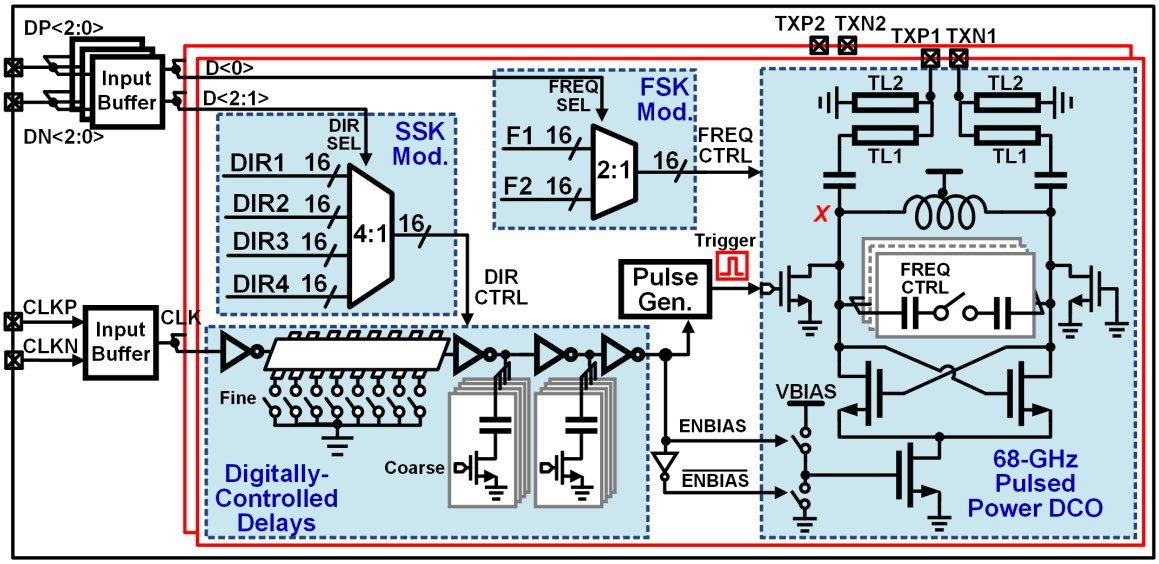

Figure 3.4: Architecture and schematic of two-element mm-wave pulsed-DCO based FSK-SSK TX in 65-nm CMOS.

3.2.1 68GHz Pulsed Power DCO Design

Pulsed mm-wave FSK modulated signal is generated using a mm-wave DCO in each element. The schematic of the DCO is shown in Fig. 3.4. The DCO is implemented as a cross-coupled oscillator with a custom resonator. Fig. 3.5 shows the custom inductor and cap bank model. The DCO inductor is implemented using the top metal with 3.4μm thickness and is optimized to improve the quality factor as much as possible in around 68GHz. The DCO frequency is controlled by switches in series with metal strips placed under the DCO inductor, similar to [29, 30]. A small section of CPWG is also included in the EM simulation. Fig. 3.6 shows the simulated frequency tuning curve and output power at the differential 100Ω antenna. Measurements showed 10% higher frequency than simulation, with measured 4.7-GHz frequency tuning range from 66 GHz to 70.7 GHz with 290-MHz frequency resolution. Pulsed FSK operation is achieved by duty-cycling the DCO bias while changing resonator frequency. A mm-wave PA following the DCO cannot be duty-cycled at Gb/s data rates and an always-enabled amplifier dominates power consumption degrading energy efficiency. Therefore, as shown in Fig. 3.4, on-chip transmission lines (TL_1 and TL_2) match the 400-Ω DCO impedance

directly to 100-Ω at the output of each element. The DCO provides 0 dBm output power to the 100-Ω load and consumes ∼9 mW from 1 V supply with 50% duty-cycling at 1 Gb/s FSK (∼ 500 ps on-time for DCO).

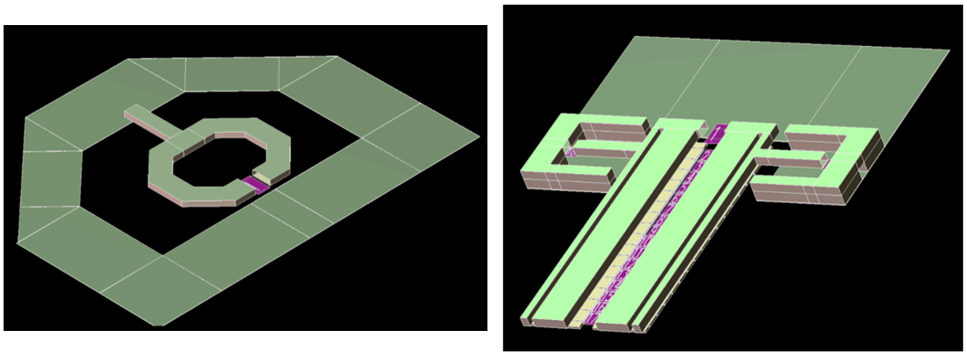

Figure 3.5: Customized inductor and cap bank IE3D models used in the proposed pulsed DCO.

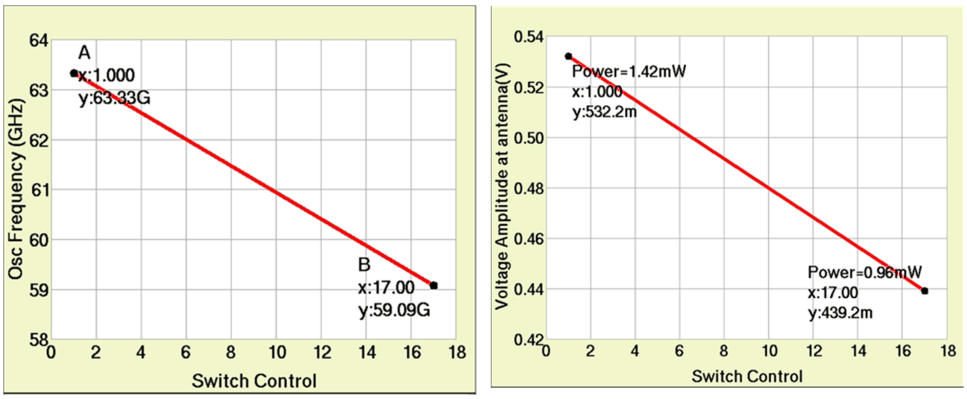

Figure 3.6: Simulated tunning curve and output power of the proposed DCO.

3.2.2 Low-Power Spatial Modulation

Switching between antennas, as described in Fig. 3.1(c), is supported by simply enabling suitable DCO in the 2-element TX (Fig. 3.4). However, spatial modulation based on different TX angles of radiation (Fig. 3.1(d,e)) requires variable phase shift. This is achieved by controlling the relative delay between the DCO-enable/trigger signals ap-

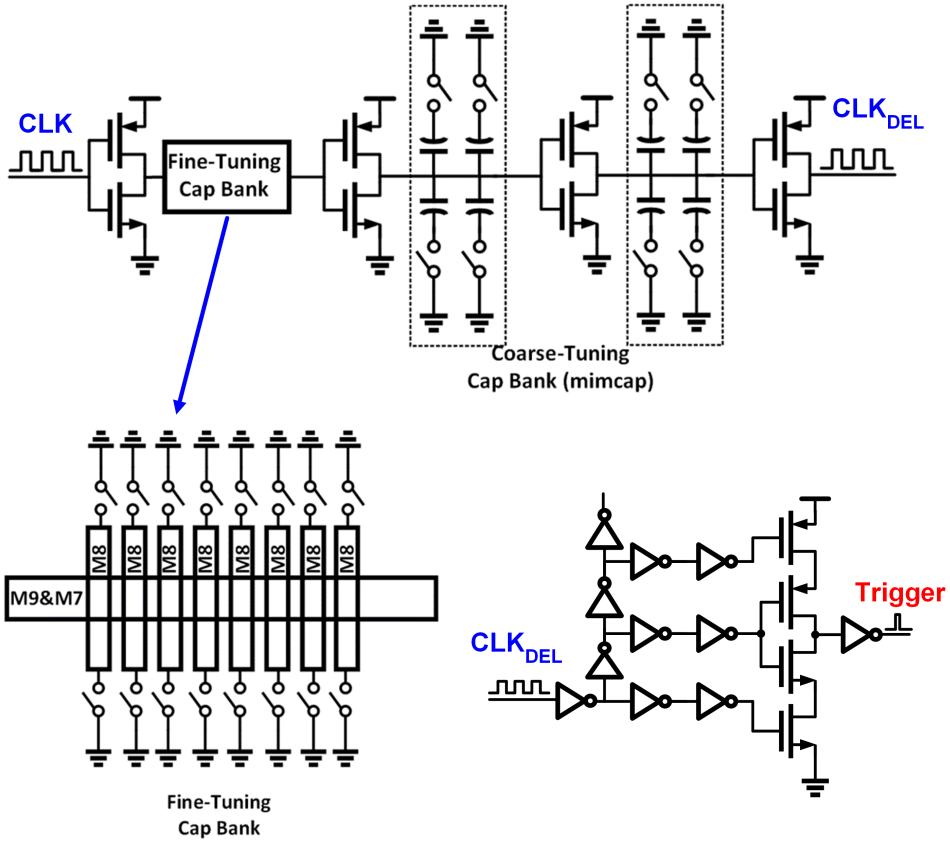

Figure 3.7: Schematic of the coarse and fine delay cells and edge combiner pulse generator.

plied to the DCO in the two elements. As shown in Fig. 3.4, the DCO-enable signal is applied to enable the bias voltage of the DCO current source following a variable coarse and fine delay cell. A trigger pulse generated from the same DCO-enable signal using edge combiner [31] is applied at node X after 80ps delay compare to the DCO-enable signal. The trigger pulse shorts one side of the resonator to ground and creates significant asymmetric current in the LC tank, enabling the kick-startup of the oscillator. The delay of the clock edge is accomplished using a bank of coarse and fine delay cells. The resolution of the delay cells need to be small fraction of the 15ps time period of the DCO output signal. Fine resolution is critical for accurately controlling the phase shift of the oscillator and the range of the delays need to cover the period of the DCO

output signal. Fig. 3.7 shows the schematic of the coarse and fine delay cells as well as the edge combiner pulse generator. The coarse delay is accomplished using capacitive loading of inverter buffers. Finer delays are achieved using a loaded transmission line with switchable metal strips. Fig. 3.8 and Fig. 3.9 shows the simulated performance of the delay cells with equivalent $\sim 10^{\circ}$ phase shift resolution and more than 360° phase shift range.

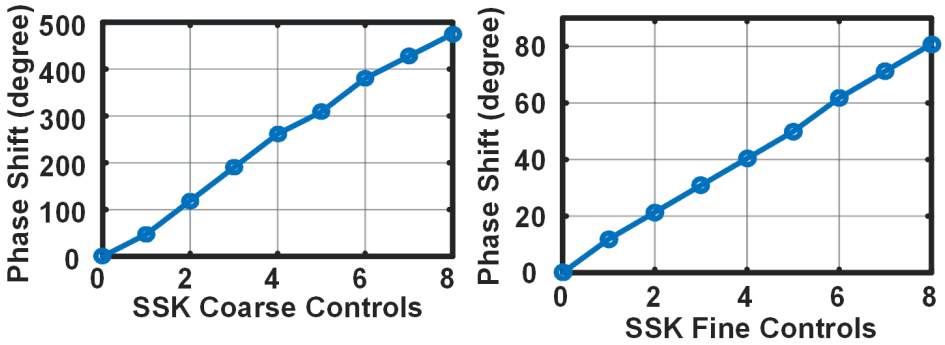

Figure 3.8: Simulated phase shift with coarse and fine control provide 360^{o} phase shift with $\sim 10^{o}$ resolution.

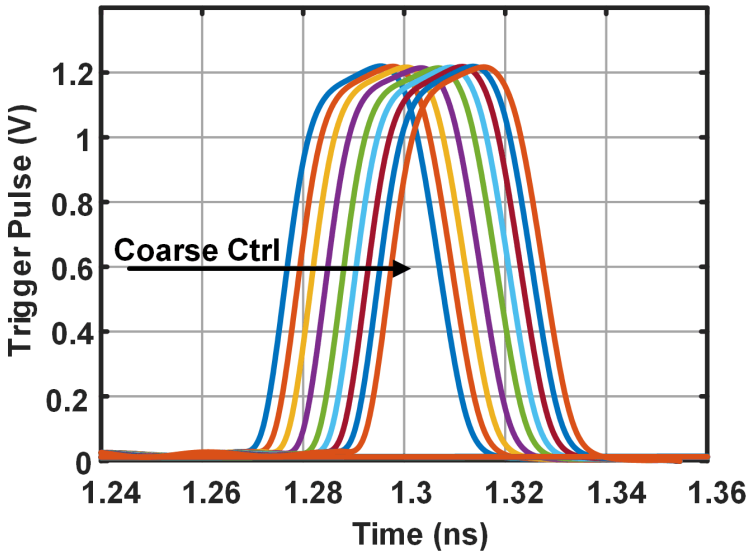

Figure 3.9: Simulated DCO trigger pulse at different coarse delay controls.

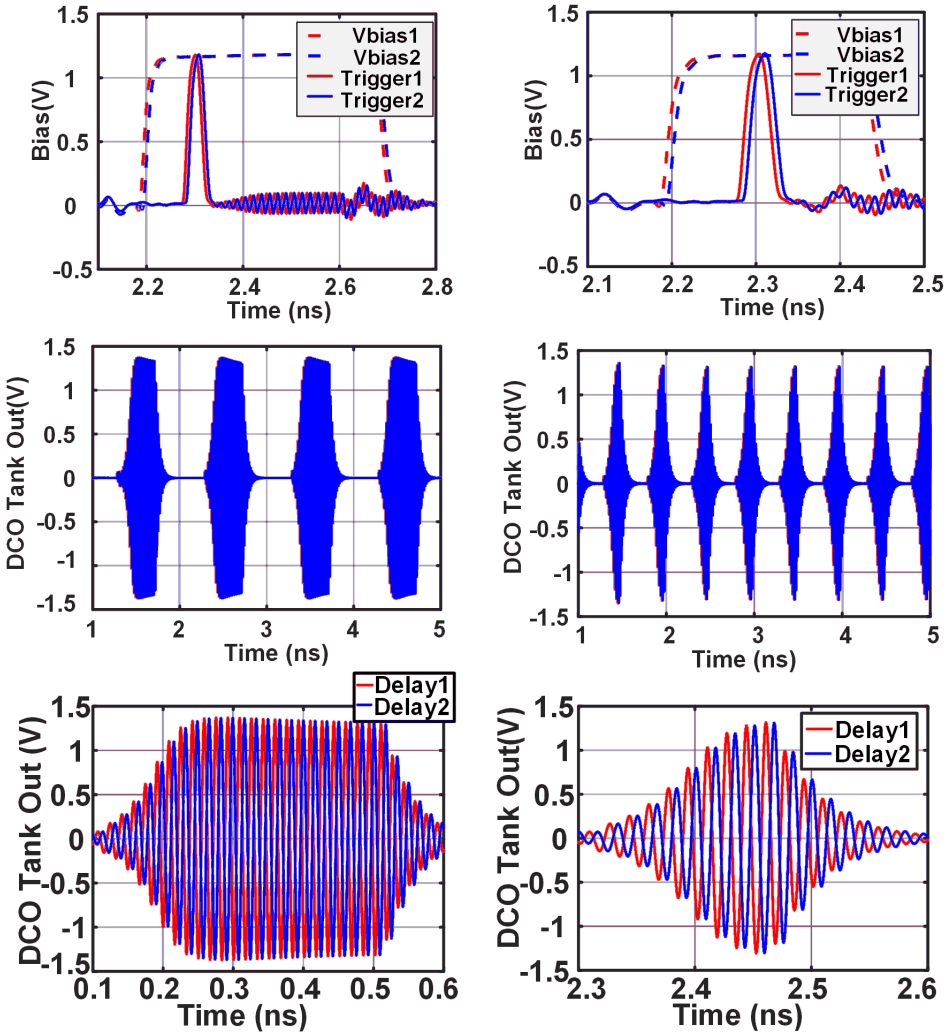

Figure 3.10: Simulated DCO startup with 8 ps relative trigger delay for 500ps ON and 250ps ON time.

Fig. 3.10 shows the simulated performance of the DCO startup with a relative time delay of 8 ps for both 500ps and 250ps on times demonstrating phase coherence between oscillator output in the two cases. The absence of a PLL implies that phase noise makes the final phase difference between the two free running DCOs random and time varying. However, for a DCO Q of 15, the DCOs are coherent for the first few cycles following bias enable, making the proposed approach suitable for a pulsed scheme with $\sim$500 ps

on time (∼30 cycles). This can be verified by EIRP measurements that depend upon relative phase shift and coherence between elements.

Incoming data is divided into FSK (1-bit) and SSK (2-bits) modulation paths (Fig. 3.4). The FSK bit drives a multiplexer selecting DCO oscillation frequencies. The SSK bits control the coarse and fine trigger signal delay (Fig. 3.8) to each DCO with 0.4 ps resolution (Fig. 3.8. Modulation rates are limited by DCO startup and shutdown with bias control (Fig. 3.8) - faster data rates require higher DCO frequency/power consumption.

3.2.3 IC Packaging with Off-Chip Antennas and L-C-L Bondwire matching

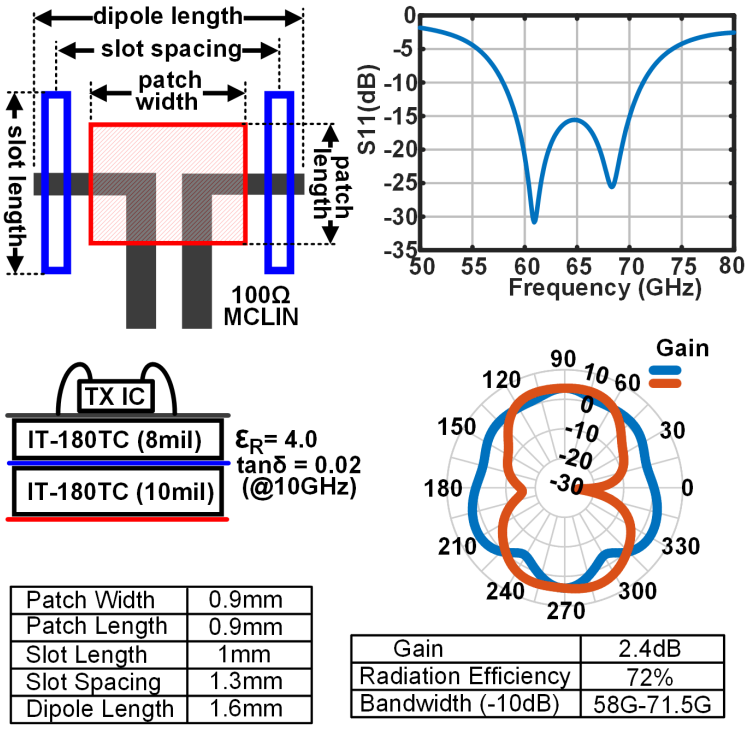

Patch Width	0.9mm
Patch Length	0.9mm
Slot Length	1mm
Slot Spacing	1.3mm
Dipole Length	1.6mm

Gain	2.4dB
Radiation Efficiency	72%
Bandwidth (-10dB)	58G-71.5G

Figure 3.11: IC packaging in commercial PCB technology with balanced aperture-coupled patch antenna.

This work uses low-cost chip-on-board packaging to connect the mm-wave TX elements to antennas-on-PCB using wire bonds. A commercial FR4-based PCB (ITEQ 180C) with $\epsilon_r = 4.0$ and dielectric loss tangent of 0.02 at 10 GHz is used with the stack-up shown in Fig. 3.11. A balanced-fed aperture-coupled patch antenna provides wide-band performance for differential TX output. The wide-band antenna shows 2.4 dB gain with 72% efficiency at 68 GHz in simulation. Bondwire inductance parasitics at mm-wave are addressed by a narrowband bondwire matching network, similar to [32]. A second series wire bond on the PCB creates an L-C-L matching network from the IC to the antenna (Fig. 3.12), with stand-alone simulations/measurement indicating $\sim$1 dB insertion loss for the network and 3.6 dB/cm loss for 100-Ω differential traces on the PCB.

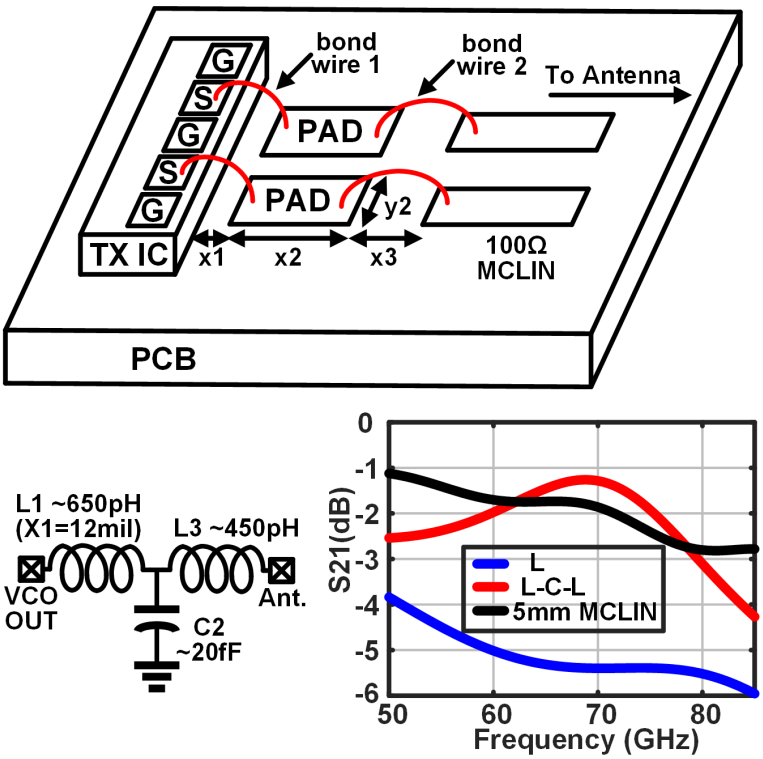

Figure 3.12: Bondwire L-C-L matching structures for impedance-matching 100-Ω differential IC output to antenna.

IC-antenna co-integration is possible at mm-wave frequencies [33–36] and such ap-

proach can provide efficient and scalable mm-wave antenna interfaces to avoid the L-C-L matching structure in the future works.

3.3 Measurement of FSK/SSK TX

Fig. 3.13 shows the die photo of the 1.1 mm^2 two-element TX IC fabricated in 65nm CMOS and the photo of IC packaged with the two aperture-coupled antennas spaced 4.4 mm apart.

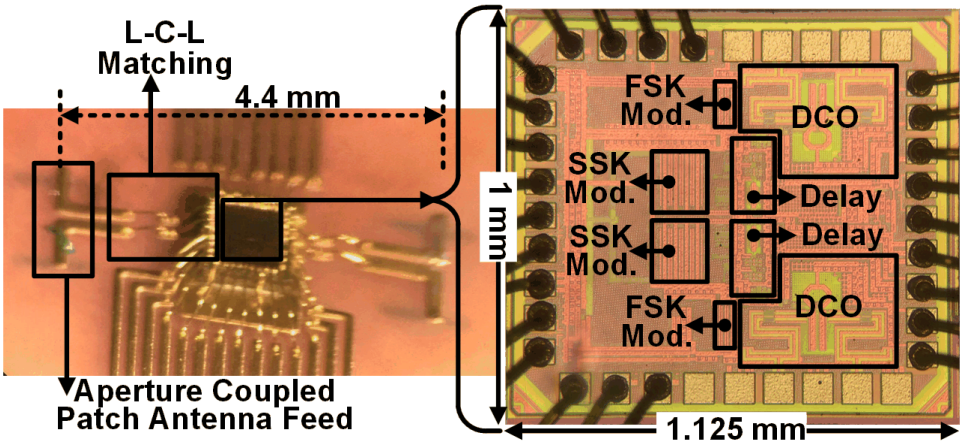

Figure 3.13: Two-element mm-wave TX packaged with PCB antennas using chip-on-board approach with PCB wirebonds for impedance matching.

The 65-nm CMOS FSK/SSK TX was characterized using both probe and package measurements. Fig. 3.14 shows the measurements setup for both the probe level and wireless characterizations. PRBS Data and clock from the Arbitrary Waveform generator is provide to the IC and the mm-wave TX output is measured using a probe and a horn antenna followed by V-band mixer. A small anechoic corner is created in the lab to measure the TX output for wireless measurements.

Measured DCO frequency tuning range and EIRP with probe level and with antennas are shown in Fig. 3.15, demonstrating 4.7-GHz tuning and $>$ 0-dBm EIRP. Importantly the frequency is only slightly changed by the change in termination from probe to antenna on the DCO output.

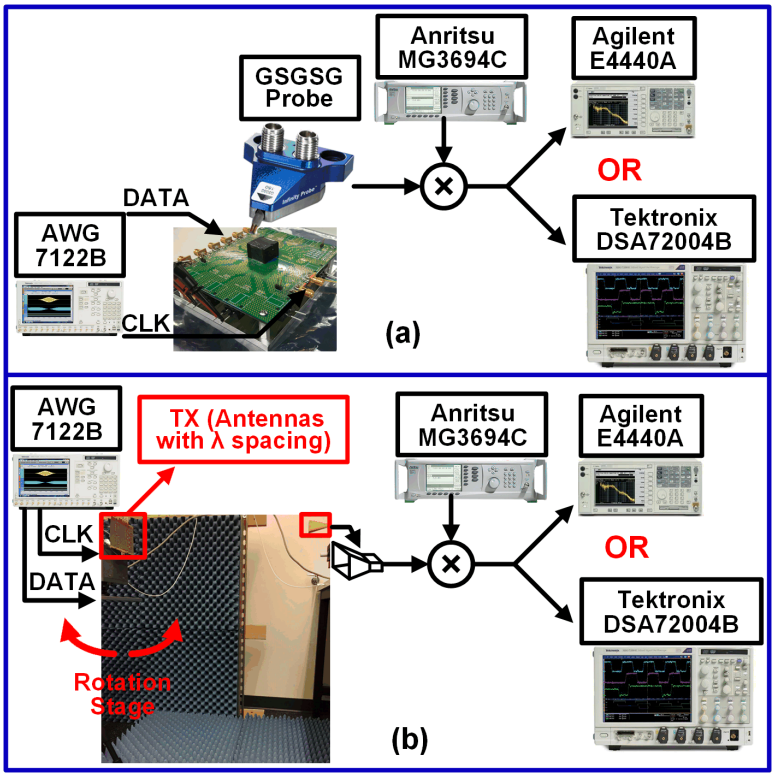

Figure 3.14: Measurement setup for the two-element FSK-SSK 68GHz prototype.

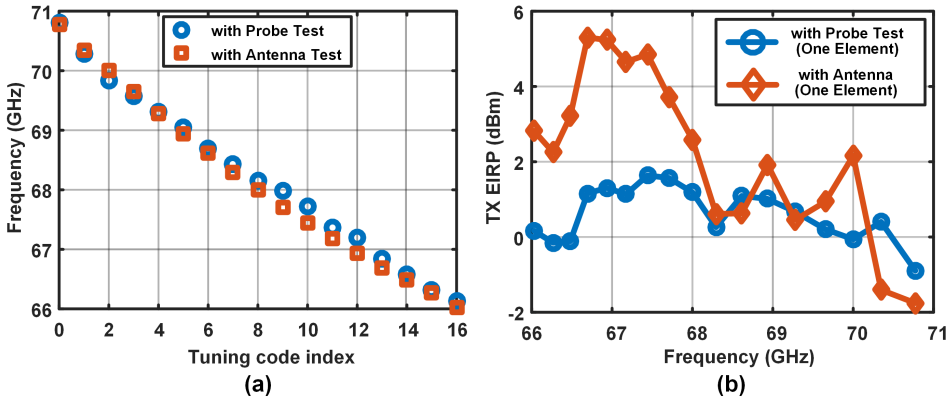

Figure 3.15: Measured DCO frequency tuning curve and TX EIRP across tuning range with probe and antenna testing.

A mm-wave RX built with COTS components is used for wireless testing of the TX IC packaged with antennas. Pulsed FSK-DCO operation is measured using the RX

down-converter demonstrating 1 Gb/s FSK modulation (Fig. 3.16).

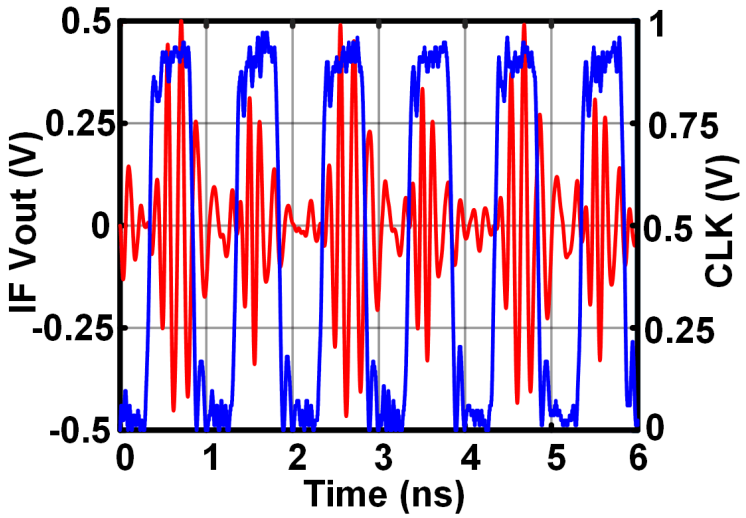

Figure 3.16: Measured time-domain 1Gb/s pulsed-FSK waveform after down-conversion.

The efficacy of the variable phase shift generation between the two DCOs through trigger pulse delay is shown in Fig. 3.17 and Fig. 3.18. Single-element and two-element pattern with no delay shows beam narrowing with two elements (Fig. 3.17). The two-element pattern shows the impact of the coherent addition and subtraction of signals in an array demonstrating the functionality of phase shift using the trigger delays. This beam can be steered as shown in Fig. 3.18 by changing the relative trigger delay.

The phased array operation is also confirmed by measuring the power for a fixed RX orientation across delay settings. As shown here, the peak-to-null ratio of $>$ 20dB demonstrates that the phase shift resolution is sufficient to achieve good cancellation of signals (Fig. 3.19). Hence, for a fixed TX-RX channel, TX direction change can be used to encode information.

As shown in Fig. 3.20, the plot shows the measured down-converted waveform using a single fixed antenna as the RX for four different beamsteering angles (one-side). Such a 3 Gb/s link is achieved over 60-cm TX-RX separation using 4-SSK and 2-FSK modulation. The TX is compared to state-of-the-art in Fig. 3.21, demonstrating low-power spatial modulation leading to good energy-efficiency as well as range up to 60

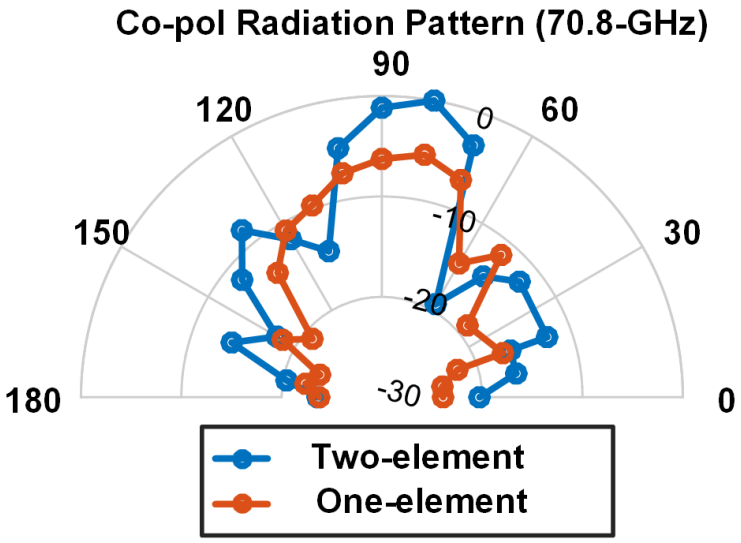

Figure 3.17: Measured normalized TX pattern with one-element and two-element TX.

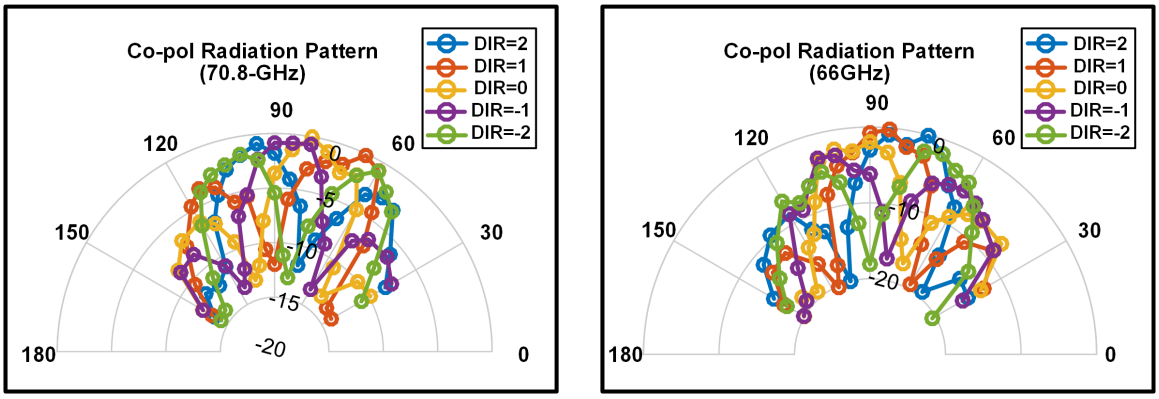

Figure 3.18: Measured mm-wave beamsteering by varying trigger pulse delay at 66GHz and 70.8GHz.

cm.

3.4 Conclusion to FSK/SSK TX

This chapter demonstrates low-power techniques to combine spatial modulation with frequency-shift keying in a mm-wave TX to enable energy-efficient short-range 10mm-wave links. A two-element TX prototype is implemented in 65-nm CMOS and is pack-

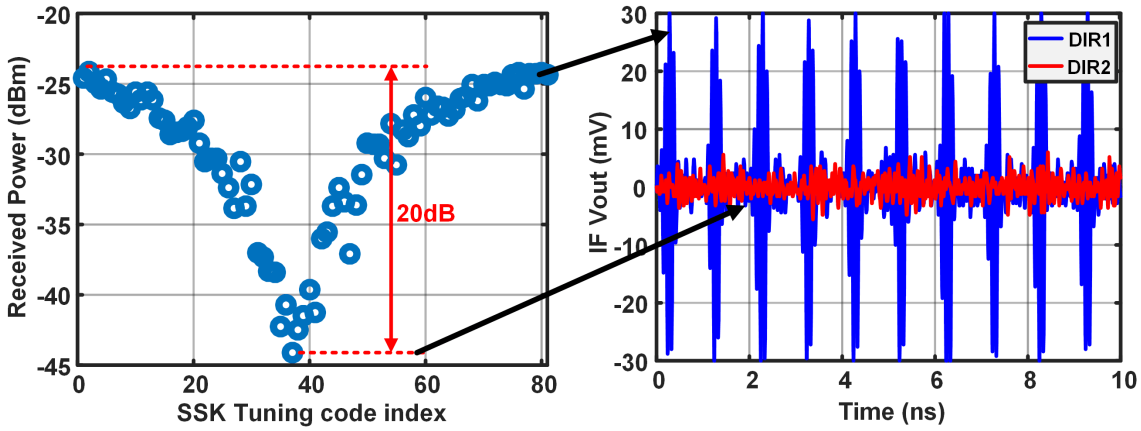

Figure 3.19: Measured peak-to-null ratio across delay for 2-element TX.

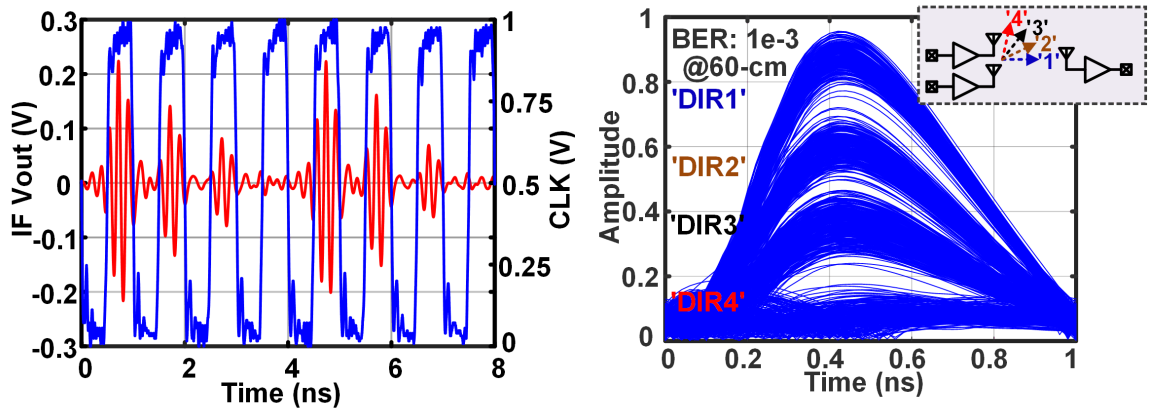

Figure 3.20: Measured 4-SSK eye diagram with 60-cm TX-RX separation.

aged with antennas on PCB, achieving 3 Gb/s data rates with energy efficiency of 7.1 pJ/bit.

	This Work	Taghivand, JSSC 15	Byeon, TMTT 13	Saponara, EuMIC 14	Wang, VLSI 10	Kong, ISSCC 13
Frequency	68 GHz	60 GHz	60 GHz	60 GHz	60 GHz	60 GHz
CMOS Technology	65 nm	40 nm	90 nm	65 nm	90 nm	65 nm
Modulation	FSK/Spatial	OOK	OOK	OOK	FSK	QPSK
Antenna	PCB Aperture Coupled Patch	On-chip Dipole	On-board Yagi-Uda	On-chip Dipole	On-board folded dipole	On-chip Slot Loop
EIRP (dBm)	0 (1 element) 6 (2 elements)	NA	4.4	11	0	-5 (1 element) 7 (4 element)
Data Rate (Gb/s) @ Range (m)	3 @ 0.6	2.45 @ 0.1	10.7 @ 0.1	2 @ 1.1	1 @ 1.04	10.4 @ 0.4
BER	1e-3	5e-5	1e-12	NA	1e-12	1e-7
Power (mW)	21.4	11.9	31	172	350	50 †
Energy/Bit (pJ/bit)	7.1	4.9	2.9	86	350	4.8 †
Energy/Bit/EIRP (pJ/bit/mW)	1.78	NA	1.05	6.83	350	0.96 †

† Power of PLL required for coherent QPSK not included.

Figure 3.21: Comparison to state of the art low-power mmWave TX

Chapter 4: Low-Power FSK/Spatial Modulation Receiver for mm-Wave Wireless Links

4.1 Introduction to Low-Power Spatial Modulation RX

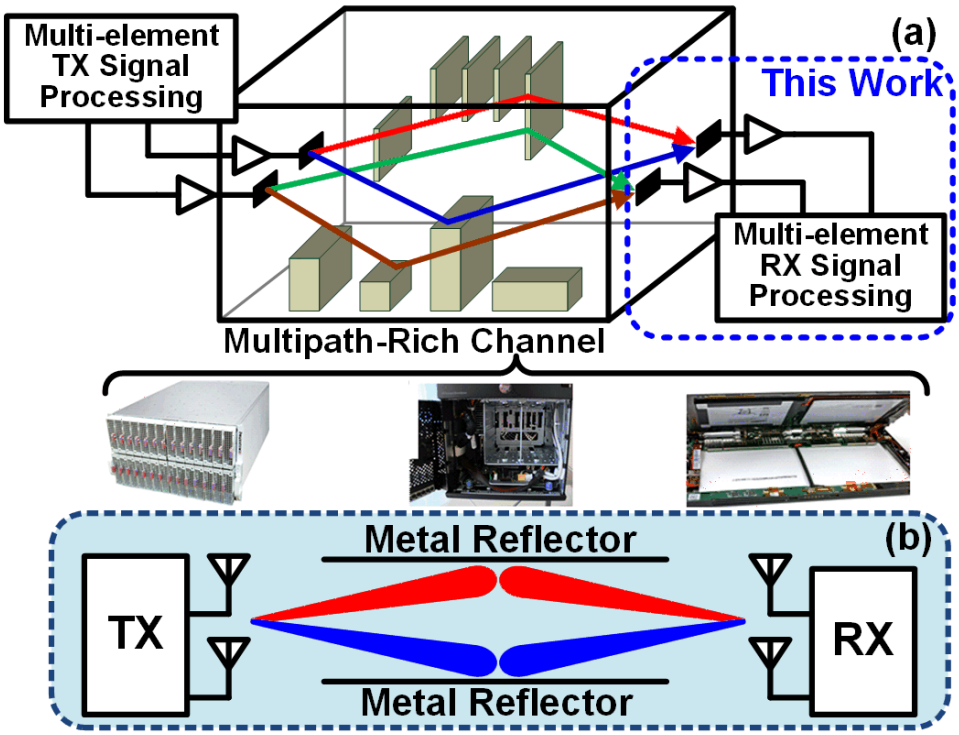

Figure 4.1: System overview of low-power mm-wave wireless interconnect within enclosed platforms using spatial modulation/space-shift keying (SSK).

The small physical size of multiple-antenna systems at mm-wave and the large available bandwidths make short-range high-speed mm-wave wireless links attractive. On-off keying (OOK) links have been proposed at these frequencies to achieve high energy-efficiency which is critical in short-range applications [18, 37]. FSK links can provide

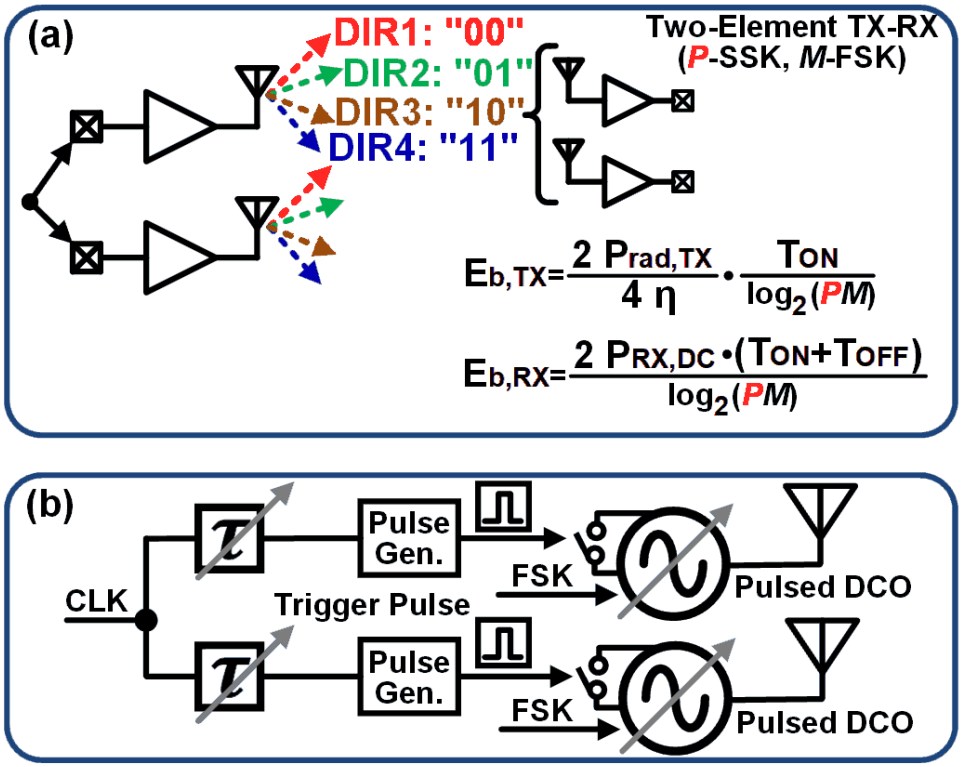

Figure 4.2: (a) Adding SSK to FSK improves RX and TX energy-efficiency, (b) Block diagram of low-power mm-wave 2-element TX with combined SSK and FSK [4].

improved robustness to interferers and multipath at the cost of higher power consumption compared to OOK [21, 38]. Energy efficiency can be improved by combining FSK with spatial modulation or space shift keying (SSK) where bits are mapped to directions in relatively static channels [1, 2, 4]. In such schemes, SSK is achieved using a multiple element transmitter (TX) to switch antennas or beam directions based on input data. SSK demodulation requires a receiver (RX) that can distinguish the angle-of-incidence (AoI) [2]. Such SSK links are well suited for board-to-board communication in reflective computing chassis where channels are slow-varying and contain transmit-direction dependent multi-path components (Fig. 4.1 [4]).

The improvement in TX and RX energy efficiency with SSK is shown in the $\log_2(P)$ term in Fig. 4.2 where P is the SSK modulation-depth. Efficient SSK TX must provide

low-power beam switching/steering without power overhead. Phased-array based beam-switching increases the effective isotropic radiated power (EIRP) for given array DC power compared to antenna-switching schemes. A low-power pulsed digital-controlled oscillator (DCO) phased-array scheme is presented in [4] to achieve beam-switching in the TX without the overhead of power-hungry phase shifting. In this work, a low-power two-element 66GHz - 70GHz FSK-SSK RX is presented that is capable of demodulating SSK and FSK signals concurrently. The SSK/FSK RX IC is packaged with antennas, demonstrating 3-Gb/s SSK-FSK link operation up to 40-cm (using horn-antenna based TX) and 2-Gb/s SSK-FSK link operation up to 6-cm using a 6-dBm EIRP FSK-SSK TX [39].

4.2 Design of Low-Power mm-Wave Two-Element FSK-SSK Receiver

While a multi-beam output phased array is attractive for the SSK RX since the array improves SNR, low-power operation is desired for high energy-efficiency. In order to detect both the SSK and Pulsed FSK signals while maintaining energy efficiency, we proposed two different architectures for the receiver: Series-FSK-SSK and Parallel-FSK-SSK. The series-FSK-SSK RX is described in section 4.2.1 and the parallel-FSK-SSK RX will be described in section 4.2.2.

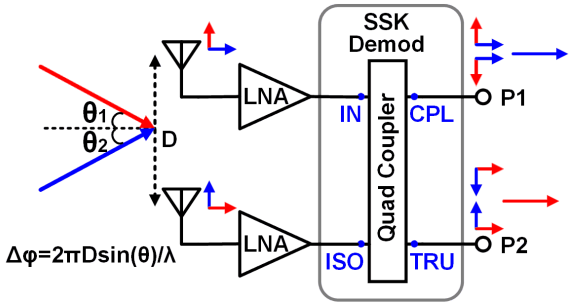

Figure 4.3: SSK demodulation scheme using quadrature coupler.

As shown in Fig. 4.3, the core of SSK demodulation scheme is the quadrature coupler that act as a fixed spatial filter [3]. The phase shift of the IN-to-THRU path and the ISO-to-COUPLED path are both $90°$, while the IN-to-COUPLED path and the ISO-to-

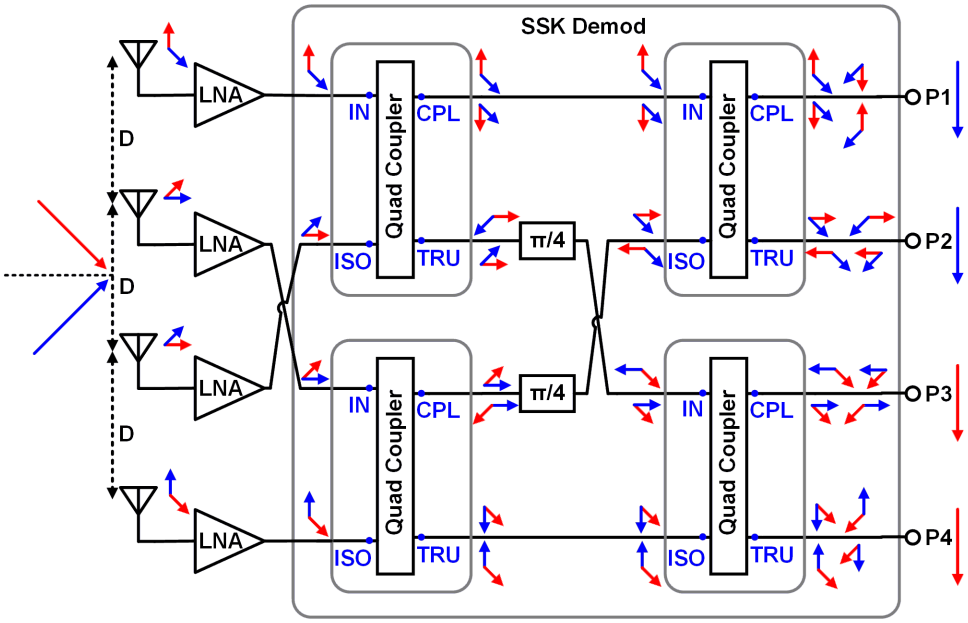

Figure 4.4: SSK demodulation scheme using 4X4 Butler matrix as spatial filter.

THRU port has 0° phase shift. The signal at the input of each LNA presents a phase difference directly corresponding to the angle-of-incidence. The signals at the IN and ISO port has the same phase difference because LNA in each elements are identical to each other. For one particular angle-of-incidence, the ISO is 90° delayed compare to the IN port, the signal from ISO-to-COUPLED is at 180° and will completely cancel out the signal at 0° from IN-to-COUPLED, thus create a null swing at the COUPLED port. Meanwhile the signals from IN-to-THRU and ISO-to-THRU are in phase and will constructively add up, thus create a peak swing at the THRU port. For another particular angle-of-incidence, the ISO is 90° advanced compare to the IN port, the peak swing happens at the COUPLED port while the THRU port has null swing. The angle-of-incidence can be demodulated by comparing the signal amplitude at the THRU and COUPLED port. Such architecture can be extended to N-element SSK RX with N LNAs followed by a N$\times$N Butler matrix to improve the SSK resolution (Fig. 4.4).

4.2.1 Architecture of Series-FSK-SSK Receiver

The block diagram and architecture of the proposed two-element series-FSK-SSK RX are shown in Fig. 4.5. In this architecture, a low-power LNA in each element amplifies the input signal which is provided to a quadrature coupler (Fig. 4.5) .

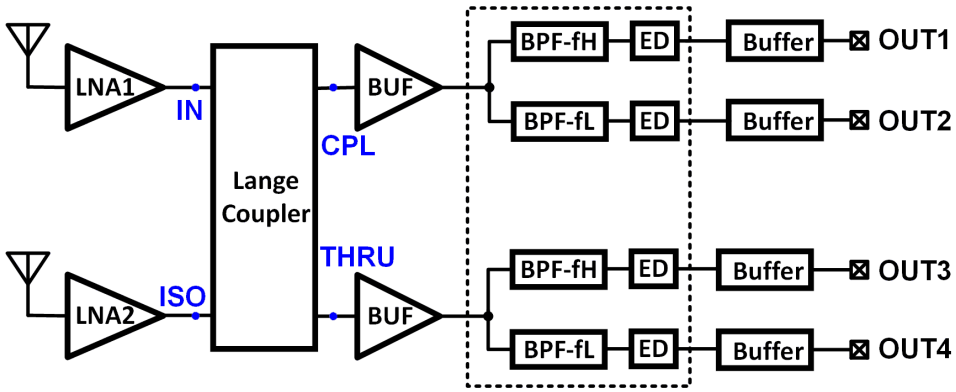

Figure 4.5: Architecture and block diagram of two-element mm-wave series-FSK-SSK RX in 65nm CMOS.

Each of the output ports of the coupler (COUPLED and THRU) in Fig. 4.5 are provided to an single-stage transformer-feedback buffer which drives two passive 4^{th}-order bandpass-bandstop filters BPF-fH and BPF-fL. The transfer function of BPF-fH provides a pass at frequency f_{High} and provides a notch at frequency f_{Low}. And vise versa BPF-fL provides a pass at frequency f_{Low} and a notch at frequency f_{High}. As shown in Fig 4.5, the FSK demodulation is achieved by comparing the relative outputs of $OUT1$ and $OUT2$ or the relative outputs of $OUT3$ and $OUT4$. while the SSK demodulation is by comparing the relative outputs of $OUT1$ and $OUT3$ or the relative outputs of $OUT2$ and $OUT4$. Overall the four passive bandpass-bandstop filters and envelope detectors achieves low-power non-coherent series-FSK-SSK detection. In the section 4.2.3, 4.2.4, 4.2.5 and 4.2.6, the design of each low-power series-FSK-SSK RX building block is described in details.

4.2.2 Architecture of Parallel-FSK-SSK Receiver

The block diagram and architecture of the proposed two-element parallel-FSK-SSK RX are shown in Fig. 4.6. The parallel-FSK-SSK and series-FSK-SSK have the same low-power LNA in each element for amplifying the input signal and the same quadrature coupler that acts as a fixed spatial filter (Fig. 4.6) [3]. Each of the coupler output ports (P1 and P2) in Fig. 4.6 are provided to both an envelope detector (ED) and an FSK demodulator. The FSK demodulator in each spatial path detects the transmit frequency while the signal Angle-of-Incidence can be determined by the relative outputs of $SSK1$ and $SSK2$, providing SSK demodulation. The SSK and FSK demodulation in parallel-FSK-SSK RX are operating in parallel. The FSK demodulator in parallel configuration consumes more power but provides better detection gain and better frequencies tunability for compensating process variations when comparing to the series configuration. The SSK demodulator in parallel configuration has higher input power level since no bandpass-bandstop filter is inserted before the ED and also better conversion gain due to the higher input power. In the following sections 4.2.3, 4.2.4, 4.2.5 and 4.2.7, the design of each low-power parallel-FSK-SSK RX building block is detailed.

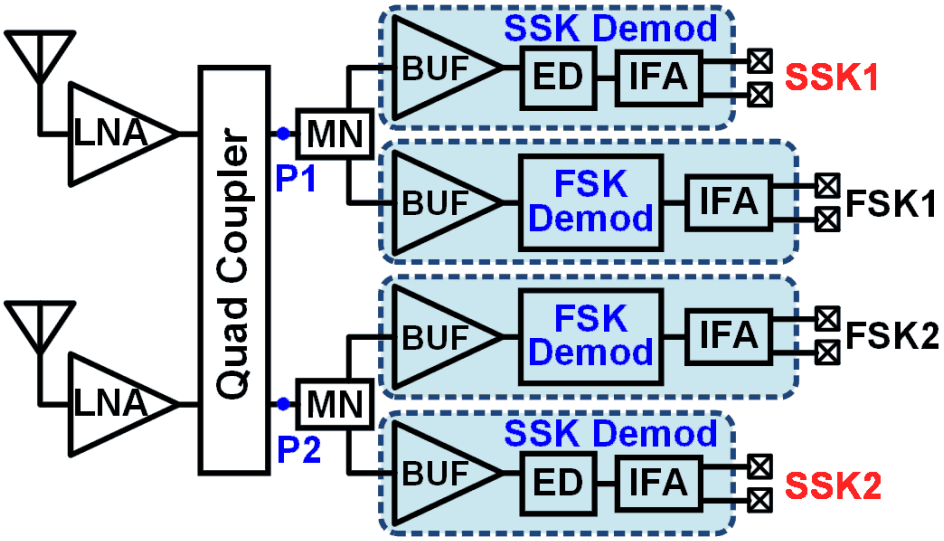

Figure 4.6: Architecture and block diagram of two-element mm-wave parallel-FSK-SSK RX in 65-nm CMOS.

4.2.3 Low-Power 68-GHz 6-Stage Transformer-Feedback LNA

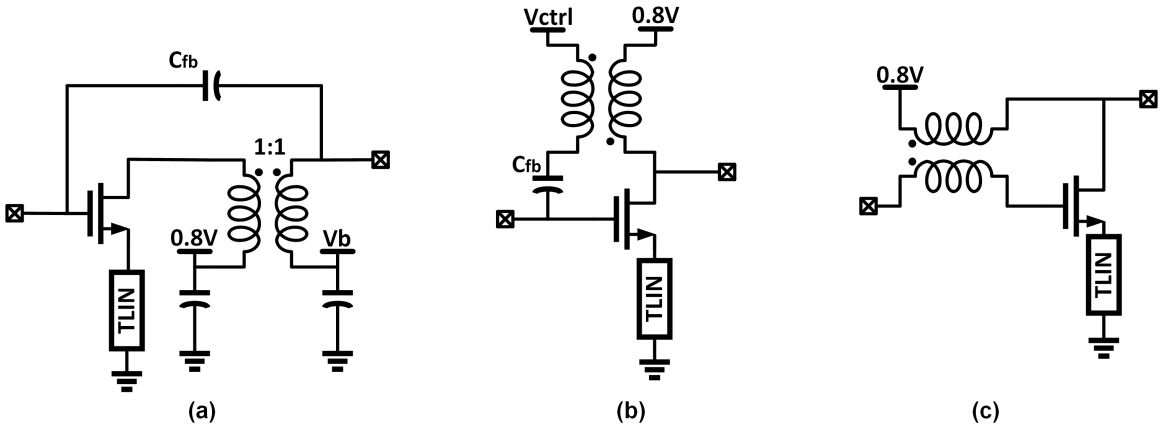

Figure 4.7: Comparison of drain-gate transformer feedback for LNA neutralization.

The LNA must simultaneously achieve low-power operation and high-gain for increasing link range, particularly since a low-power integrated SSK-FSK TX is assumed. We propose to use single-ended multiple stages of common-source LNA operating under low supply voltage 0.8V for achieving high gain with low power consumption. Drain-gate transformer feedback technique is used for LNA neutralization in order to improve maximum available gain each stage as well as reverse isolation. Fig. 4.7 shows three different drain-gate transformer feedback techniques. Fig. 4.7(a) use a 1:1 transformer as inter-stage matching network and the signal at the secondary of the transformer is feedback to the gate using a feedback capacitor with the advantage of combining the feedback mechanism within the interstate matching network [40]. The feedback capacitor is difficult to model and sensitive to unwanted signal coupling along the long feedback path. Fig. 4.7(c) implemented the secondary of the drain-gate feedback transformer as series inductor at the gate. This avoid the need of any feedback capacitor but create design challenges in optimizing the feedback strength as well as in layout placement [40]. In Fig. 4.7(b), the drain signal is picked up with low-K inverting transformer and feedback into gate with a feedback capacitor. The weakly coupling using low-K transformer avoids loading the drain inductor which can be optimized with best quality factor within the operating frequencies. Fig. 4.8 shows the EM model of the drain-gate

transformer with MOM capacitor as well as the guard ring used in the EM simulation. This drain-gate feedback technique also has the benefits of easy layout placement.

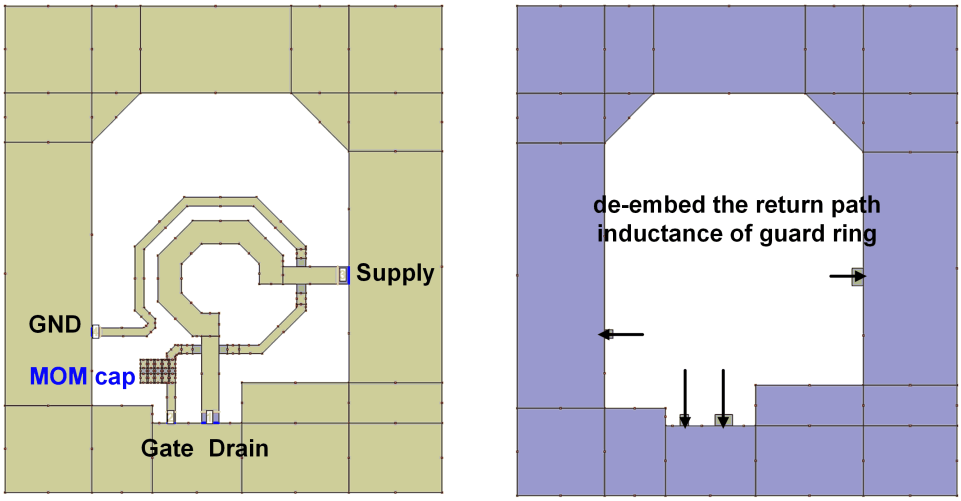

Figure 4.8: EM model of the drain-gate feedback transformer with MOM feedback capacitor.

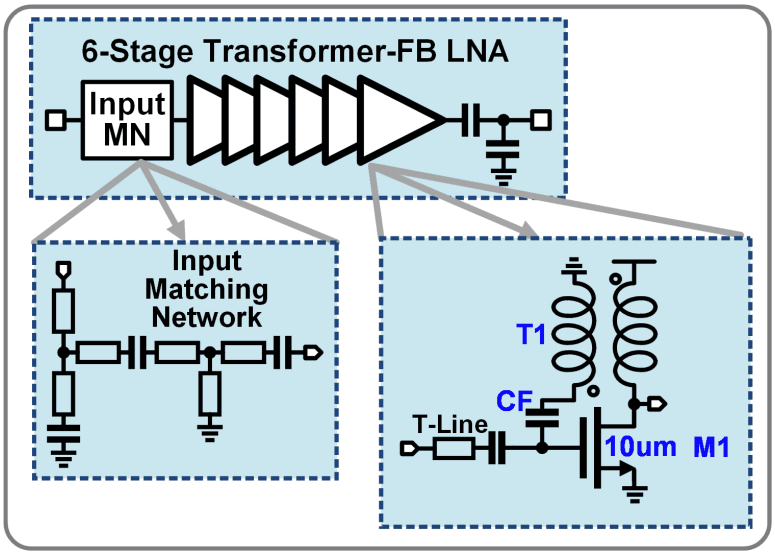

Figure 4.9: Schematic of the 6-stage transformer-feedback LNA in the proposed two-element mm-wave FSK-SSK RX in 65-nm CMOS.

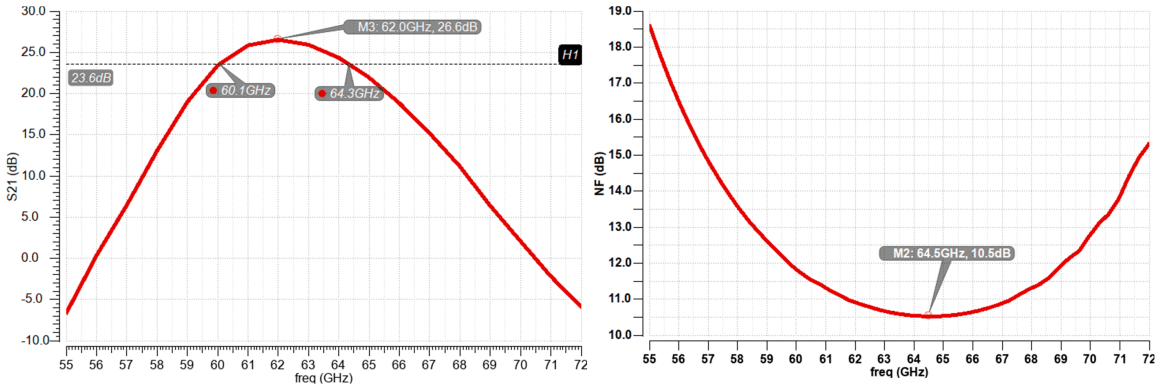

Figure 4.10: Simulated gain and noise figure of the proposed 6-stage drain-gate transformer feedback LNA in 65nm CMOS.

The schematic of the transformer-feedback 6-stage LNA with the input and output matching network is shown in Fig. 4.9. As mentioned earlier, Transformer T_1 couples the output back to the gate through capacitor C_F, effectively neutralizing C_{GD} of transistor M_1 and improving Gmax by 2.8dB at 70GHz and by 1.6dB at 62GHz for 2mA bias per stage. The transformer is implemented in a 3.4-μm thick top metal layer and feedback capacitor implemented using both 0.9-μm and 3.4-μm metal layers. The proposed approach leads to 27.3-dB simulated LNA-gain with 9.6-mW power consumption from a 0.8-V supply. The LNA output is matched to 50-Ω using a series capacitor and a shunt capacitor to drive the coupler. A laser-trim based test-point is included to measure standalone LNA gain. Fig. 4.10 shows the simulated performance of the 6-stage transformer feedback LNA. We design the LNA at 62GHz, assuming the frequency will go up by 10$\%$ based on the measurements result of an previous prototype IC. The simulated noise figure of the LNA is 10.5dB due to the lack of optimization in the LNA input matching network. The input matching network and EM simulation of the drain-gate feedback transformer needs to be carefully re-optimized in order to improve the LNA performance for possible re-use in other low power mm-wave transceiver design.

4.2.4 Compact 68-GHz Quadrature-Hybrid Coupler

A compact Lange quadrature coupler is implemented using edge-coupled lines, implemented in the 3.4-μm and 0.9-μm thick top two metal layers (Fig. 4.11. The simulated performance of the quadrature coupler is summarized in Fig. 4.12.The 50-Ω coupler only occupies 380μm$\times$50μm and achieves 3.7-dB insertion loss at 67GHz for IN-THRU, IN-CPL, ISO-THRU, ISO-CPL. The phase difference between THRU and CPL is 88° and THRU and CPL-port amplitude mismatch is $< \pm 0.5$ dB from 61 GHz to 80 GHz. The isolation between IN and ISO is -16dB. The area of the compact quadrature coupler can be further reduced with meandering.

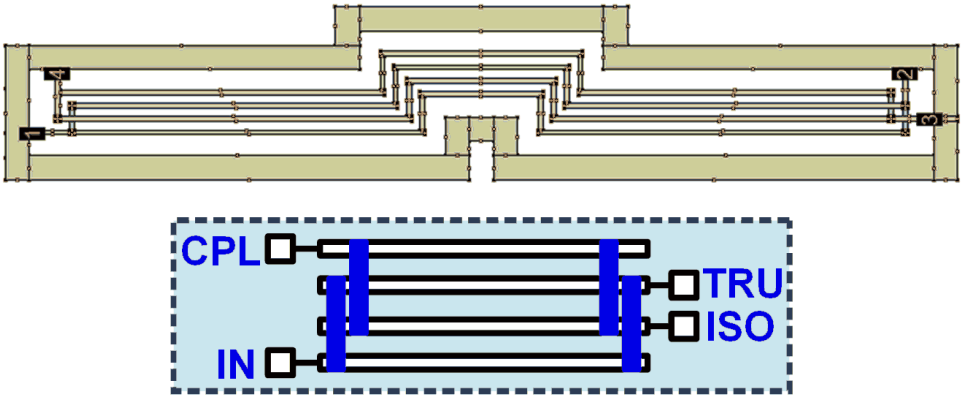

Figure 4.11: EM model and schematic of the compact broadband 68GHz Lange Coupler.

4.2.5 SSK Demodulation and Design of Envelope Detector

The proposed scheme of SSK demodulation requires the detection of the signal magnitude at each quadrature coupler output. Thus an envelope detector (ED) can be implemented as the core block of low-power SSK demodulation. Such ED needs to have high conversion gain with low-power operation and short settling time enabling support for multi-Gb/s SSK detection. Envelope detector typically consists of a rectifier [41–44] followed with a low pass filter. Fig. 4.13 shows the schematic of two different envelope detectors that can be used for low-power SSK detection. A differential ED ([5, 37]) is selected to avoid sensitivity to supply and ground bounce which requires an input balun

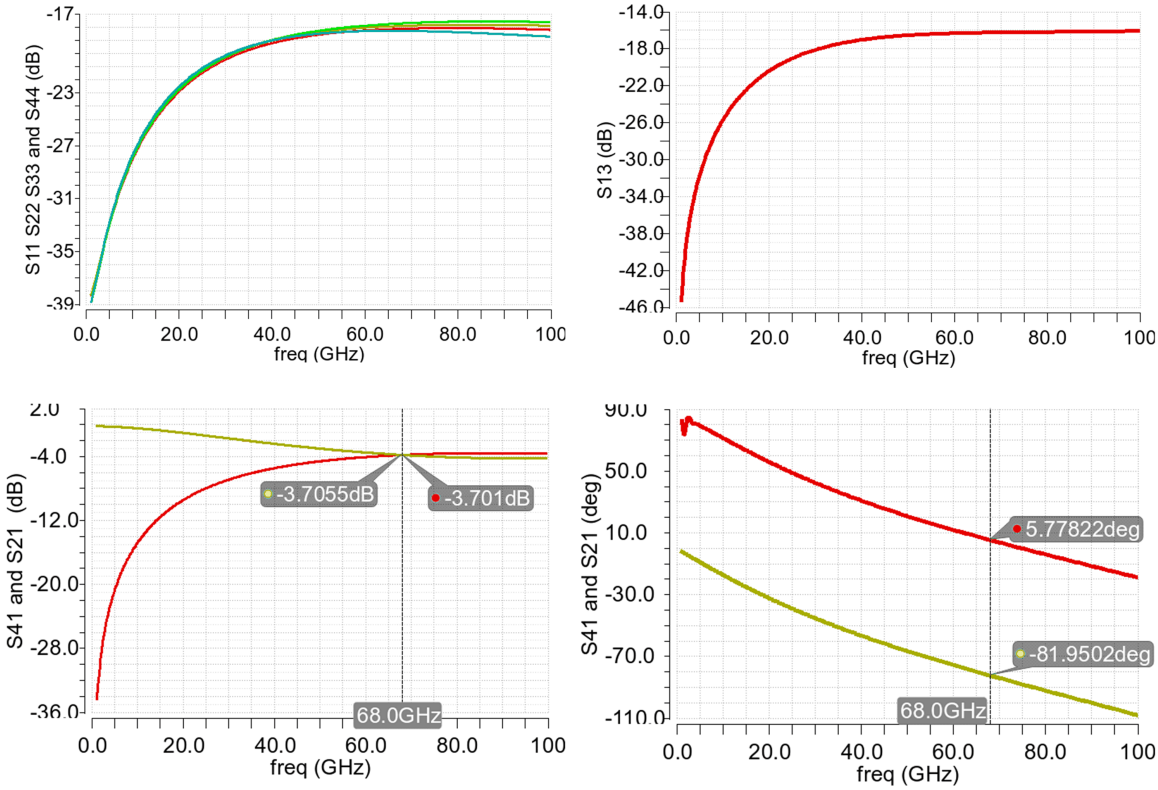

Figure 4.12: Simulated performance of the compact broadband Lange Coupler (Port1: IN, Port2: THRU, Port3: ISO, Port4: Coupled).

to translate the single-ended coupler output to differential signals. A drain-connected nmos pair is acted as the rectifier and gain-boosting load improve the conversion gain. The differential RF signal is applied to gate only in Fig. 4.13(a) and both gate and source in Fig. 4.13(b). With twice the input swing, the ED in Fig. 4.13(b) has better conversion gain but poorer quality factor of the input impedance due to the source degeneration inductor. In Series-FSK-SSK RX, the input impedance of ED will load the preceding bandpass-bandstop filter and in parallel-FSK-SSK RX, the input impedance of ED will reduce the gain the preceding buffer. Thus the ED in Fig. 4.13(a) is used in our design. The ED consumes 1.9mA and provides a responsivity of $\sim 0.33\,\mathrm{V}/V_{PK-PK}$ for small mm-wave input at the ED. The pre-buffer driving the ED consumes 1.2mA. Fig. 4.14 shows the transit simulation of the ED with different input swing at the gate. The sim-

ulation also shows the ED can settle down within 100ps and enabling multi-Gb/s SSK demodulation.

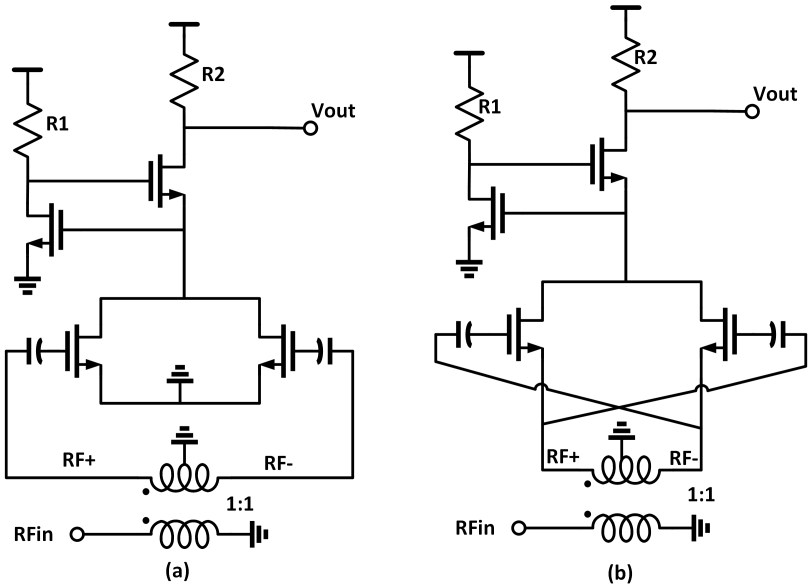

Figure 4.13: Schematic of the envelope detector used for low-power SSK detection [5].

4.2.6 Bandpass-Bandstop Filter for Series-FSK-SSK RX

Fig. 4.15 shows the schematic of the bandpass-bandstop filter used for FSK demodulation in the series-FSK-SSK RX. Each bandpass-bandstop filter consist of a series LC tank and a shunt LC tank. For a LC tank with quality factor Q, the impedance Z_{tank} can be expressed as

$$\mid Z_{tank} \mid = \frac{\omega LQ}{\sqrt{1+Q^2(1-\omega^2 LC)^2}} \tag{4.1}$$

The voltage gain of the bandpass-bandstop filter is

$$\frac{V_{out}}{V_{in}} = \frac{\frac{\omega L_2 Q_2}{\sqrt{1+Q_2^2(1-\omega^2 L_2 C_2)^2}}}{\frac{\omega L_1 Q_1}{\sqrt{1+Q_1^2(1-\omega^2 L_1 C_1)^2}} + \frac{\omega L_2 Q_2}{\sqrt{1+Q_2^2(1-\omega^2 L_2 C_2)^2}}} \tag{4.2}$$

The series LC tank is resonate at ω_1 and the shunt LC tank is resonate at ω_2. The voltage

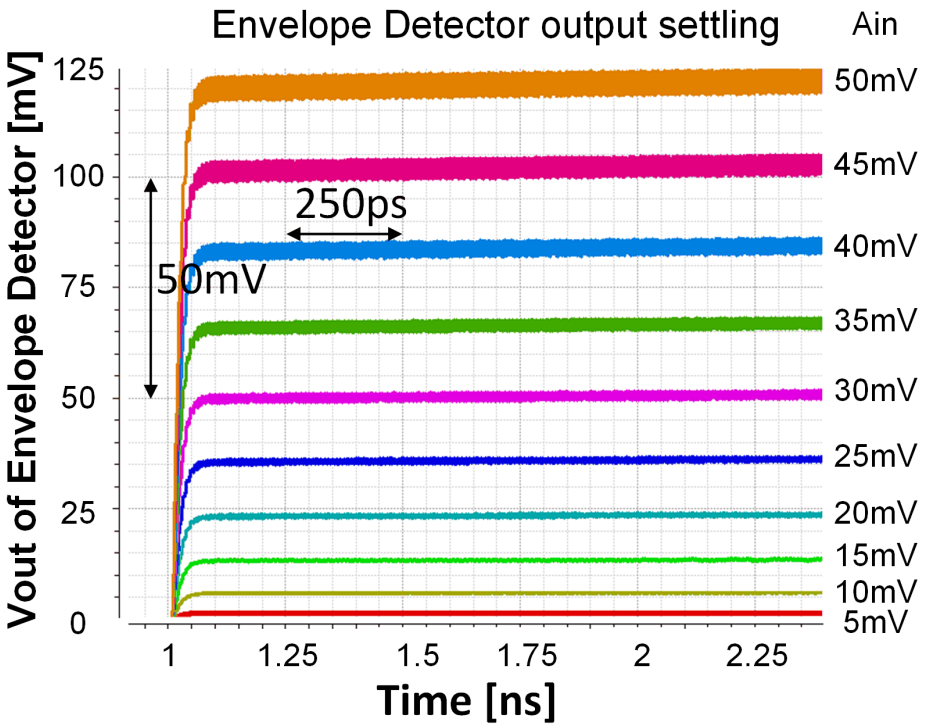

Figure 4.14: Simulated performance of the proposed envelope detector in 65nm CMOS.

gain of the bandpass-bandstop filter at the two resonate frequencies can be expressed as

$$\begin{aligned} \frac{V_{out}}{V_{in}}\,|_{\omega_1} &= \frac{\omega_1 L_2 Q_2}{\omega_1 L_1 Q_1 \sqrt{1+Q_2^2(1-\omega_1^2 L_2 C_2)^2} + \omega_1 L_2 Q_2} \\ \frac{V_{out}}{V_{in}}\,|_{\omega_2} &= \frac{\omega_2 L_2 Q_2}{\omega_2 L_1 Q_1 / \sqrt{1+Q_1^2(1-\omega_2^2 L_1 C_1)^2} + \omega_2 L_2 Q_2} \end{aligned} \tag{4.3}$$

Assume the quality factors of both LC tanks are 15, and the two frequencies used in the FSK modulation is ω_1 =66GHz and ω_2 =70.5GHz. The terms $\alpha_1 = \sqrt{1+Q_2^2(1-\omega_1^2 L_2 C_2)^2}$ and $\alpha_2 = \sqrt{1+Q_1^2(1-\omega_2^2 L_1 C_1)^2}$ are 2.1, 2,3 respectively and is increasing with better quality factor or wide frequency separation. Such two terms α_1 and α_2 is directly related to the peak-to-null ratio of the bandpass-bandstop filter. Overall the series LC tank create a null at frequency ω_1 and the shunt LC tank create a peak at frequency ω_2.

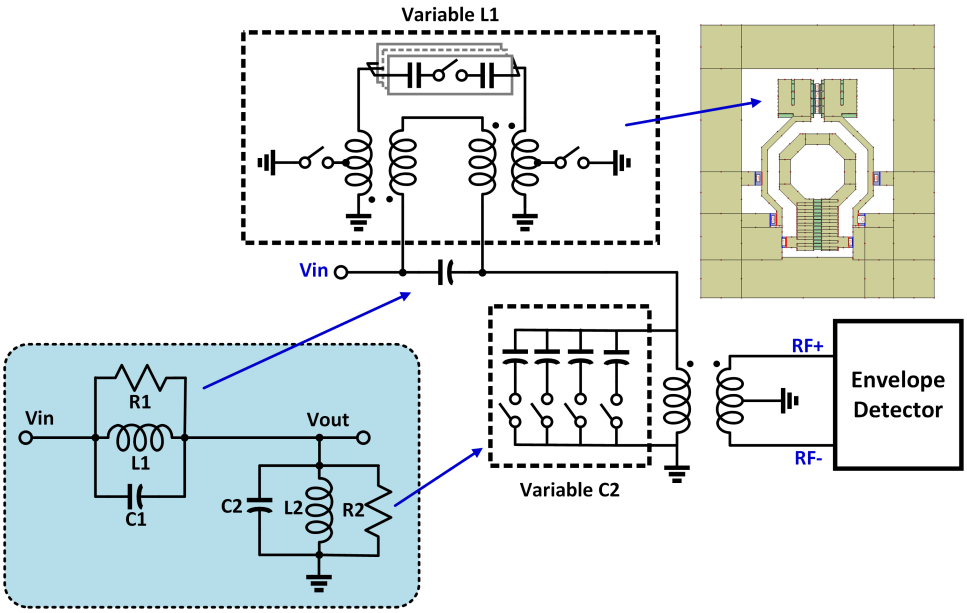

Figure 4.15: Schematic of the bandpass-bandstop filter used for FSK detection in Series-FSK-SSK RX.

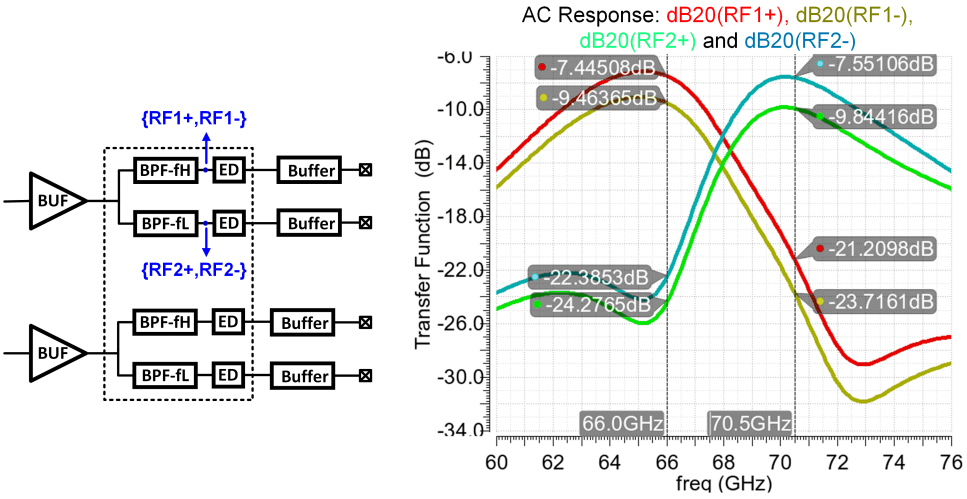

Figure 4.16: Simulated frequency response of the bandpass-bandstop filter.

The peak-to-null ratio and the passband gain can be approximately as

$$\begin{aligned} \text{Peak-to-Null ratio} &\approx \frac{R_2 + \alpha_1 R_1}{R_2 + R_1/\alpha_2} \\ \text{Passband Gain} &\approx \frac{R_2}{R_2 + R_1/\alpha_2} \end{aligned} \tag{4.4}$$

Improving the quality factor and increasing the frequency separation can improve both the peak-to-null ratio and passband gain. Increasing the ratio of R_1/R_2 improve the peak-to-null-ratio but making the passband gain worse. As showed in Fig. 4.15, the inductor L_1 is coupled to the secondary inductor with switchable return path to ground ring and loaded with custom switchable cap bank, in order to make the equivalent L_1 tunable. C_2 is also tunable. The input impedance of the envelope detector is lumped into the shunt LC tank design. The bandpass-bandstop filter is optimized to get better peak-to-null ratio with compromise in passband gain. The tunability of the filter is limited due to the requirement of high Q for better peak-to-null ratio and passband gain. Fig. 4.16 shows the simulated frequency response of the two bandpass-bandstop filters used in the series-FSK-SSK RX. The filter have $\sim$12dB peak-to-null ratio and $\sim$10dB loss with two FSK frequencies at 66GHz and 70.5GHz.

4.2.7 FSK Demodulator for Parallel-FSK-SSK RX

The FSK demodulator/discriminator in parallel-FSK-SSK RX consists of a transformer-based power splitter that divides the input signals into two paths, with one path goes through a frequency-dependent phase shifter (Fig. 4.17). The other path directly goes to the input of a phase detector. Such phase detector translates the relative phase difference between the two paths to a voltage output, achieving frequency discrimination. The frequency-dependent phase shift is accomplished using a LC resonator whose center frequency can be tuned through static switches. The phase shift of the LC resonator is

$$\begin{aligned} \Phi(\mathrm{Z_{tank}}) &= \arctan\left[\frac{R_p}{\omega L}(1-\omega^2 LC)\right] \\ &= \arctan\left[Q(1-\omega^2 LC)\right] \end{aligned} \tag{4.5}$$

A programmable negative resistance cell provides higher resonator-Q [45–49] and hence increased phase variation across frequency when enabled.

Fig. 4.17 also shows the schematic of the phase detector. The PD is implemented based on a Gilbert-cell like mixer with tunable current bleeding to improve the conver-

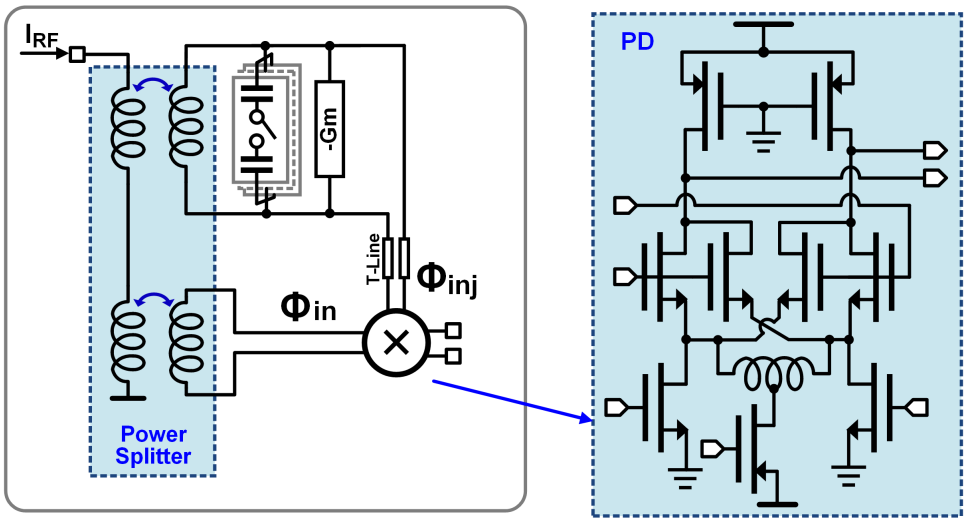

Figure 4.17: Schematic of the phase detector and the FSK demodulator used in Parallel-FSK-SSK RX.

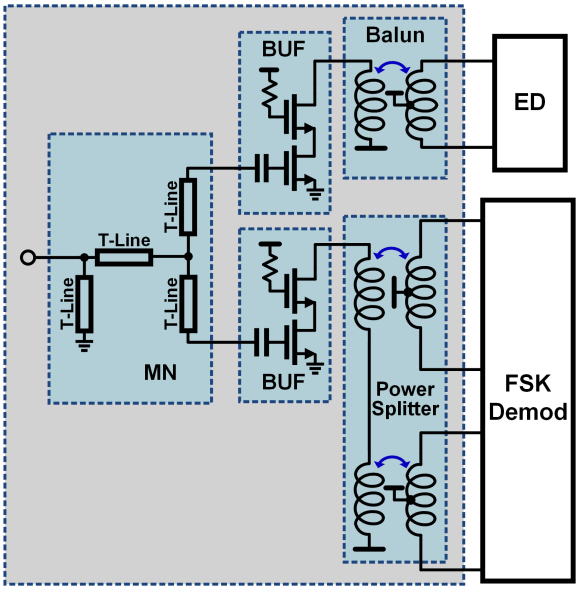

Figure 4.18: Schematic of the matching network and buffer between quadrature coupler and Parallel-FSK-SSK Demodulators.

sion gain while maintain the hard switch of the switch-quad. A shunt trap inductor is tapped to the source of the switch-quad also for improving conversion gain. The bleed

current is applied into the center-tap of the shunt trap inductor. Fig. 4.18 shows the schematic of the single cascode stage buffer preceding the FSK demodulator and SSK demodulator. The primary side of the transformer-based power splitter and the balun used in the FSK and SSK demodulator also acted as the load inductor of the preceding buffer stage. The input of two buffers are together matched to 50Ω and connected to each of the quadrature coupler output. The demodulator including pre-buffer consumes 4.45 mA (3.96 mA) with the negative gm-cell enabled/disabled.

4.2.8 CPWG-Fed Aperture Coupled Patch Antenna on PCB for FSK-SSK RX

CPWG-fed aperture coupled patch antenna is designed on a low-cost IT-180TC PCB. The CPWG-fed instead of microstrip-fed is used here to reduce the radiation of the feed-line and to improve the front-to-back-ratio of the radiation pattern. The antenna dimensions, PCB stack-up and simulated input matching and the antenna radiation pattern are included in Fig. 4.19. The simulation shows the antenna achieving $\sim$4.6dB gain and is matched from 63GHz to 73.8GHz. The front-to-back-ratio is 10.6dB.

Fig. 4.20 shows the antenna array consisting of two CPWG-fed aperture-coupled patch antenna with spacing of λ. The CPWG-fed is bend 90 $\circ$ to align the polarization and beamsteering plane with the TX antenna array. The IC is packaged with the antenna on PCB using a bondwire LCL-matching scheme [32]. Fig. 4.21 shows the LCL-matching structure and the simulated loss. This LCL-matching scheme is similar to the one used in the TX package except differential antenna is used in TX while single-ended antenna is used in RX. The LCL-matching has $<$1dB loss in the RX operating frequency range.

4.3 Measured Performance of mm-Wave FSK-SSK RX

The two-element 68-GHz FSK-SSK RX is implemented using both the series-FSK-SSK and parallel-FSK-SSK configurations in a 65-nm CMOS process with 9 metal layers. The series-FSK-SSK RX occupies 1.32mm^2 and the die photo is shown in Fig. 4.22.

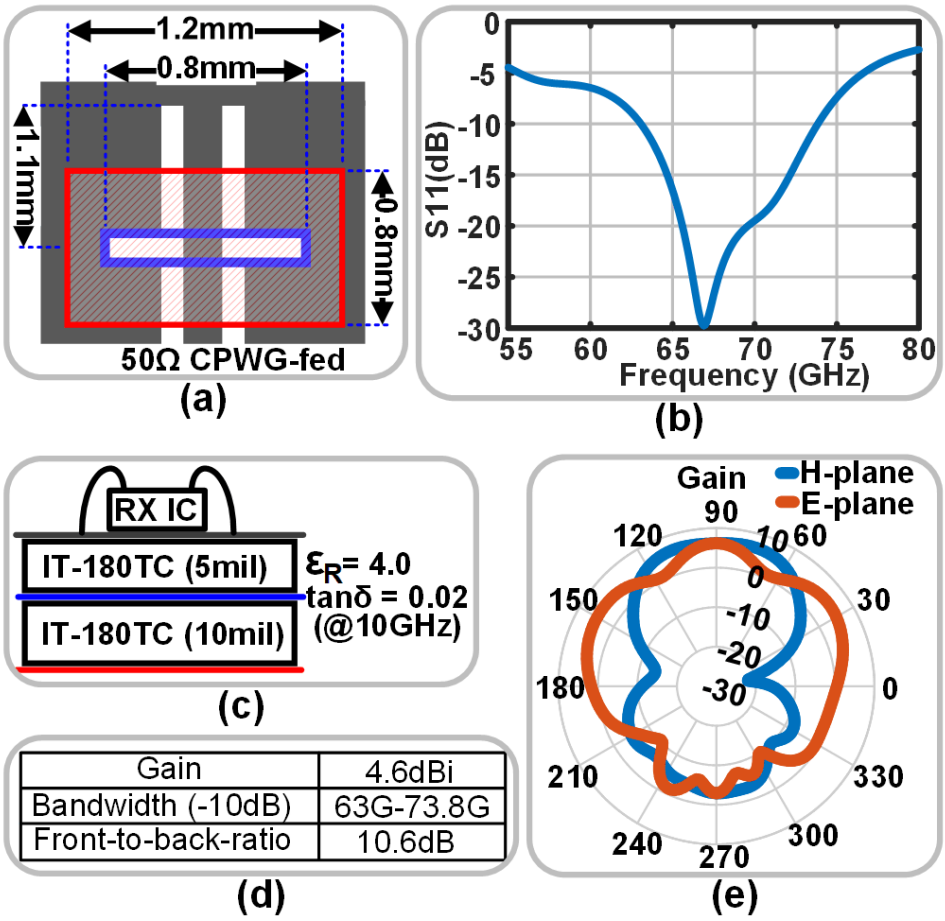

Figure 4.19: CPWG-fed aperture-coupled patch antenna in IT-180TC PCB: (a) Antenna dimensions; (b) Simulated S11 shows wideband impedance matching for the antenna; (c) PCB stack-up; (d) Summary of simulated antenna performance; (e) Simulated antenna gain.

While the parallel-FSK-SSK RX occupies 1.375 mm^2 and the die photo is shown in Fig. 4.23. The IC is packaged with CPWG-fed aperture coupled patch antennas using chip-on-board approach and the packaged IC is also shown in Fig. 4.23.

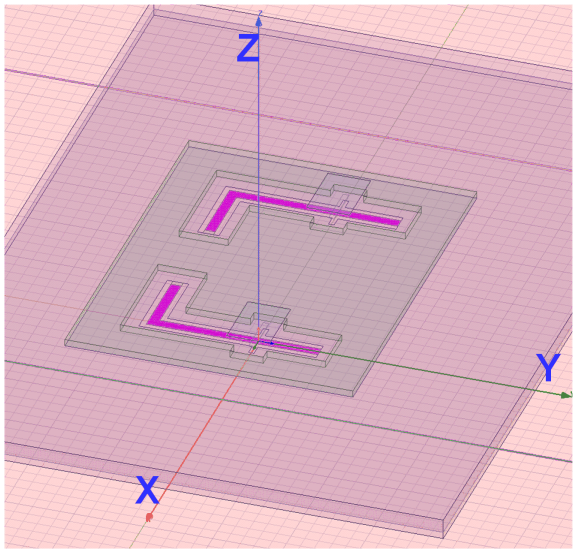

Figure 4.20: HFSS model of the CPWG-fed aperture-coupled patch antenna array.

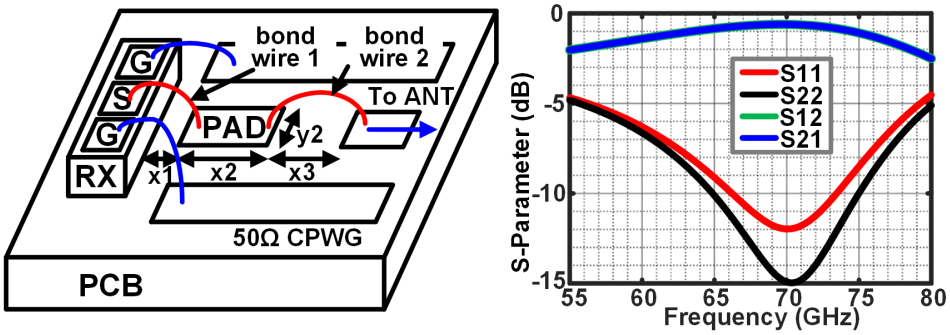

Figure 4.21: L-C-L bondwire matching structure for RX LNA GSG input and simulated loss of such L-C-L structure.

4.3.1 DC Power Consumption of FSK-SSK RX

The DC power consumption of both series-FSK-SSK RX and parallel-FSK-SSK RX are listed in Fig. 4.24. The FSK and SSK demodulator combined consumes 15.9mW in the parallel-FSK-SSK RX comparing to the 10.07mW in the series-FSK-SSK RX. The LNA in parallel-FSK-SSK is operating in low gain mode. The total DC power consumption is 32.76mW and 29.6mW respectively for the series-FSK-SSK RX and the parallel-FSK-SSK RX.

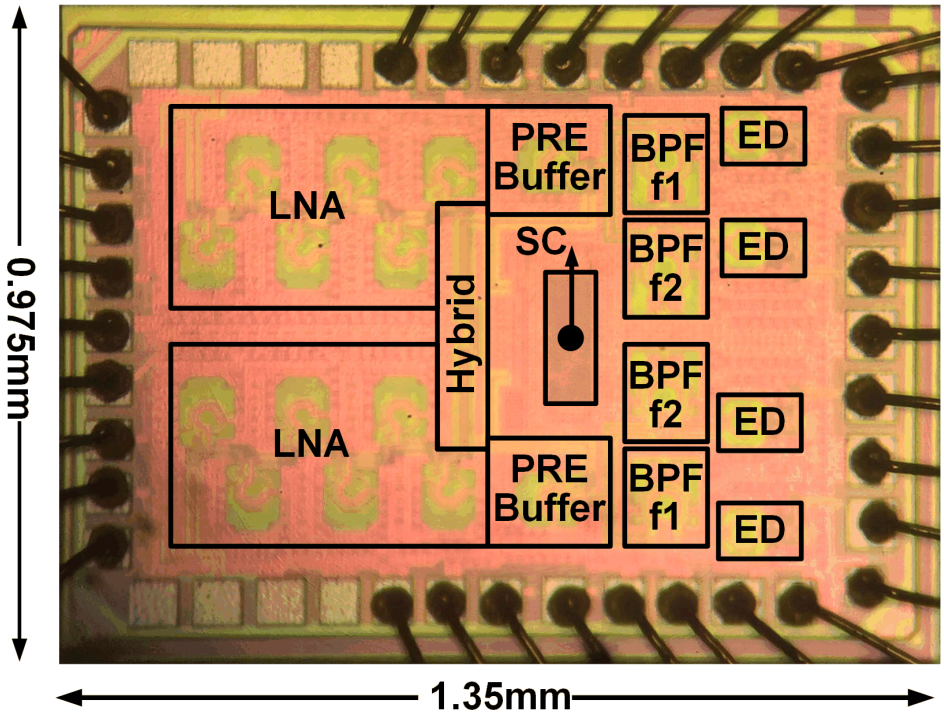

Figure 4.22: Die photo of the two-element mm-wave Series-FSK-SSK RX fabricated in 65nm CMOS.

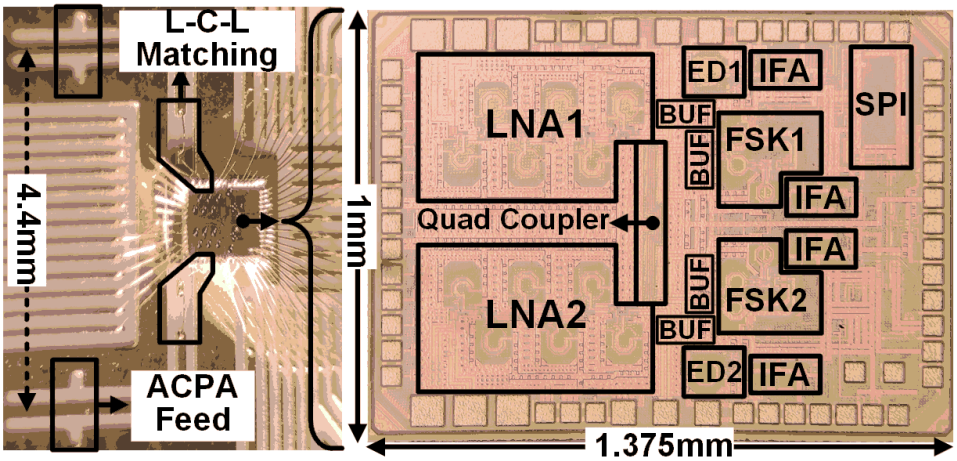

Figure 4.23: Two-element mm-wave Parallel-FSK-SSK RX packaged with PCB antennas using chip-on-board approach with PCB wirebonds for impedance matching.

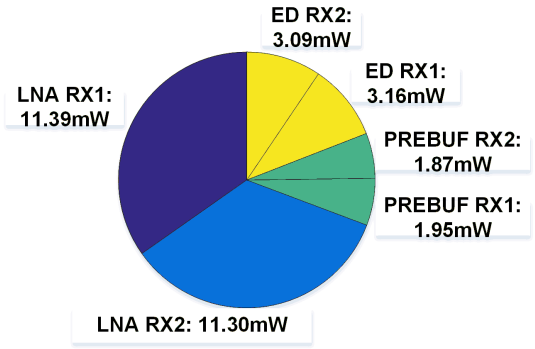

	Power Consumption (mW)
LNA RX1	11.39
LNA RX1	11.30
PREBUF RX1	1.95
PREBUF RX2	1.87
ED RX1	3.16
ED RX2	3.09
Total	32.76

(a) Series-FSK-SSK Receiver

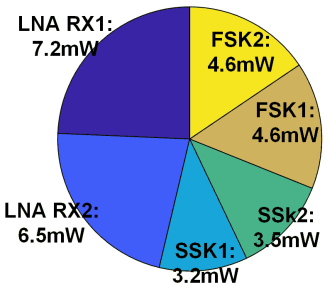

	Power Consumption (mW)
LNA RX1	7.2
LNA RX2	6.5
SSK1 (BUF+ED)	3.2
SSK2 (BUF+ED)	3.5
FSK1 (BUF+PD)	4.6
FSK2 (BUF+PD)	4.6
Total	29.6

(b) Parallel-FSK-SSK Receiver

Figure 4.24: DC power consumption of the Two-element Series-FSK-SSK RX and the Two-element Parallel-FSK-SSK RX.

4.3.2 Series-FSK-SSK RX Measurements

The series-FSK-SSK RX is characterized using a probe-based measurement setup (Fig. 4.25). A directional coupler splits the mm-wave signal into two paths. One path goes to a GSG probe and the other one goes to a phase shifter before goes to another GSG probe. The phase shifter helps emulate signal coming from different SSK directions. Fig. 4.26 shows the measured receiver output with CW of different frequencies and various input power levels, indicating the LNA is starting saturated when P_{in} >-20dBm and the LNA is peaking at ~72GHz which is 6% higher than the targeted frequency.

The FSK demodulation capability of the series-FSK-SSK RX is demonstrated by measuring both the RX OUT2 and RX OUT3 with the CW of different frequencies. As shown in Fig. 4.27, the series-FSK-SSK RX can distinguish the frequency by comparing RX OUT2 and RX OUT3. Such RX can support FSK demodulation with choosing the two frequencies as 70.5GHz and 74GHz. The angle-of-incidence can be demodulated by comparing RX OUT1 and RX OUT3 as showed in Fig. 4.28

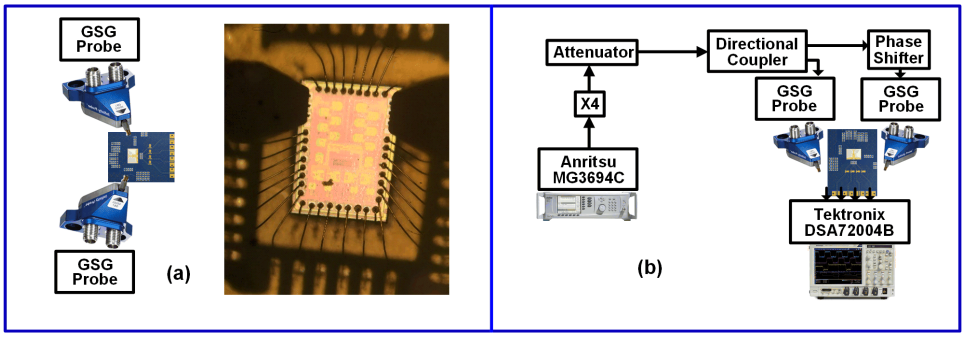

Figure 4.25: Measurements setup for the two-element mm-wave series-FSK-SSK RX.

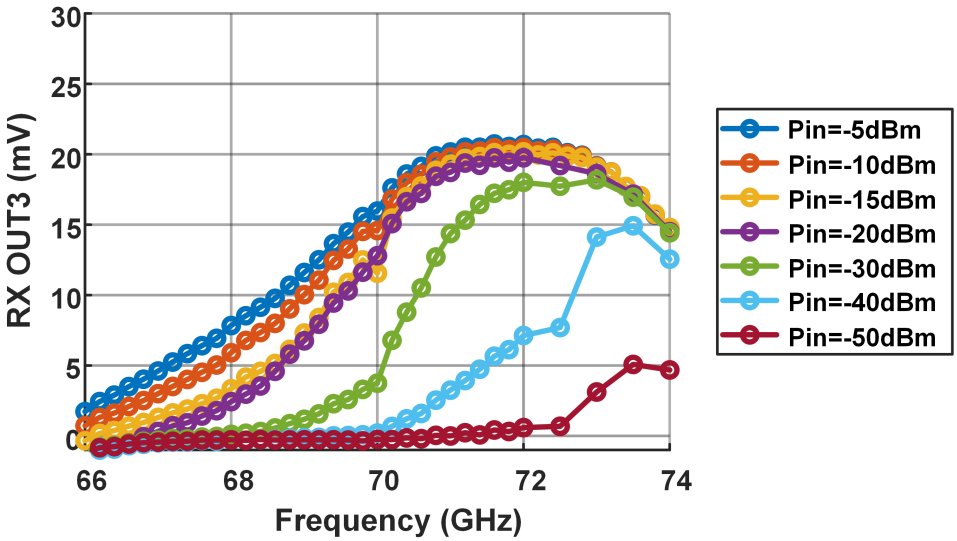

Figure 4.26: Measured receiver gain of the Series-FSK-SSK RX using probe test indicating the LNA in Series-FSK-SSK RX is tuned 6% higher in frequency.

4.3.3 Parallel-FSK-SSK RX Measurements

The two-element parallel-FSK-SSK RX is measured both using probe test and wireless measurements (Fig. 4.29).

Measured LNA performance based on probe-level measurements is shown in Fig. 4.30. The LNA achieves 28.5dB gain at 68.3GHz with a 3-dB bandwidth of 3-GHz while drawing 14-mA, demonstrating close to simulated performance. The IC is packaged with aperture coupled patch antenna on PCB enabling PCB-level wireless measure-

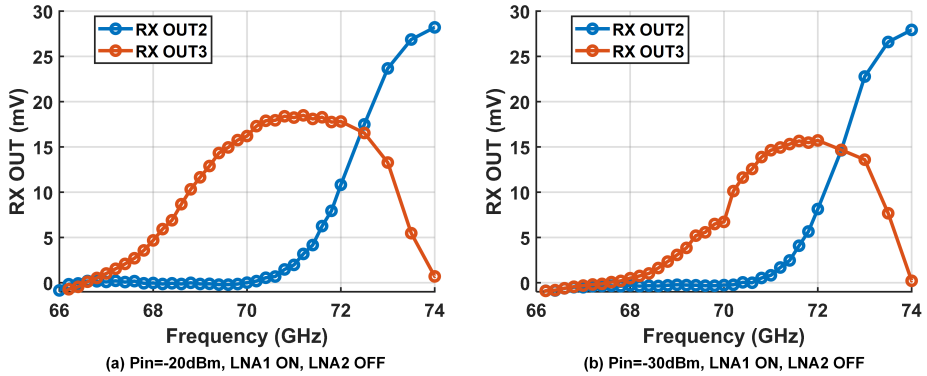

Figure 4.27: Measured frequency response of Out2 and Out3 in Series-FSK-SSK RX with LNA1 ON and LN2 OFF for (a) Pin=-20dBm, and (b) Pin=-30dBm. The measurements demonstrated the FSK demodulation capability of the Series-FSK-SSK RX.

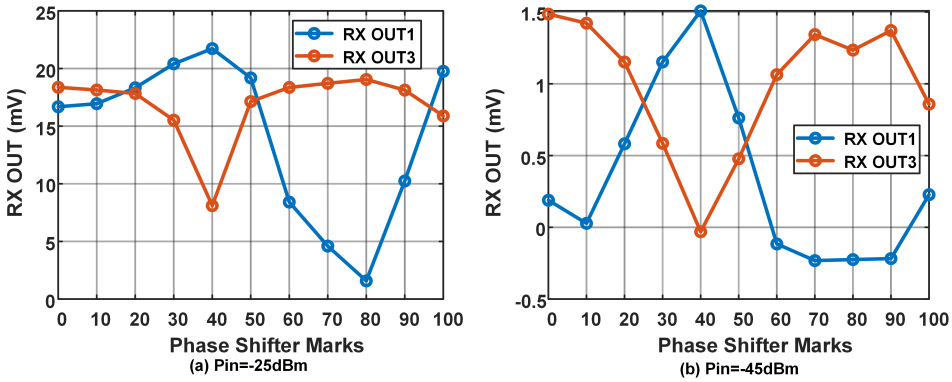

Figure 4.28: Measured Out1 and Out3 in Series-FSK-SSK RX with both LNA on across various phase differences between the two LNA, mimicking received signals with different angle-of-incidence. The measurements demonstrated the SSK demodulation capability of the Series-FSK-SSK RX.

ments. PCB-level measurements were measured at lower LNA bias current due to oscillation observed at highest gain in packaged PCB (with supply and ground through wirebonds) at one LNA. Fig. 4.31 shows the measured sensitivity of the parallel-FSK-SSK RX including the antenna-on-PCB and wirebonds at different LNA bias voltages and different LNA combinations.

Fig. 4.32 shows the measured performance of the FSK demodulator across frequency with and without the negative-gm cell enabled. As shown in Fig. 4.32(a,b), the discrim-

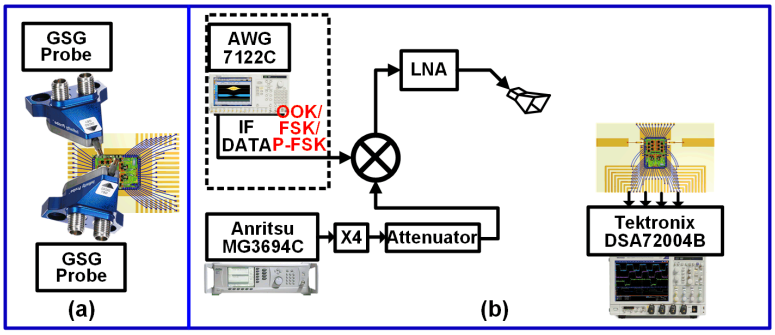

Figure 4.29: Measurements setup for the two-element mm-wave parallel-FSK-SSK RX.

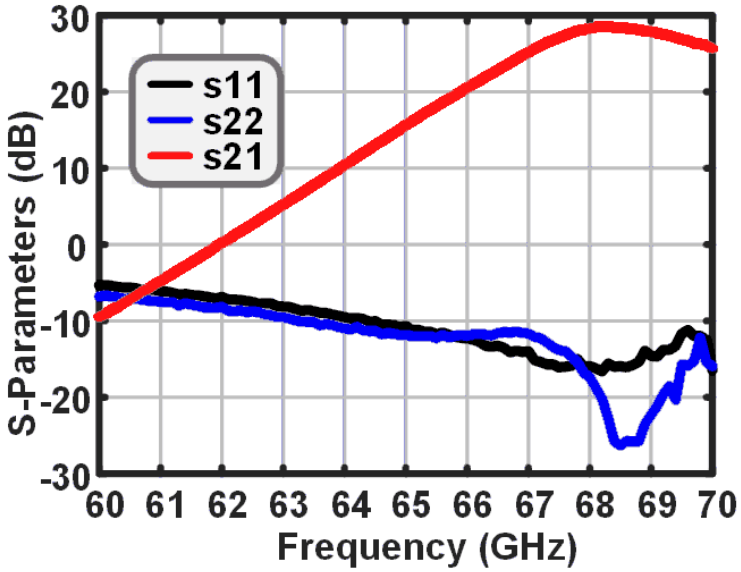

Figure 4.30: Measured LNA gain, input and output matching with probe testing.

inator is able to convert frequency to amplitude. The null frequency can be tuned by programming the LC resonator while the negative-gm cell increases discriminator slope across frequency. BER measurements on the RX are performed with a pulsed FSK signal where signal frequency is switched between 67-GHz and 69-GHz. As shown in Fig. 4.33, 1-Gb/s pulsed FSK measurements show $< 10^{-6}$ BER up to 45 cm. At 2.4-Gb/s BER of $< 10^{-3}$ is achieved up to 30 cm with pulsed-FSK (50% duty cycle).

Fig. 4.34 shows the measurement setup of the SSK BER test using single horn antenna as TX. The two-element IC is packaged with antennas with λ spacing between

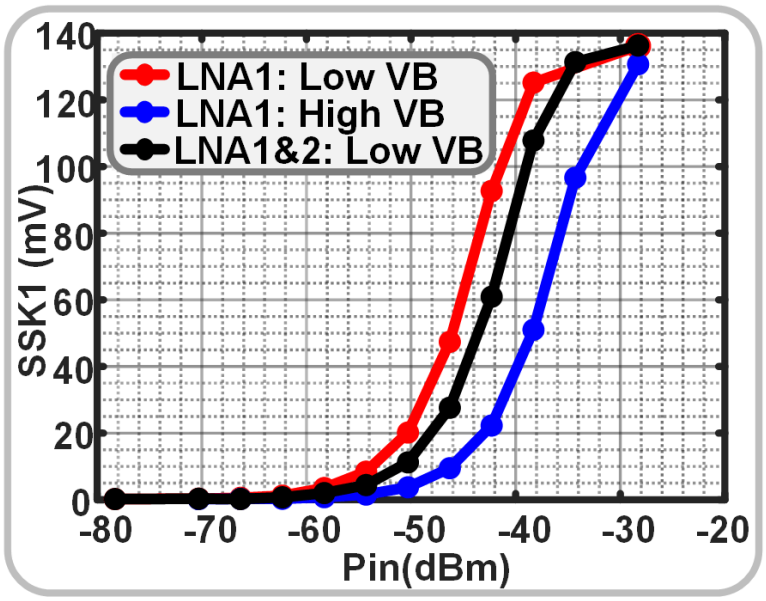

Figure 4.31: Measured sensitivity of Parallel-FSK-SSK RX with different LNA bias.

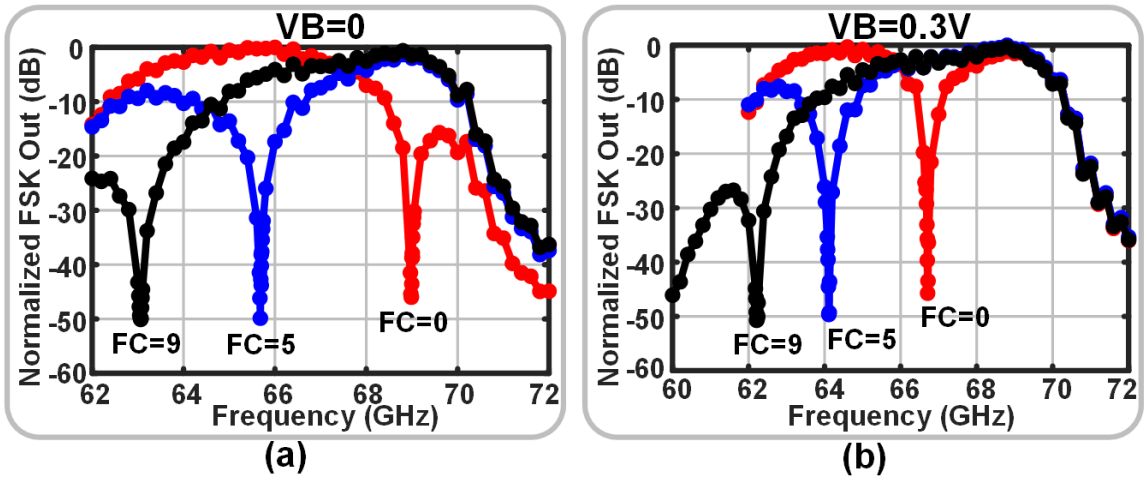

Figure 4.32: Measured FSK path gain across frequencies with (a) gm-cell disabled and (b) gm-cell enabled, demonstrating tunability and frequency discrimination in the FSK demodulator.

elements. The relative antenna pattern at $SSK1$ and $SSK2$ are shown at two frequencies used for the FSK in Fig. 4.35. As shown in Fig. 4.34, SSK transmission in a horn-antenna based setup is created by sending data from two different directions and

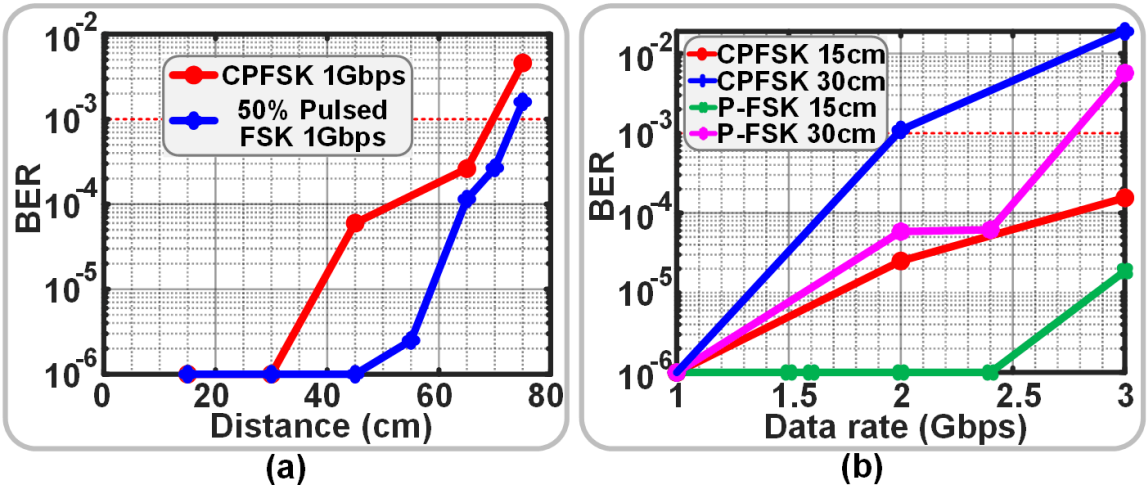

Figure 4.33: Measured BER for continuous-phase FSK (CPFSK) and 50% duty-cycle pulsed FSK (p-FSK) across (a) distances and (b) data rates.

SSK demodulation is performed by comparing relative value of $SSK1$ and $SSK2$. As shown in Fig. 4.36, BER of $< 10^{-3}$ at 1 Gb/s is achieved up to 100 cm (equivalent $P_{in,RX}$ is -40 dBm) with horn-antenna setup.

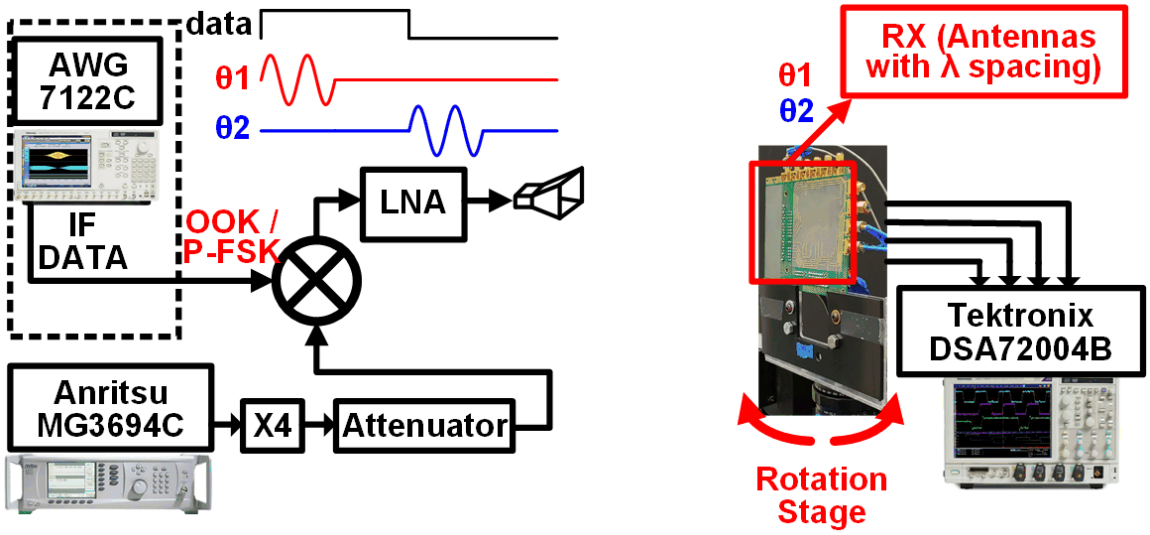

Figure 4.34: Measurement setup of SSK BER test using single horn antenna as TX.

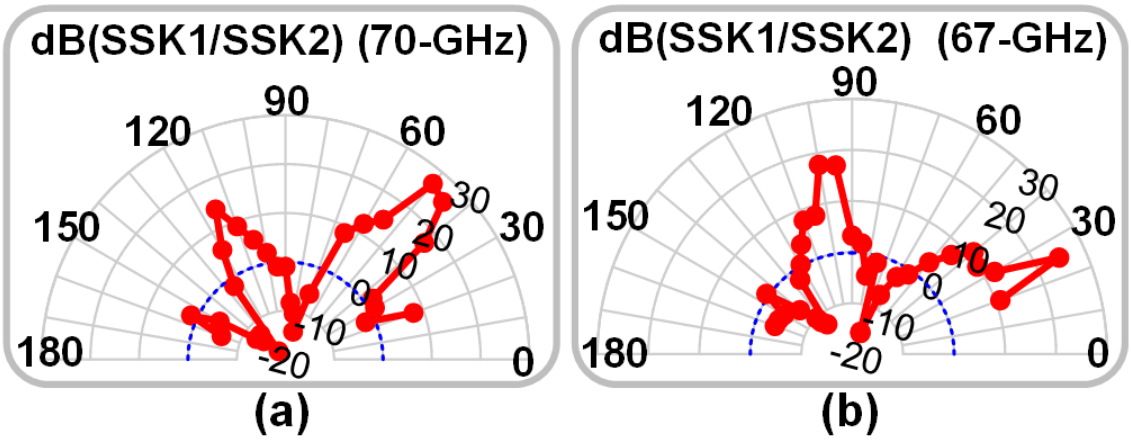

Figure 4.35: Measured SSK1/SSK2 across incident directions at (a) 70GHz and (b) 67GHz;

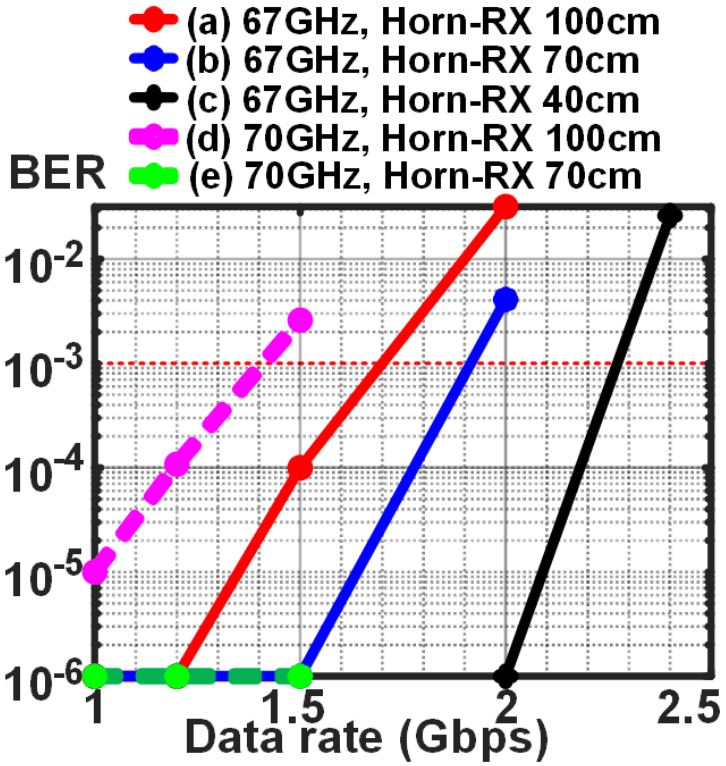

Figure 4.36: Measured SSK BER across data rates and distances.

4.4 TX-RX SSK Channel Analysis with Metal Reflectors

A better understanding of the SSK channel is essential to setup the measurements of TX-RX SSK link. The far field radiation pattern of a patch antenna with width W and length L on a substrate of thickness h can be described as

$$\mathrm{RP_{single}} = \cos\theta \cdot \mathrm{sinc}(\frac{k_o L}{2}\sin\theta)\mathrm{sinc}(\frac{k_o h}{2}\cos\theta) \tag{4.6}$$

The array factor of N-element antennas with spacing D is showed as

$$\mathrm{AF_N} = 1 + \sum_{i=2}^{N} \alpha_i \cos(\frac{2\pi}{\lambda} \cdot \frac{\Delta\tau_i}{T}\lambda + \frac{2\pi}{\lambda}(i-1)D\sin\theta) \tag{4.7}$$

where α_i is output power ratio of element$_i$ to element$_{i+1}$, $\Delta\tau_i$ is the delay between element$_i$ and element$_{i+1}$, D is the distance between each element, and T is the carrier period. Then the far field radiation pattern of two-element patch antennas can be described as

$$\begin{aligned}\mathrm{RP_{two}} = \cos\theta \cdot \mathrm{sinc}(\frac{k_o L}{2}\sin\theta)\mathrm{sinc}(\frac{k_o h}{2}\cos\theta) \\ \times(1 + \alpha\cos(2\pi\frac{\Delta\tau}{T} + \frac{2\pi}{\lambda}D\sin\theta)))\end{aligned} \tag{4.8}$$

We assumed there is no output power mismatch between two DCOs (thus α=1) and the two antennas are identical with the dimension of $L \approx 0.4\lambda$ and PCB substrate thickness $h \approx 0.125\lambda$. Fig. 4.37 shows the radiation pattern of two-element patch antenna array at various relative trigger delay $\Delta\tau_i$ for both D=$\lambda/2$ and D=λ.

In the RX side, SSK1, SSK2 detect envelope of the signal at the coupled and through port respectively. Define P1, P2, P3, P4 as the IN, THRU, CPL and ISO port of the on-chip quadrature coupler. The normalized gain from RX-ANT1 and RX-ANT2 to SSK1 and SSK2 can be expressed as

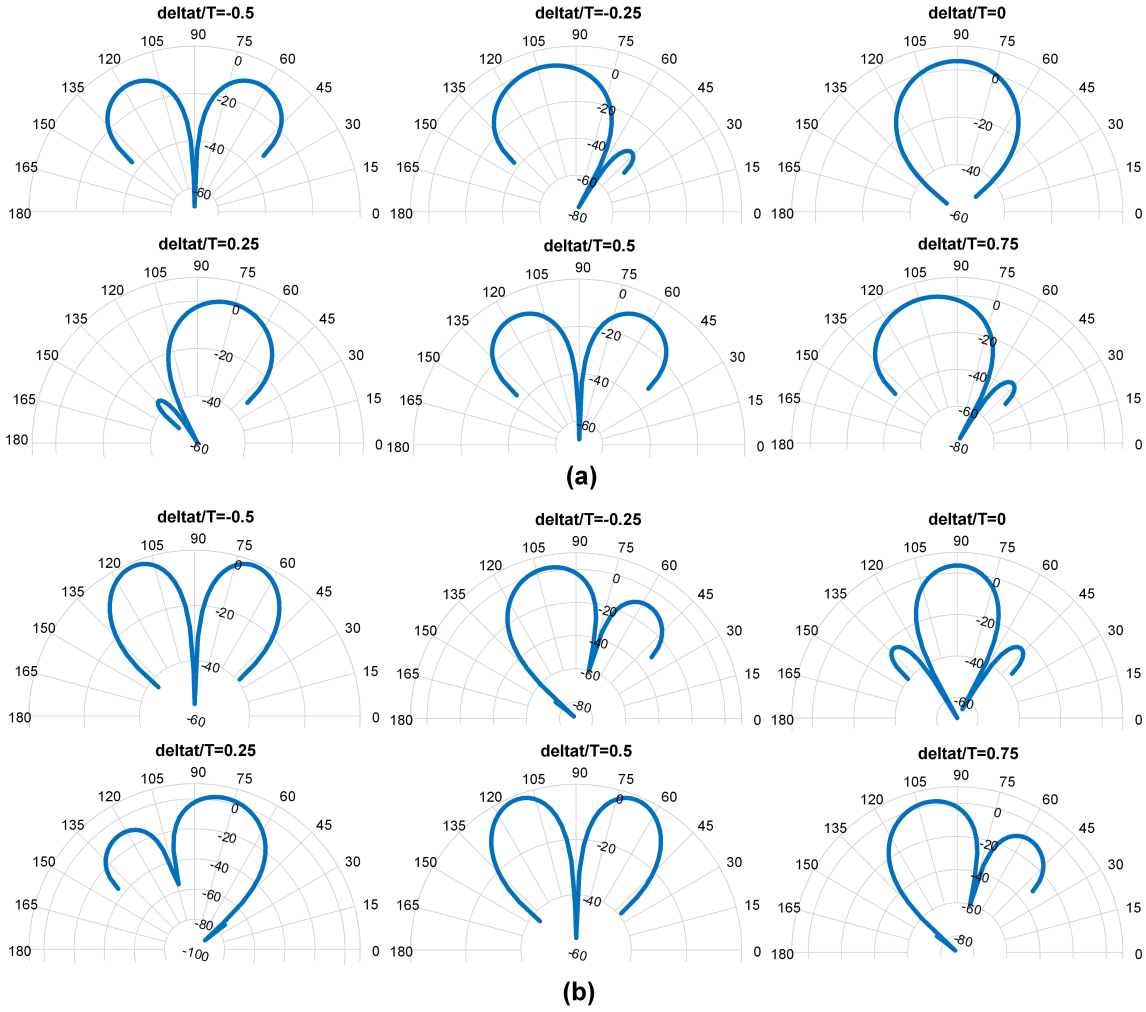

Figure 4.37: Radiation pattern of two-element SSK TX packaged with patch antenna array at various delay settings for (a) spacing D=$\lambda/2$ and (b) spacing D=λ.

$$A_{1,1} = (1-\epsilon_a)\cdot(-\frac{1}{\sqrt{2}}); \quad A_{1,2} = (1-\epsilon_a)\cdot(-\frac{j(1-\epsilon_b)}{\sqrt{2}}); \\ A_{2,1} = -\frac{j(1-\epsilon_c)}{\sqrt{2}}; \quad A_{2,2} = -\frac{(1-\epsilon_d)}{\sqrt{2}}; \tag{4.9}$$

where ϵ_a is the gain mismatch between LNA1 and LNA2, ϵ_b, ϵ_c, ϵ_d represents the

gain mismatches in the quadrature coupler. The SSK1 and SSK2 corresponding to signal with angle-of-incident (AoI) can be written as:

$$
\begin{aligned}
A_{\text{SSK1}} &\sim \text{RP}_{\text{single}} \cdot (A_{1,1} \text{e}^{-j\frac{2\pi}{\lambda}\text{Dsin}\theta} + A_{2,1}) \\
&= -\frac{\text{RP}_{\text{single}}}{\sqrt{2}}[(1-\epsilon_a)\text{e}^{-j\frac{2\pi}{\lambda}\text{Dsin}\theta} + (1-\epsilon_c)\text{e}^{j\frac{\pi}{2}}]; \\
A_{\text{SSK2}} &\sim \text{RP}_{\text{single}} \cdot (A_{1,2} \text{e}^{-j\frac{2\pi}{\lambda}\text{Dsin}\theta} + A_{2,2}) \\
&= -\frac{\text{RP}_{\text{single}}}{\sqrt{2}}[(1-\epsilon_a)(1-\epsilon_b)\text{e}^{j\frac{\pi}{2}}\text{e}^{-j\frac{2\pi}{\lambda}\text{Dsin}\theta} + (1-\epsilon_d)];
\end{aligned}
\tag{4.10}
$$

Fig. 4.38 shows the receiver outputs SSK1/SSK2 across angle-of-incidence for two-element SSK RX packaged with patch antenna for both D=$\lambda/2$ and D=λ. Fig. 4.39 shows the receiver outputs $P1/P2/P3/P4$ across angle-of-incidence for four-elements SSK RX packaged with patch antenna for D=$\lambda/2$.

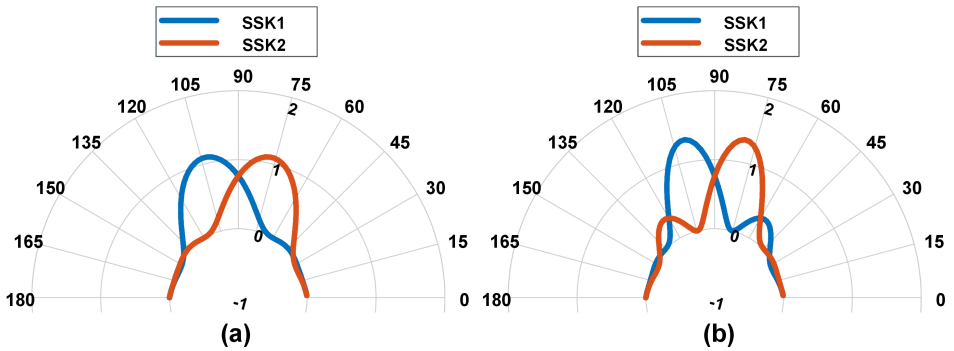

Figure 4.38: Receiver response across angle-of-incidence for two-element SSK RX packaged with patch antenna array for (a) spacing D=$\lambda/2$ and (b) spacing D=λ.

As shown in Fig. 4.40, by placing two metal reflectors at both sides of the wireless channel, the RX receives both the Line-of-Sight (LOS) and Non-Line-of-Sight (NLOS) (due to reflections) from the TX. Here we assume signals with more than one time reflections is negligible due to the extra path loss and extra reflections loss. Also once the TX/RX and metal reflectors is physically fixed, the channel between the TX and RX is a static channel. We can assume only three TX-to-RX path existing: one LOS path,

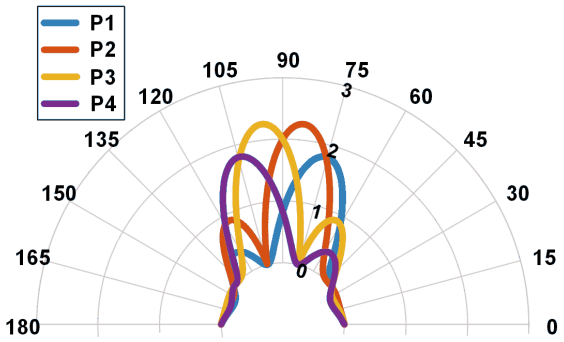

Figure 4.39: Receiver response across angle-of-incidence for four-element SSK RX packaged with patch antenna array for spacing D=$\lambda/2$.

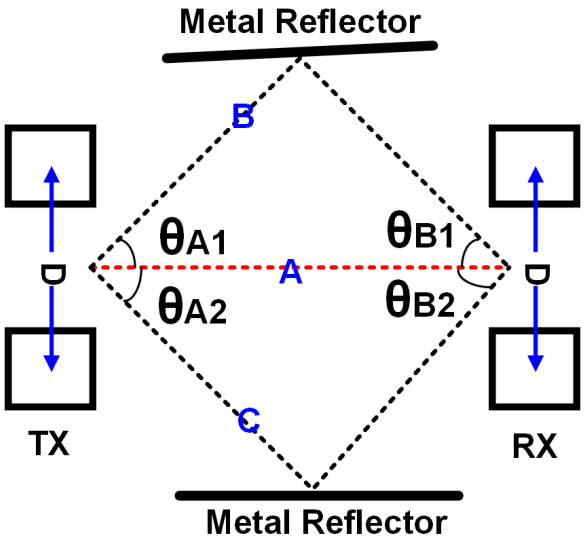

Figure 4.40: 2D model of SSK channel with side metal reflectors.

two NLOS path with reflection from either side reflector. The overall SSK1 and SSK2 can be described as:

$$
\begin{aligned}
\mathrm{V}_{\mathrm{SSK1,sum}} &= \mathrm{RP}_{\mathrm{two}}(\theta_{T0})A_{\mathrm{SSK1}}(\theta_{R0})\frac{\mathrm{e}^{-j\frac{2\pi}{\lambda}R_0}}{R_0} \\
&+\mathrm{RP}_{\mathrm{two}}(\theta_{T1})A_{\mathrm{SSK1}}(\theta_{R1})\frac{\mathrm{e}^{-j\frac{2\pi}{\lambda}R_1}}{R_1}\alpha_{\mathrm{loss}} \\
&+\mathrm{RP}_{\mathrm{two}}(\theta_{T2})A_{\mathrm{SSK1}}(\theta_{R2})\frac{\mathrm{e}^{-j\frac{2\pi}{\lambda}R_2}}{R_2}\alpha_{\mathrm{loss}} \\
\mathrm{V}_{\mathrm{SSK2,sum}} &= \mathrm{RP}_{\mathrm{two}}(\theta_{T0})A_{\mathrm{SSK2}}(\theta_{R0})\frac{\mathrm{e}^{-j\frac{2\pi}{\lambda}R_0}}{R_0} \\
&+\mathrm{RP}_{\mathrm{two}}(\theta_{T1})A_{\mathrm{SSK2}}(\theta_{R1})\frac{\mathrm{e}^{-j\frac{2\pi}{\lambda}R_1}}{R_1}\alpha_{\mathrm{loss}} \\
&+\mathrm{RP}_{\mathrm{two}}(\theta_{T2})A_{\mathrm{SSK2}}(\theta_{R2})\frac{\mathrm{e}^{-j\frac{2\pi}{\lambda}R_2}}{R_2}\alpha_{\mathrm{loss}}
\end{aligned}
\tag{4.11}
$$

With two TX antennas separated by λ and two RX antennas separated by λ, we can calculate the expected receiver outputs SSK1 and SSK2 with respect to the SSK directions (beamsteering angles). For the first scenario, we assume the metal reflectors are placed to make θ_{A1}=θ_{A2}=30 ∘ and θ_{B1}=θ_{B2}=30 ∘. Both SSK1 and SSK2 can be separate into three components SSK1$_{A,B,C}$ and SSK2$_{A,B,C}$, representing signal travel from LOS-path(A), NLOS-path(B) and NLOS-path(C) (Fig. 4.40). The SSK1 and SSK2 shows same pattern across SSK directions in this scenario (Fig. 4.41).

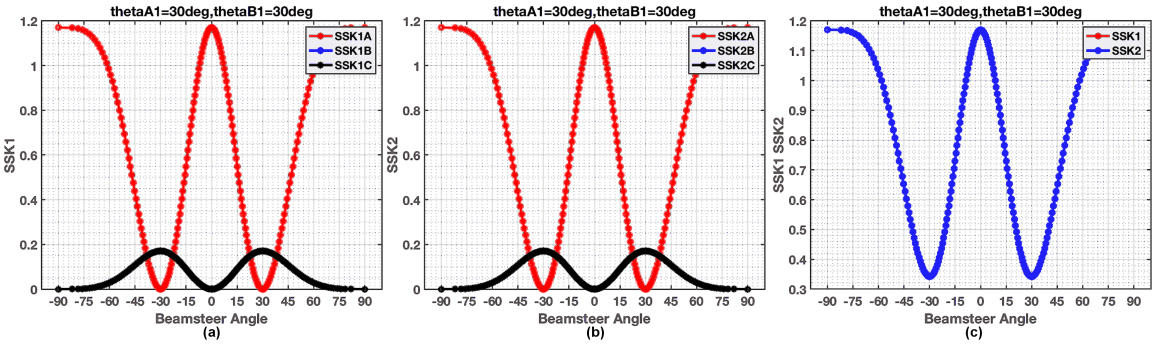

Figure 4.41: SSK pattern across beamsteering angles when the metal reflectors are placed such that θ_{A1}=30° and θ_{B1}=30°.

For the second scenario, we assume the metal reflectors are placed to make θ_{A1}=θ_{A2}=30 ◦ and θ_{B1}=θ_{B2}=15 ◦. The components SSK1B and SSK2C, SSK1C and SSK2B has the same pattern for SSK1 and SSK2. Thus SSK1 and SSK2 also shows same pattern across SSK directions in this scenario (Fig. 4.42).

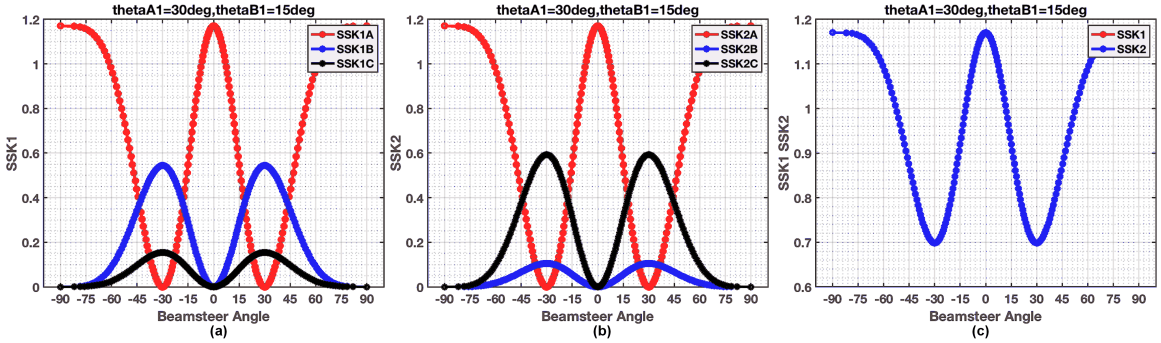

Figure 4.42: SSK pattern across beamsteering angles when the metal reflectors are placed such that θ_{A1}=30° and θ_{B1}=15°.

For the second scenario, we assume the metal reflectors are placed to make θ_{A1}=θ_{A2}=15 ◦ and θ_{B1}=θ_{B2}=15 ◦. The SSK1 and SSK2 has different pattern across SSK directions in this scenario (Fig. 4.43). Also the NLOS path is delayed compared to the LOS path and the phase differences can be anything depends on the channel geometry. Fig. 4.43(c) shows the SSK1 and SSK2 pattern when the LOS signal and echoes are in-phase, while Fig. 4.43(d) shows the SSK1 and SSK2 pattern when the LOS signal and echoes have 180° phase difference. The actual SSK1 and SSK2 patterns are more complex and calibration is needed if any spacial parameters is changed for such slowly-varying channel to determine the SSK1 and SSK2 patterns across SSK directions/beamsteering angles.

4.5 TX-RX SSK Measurements with Metal Reflectors

An SSK-FSK link measurement with a CMOS SSK-TX is performed using the setup shown in Fig. 4.44. Metal reflectors are included in the setup to emulate a static reflective channel with multipath. SSK-FSK measurements demonstrating $< 10^{-4}$ errors with effective 2 Gb/s data rates (1 Gb/s FSK and 1 Gb/s SSK) using integrated 68-GHz FSK-SSK CMOS TX and the proposed FSK-SSK RX, demonstrating the first mm-wave

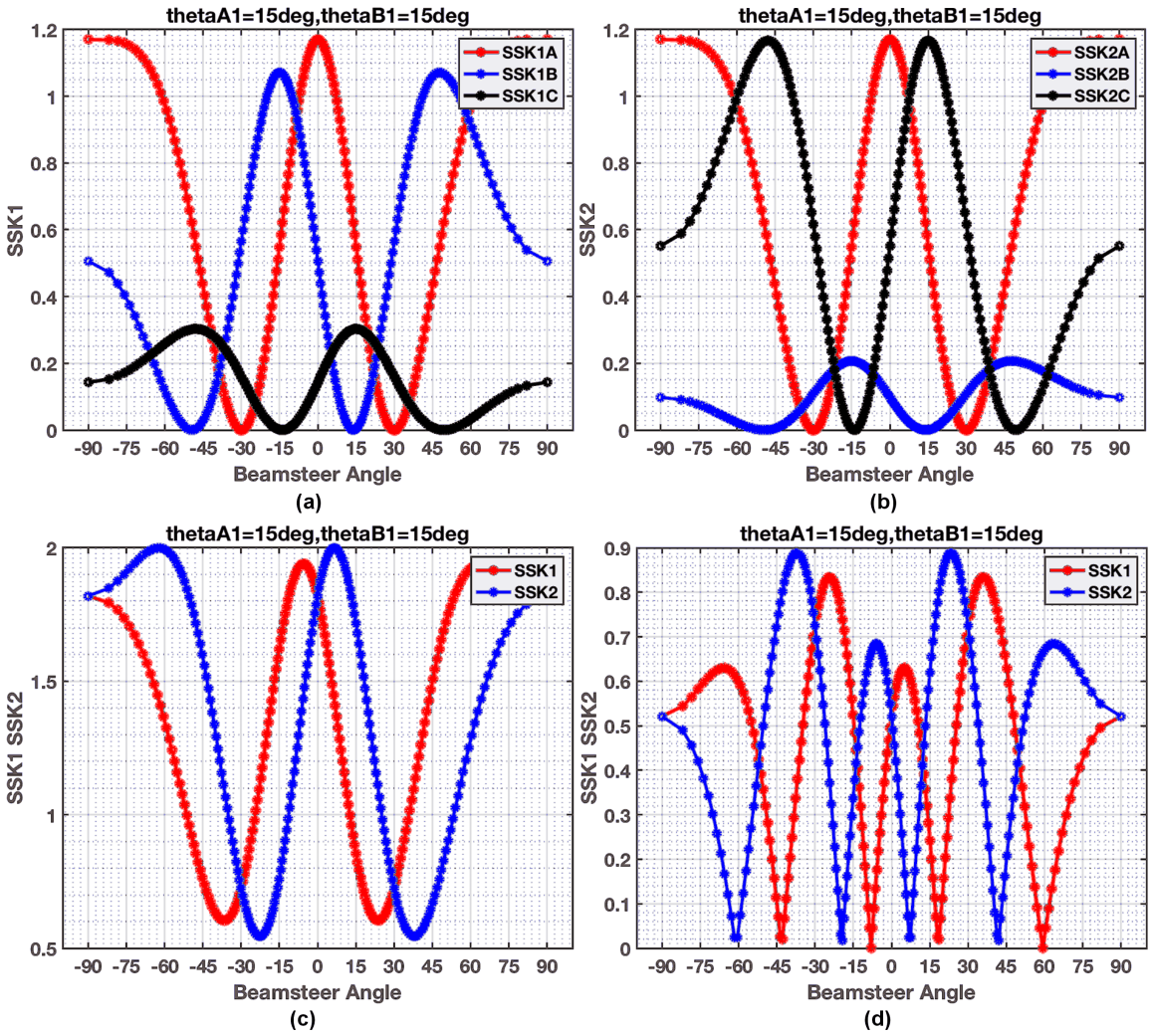

Figure 4.43: SSK pattern across beamsteering angles when the metal reflectors are placed such that θ_{A1}=15° and θ_{B1}=15°.

CMOS SSK link. The RX consumes ∼14.8mW/element leading to overall ∼ 30mW power consumption.

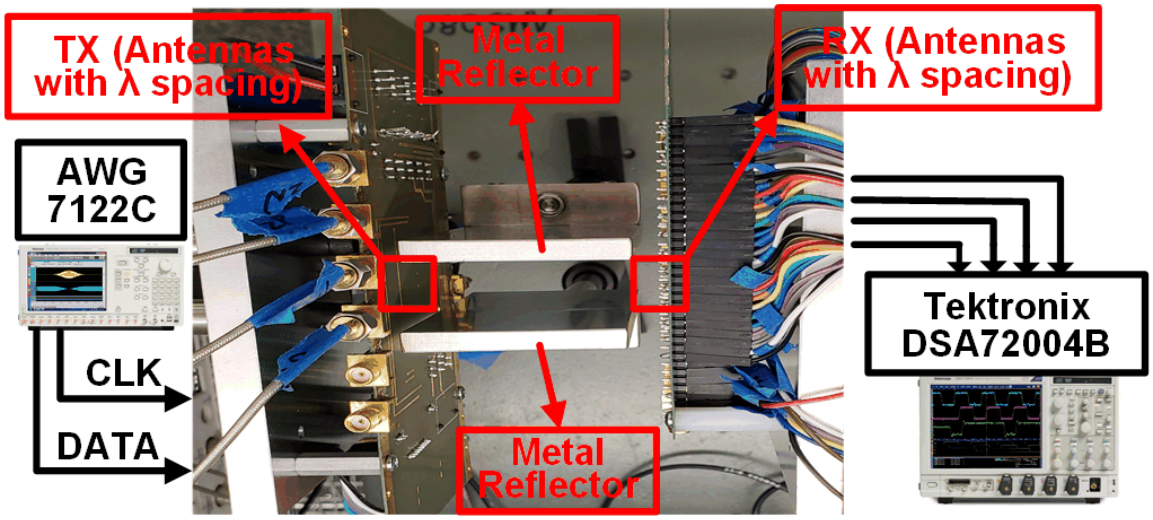

Figure 4.44: Measurement setup for TX-RX link using metal reflectors to provide signal paths with various spatial properties, as well as to mimic enclosed platforms.

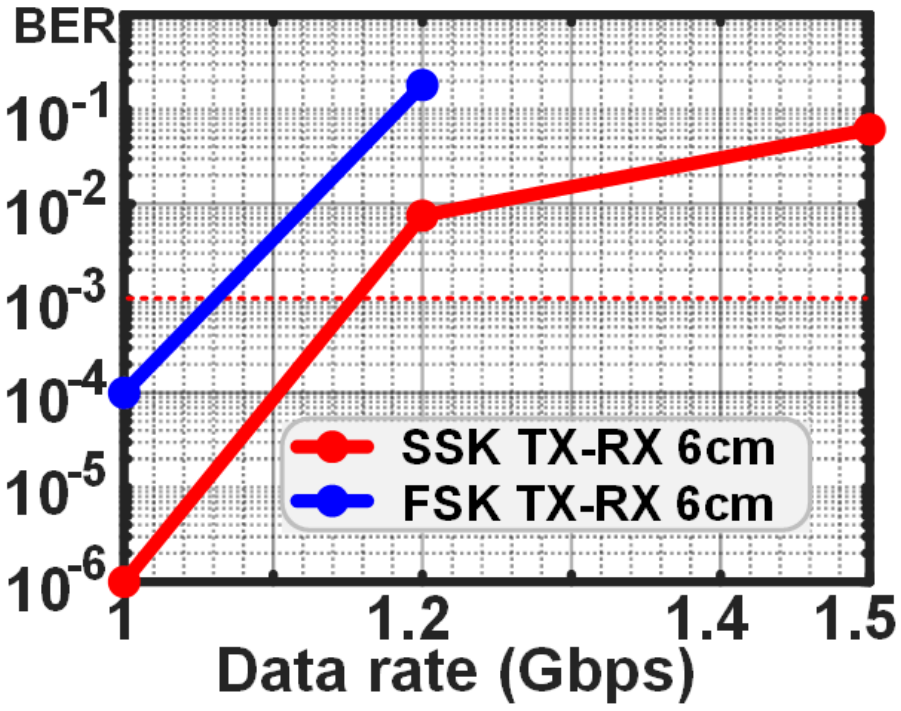

Figure 4.45: Measured BER for 68 GHz CMOS TX-RX FSK/SSK link.

	This Work	Byeon, TMTT13	Lee, MWCL16	Zhu, TMTT14	Wang, VLSI 10
Technology	65nm	90nm	65nm	90nm	90nm
Freq	68GHz	60GHz	84GHz	45GHz	60GHz
Modulation	Spatial/FSK	OOK	OOK	OOK	FSK
No. of Elements	2	1	1	1	1
Antenna	Aperture -Coupled Patch (4.6dBi)	Yagi-Uda (6.6dBi)	Probe Test Only	SIW (8.7dBi)	Folded dipole (5dBi)
RX Power (mW)	15/element 30 total	36	46	54	150+ 70(PLL)
TX Power (mW)	11/element 22 total	31	None	62	280
Data Rate (Gb/s)	2@1e-4	3@1e-6	10@1e-6	4@1e-6	2@1e-6
Sensitivity (dBm)	(-38, -46*)	(-45)	(-45)	(-46)	(-57)
Energy/bit (pJ/bit)	26	22.3	NA	29	250
Path loss	(45dB)	(60dB)		(62dB)	(62dB)

*** Sensitivity at peak LNA gain**

Figure 4.46: Comparison to state of the art low-power mm-wave RX.

4.6 Conclusion to FSK-SSK RX

Space shift keying represents a promising technique to increase energy efficiency in relatively slow-varying channels. A low-power mm-wave two-element RX is implemented in 65 nm CMOS targeting FSK-SSK modulated short-range links at mm-wave. An end-to-end 68 GHz FSK-SSK link operating at 2 Gb/s over 6 cm with integrated CMOS RX and TX demonstrates the first SSK-FSK link and the feasibility of using SSK in addition to other energy-efficient modulation schemes to improve overall link energy efficiency.

Chapter 5: An Integrated 7-Gb/s 60-GHz Communication Link Over Single Conductor Wire using Sommerfeld Wave Propagation in 65-nm CMOS

5.1 Introduction to Guided mm-Wave Electrical Links

The need for high data rate, high density, and physically reconfigurable I/O links has led to wirelessly-coupled inter-chip links established through proximity coupling [50], guided-waves in low-cost waveguides [22, 25, 38, 51], and wireless links [17]. Wireless / guided-wave links are particularly attractive in CMOS technologies capable of high-speed digital processing to enable full integration. However, such links suffer from two critical challenges: (i) signal coupling between the TX/RX on the IC and the channel, and, (ii) signal propagation through the channel (waveguide/air). Weak signal coupling restricts fully-integrated capacitively-coupled proximity-coupling links to $<$ 2-mm range [50]. Although, hollow plastic-tube based links can achieve longer range, they require bond-wire / PCB antennas and have asymmetry between TX and RX antennas [22]. Furthermore, data rates over such hollow waveguides are ultimately limited by waveguide loss at high frequencies (2.5-dB/m@120-GHz), dispersion, and higher order modes [6]. Wireless links at sub-mmwave are conducive to antenna integration but are limited severely by free-space path loss.

Fig. 5.1 shows the energy efficiency of conventional electrical links and optical links across channel distance. The high channel loss for conventional electrical links at high frequencies means that the equalization required to achieve high data rates is challenging to overcome to achieve with good link energy efficiency. This can be seen by the higher pJ/bit required for longer range conventional electrical links particularly as links approach tens of centimeters to meters. One solution is to use optical interconnect; However, such links suffer from poor energy efficiency of lasers and even in the case of integrated photonics, the need for precision physical packaging with um-scale resolu-

tions. The cost and complexity overhead of using optical links has meant the crossover between conventional electrical and optical links is in the range of meters. Guided mm-wave electrical links are potential solutions by targeting energy efficiency in the tens of cm to few meters range to bridge this gap between conventional electrical and optical links. Previous offers of guided mm-wave electrical links have been focused on hollow and solid polymer waveguides that are of the order of mm in dimensions and have low loss at mm-wave and THz frequencies. Fig. 5.2 shows the loss and group delay in such solid and hollow dielectric waveguides. The dispersion in such dielectric waveguides varies almost linearly with frequency for a given length and is increasing with channel length. This puts a limit on the maximum data rates supported by the dielectric waveguides for a given channel length and a given center frequency.

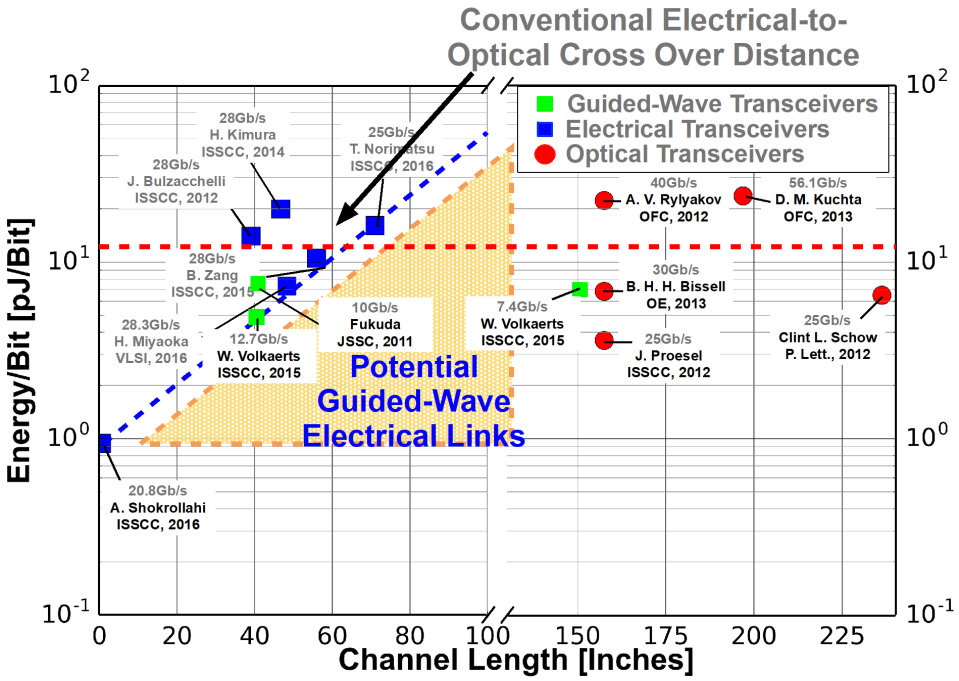

Figure 5.1: Energy efficiency of electrical and optical links across channel distance.

Radial-mode Sommerfeld-wave propagation over a single-wire has long been known to have low loss ($<$ 1 dB/m@100 GHz) and almost no dispersion up to hundreds of GHz [7,52]. However, exciting the radial wave in a single conductor wire (SCW) is chal-

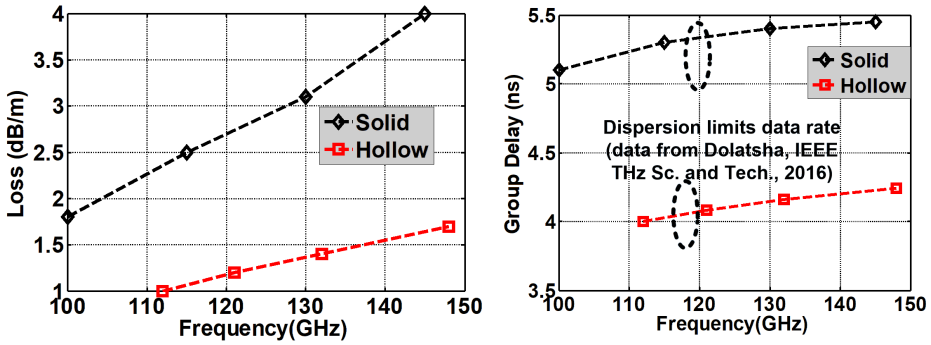

Figure 5.2: Loss and group delay in solid and hollow dielectric waveguides (data from [6]).

lenging with typical linear/circular polarized antennas and has been accomplished using picosecond lasers exciting currents on a concentric two-electrode antenna fabricated on photo-conductive material [7]. In this work, we present an approach for mm-wave excitation of the Sommerfeld-wave mode on a SCW using a radial on-chip antenna, demonstrating a fully-integrated end-to-end 7 Gb/s transceiver system over 60-GHz carrier (including serializers, mm-wave OOK modulators, on-chip antennas, demodulators and deserializers) across 20-cm of bare copper wire (diameter = 0.4 mm) with no off-chip components. This work presents not only the first fully-integrated system, but is also the first demonstration of a multi-Gb/s links over SCW using Sommerfeld waves [53].

5.2 Fully-Integrated Communication Link Over Single Conductor Wire

5.2.1 System Overview of Guided Link on SCW

Fig. 5.3 outlines the link concept. A high-speed multiplexer serializes incoming data and drives an on-chip mm-wave TX that generates an OOK-modulated 60-GHz signal. The TX output is coupled to the Sommerfeld radially-polarized propagation mode in a single conductor wire (SCW) using an on-chip antenna. The weakly-guided Sommerfeld wave occurs due to the finite conductivity of the bare-copper SCW and propagates along the SCW as a TM wave. The electric field is largely radial as shown in

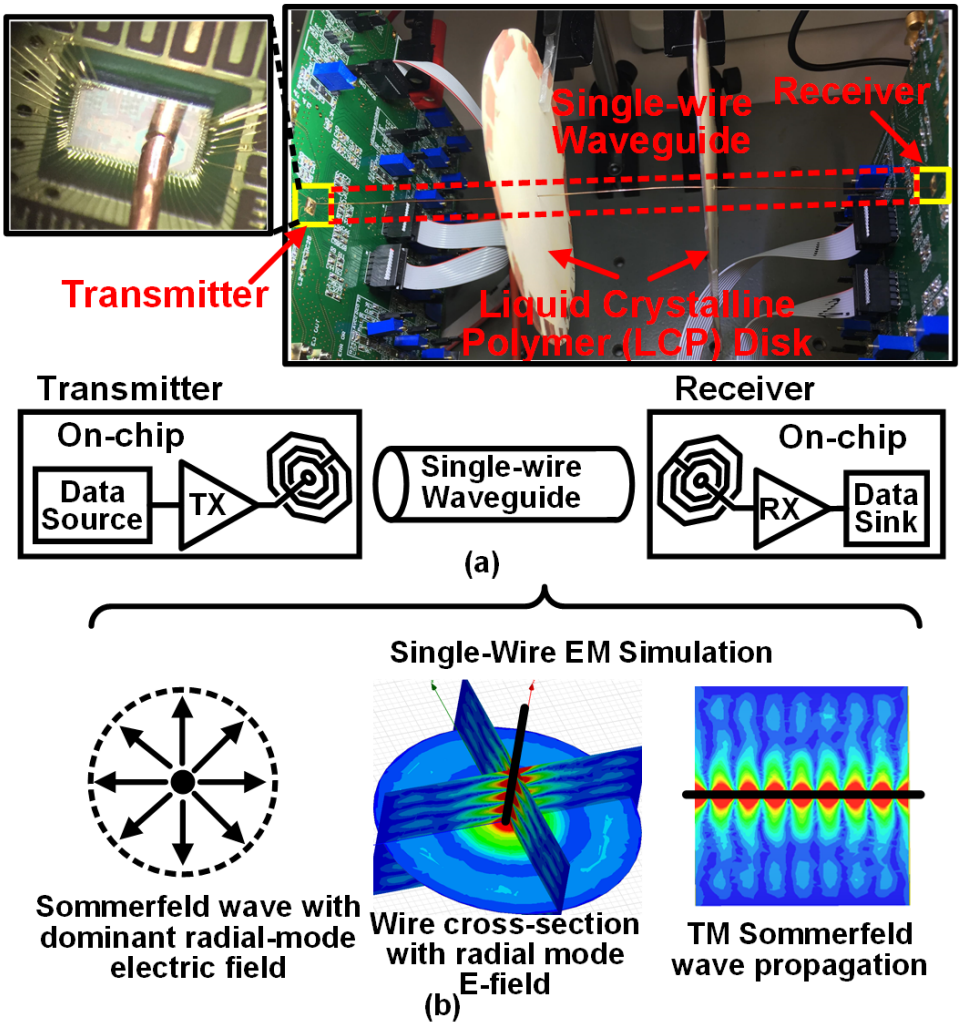

Figure 5.3: (a) System overview of communication link with a modulated 60-GHz carrier using low-loss and flat dispersion Sommerfeld-wave propagation in a single conductor wire (SCW) (bare copper wire, 400 μm diameter), (b) EM simulations of dominant radial-mode E-field and TM propagation in SCW.

Fig. 5.3 but has a longitudinal component along the wire. The SCW is supported mechanically using $\sim$100 μm-width Liquid Crystal Polymer (LCP) disks (ϵ_R= 2.9, tan δ = 0.0025@10 GHz). The supporting structure ensures radial symmetry around the SCW up to $\sim 5\lambda$ (λ = 5 mm @ 60 GHz) to maintain radial-mode propagation. On the RX, a similar antenna couples the 60-GHz Sommerfeld wave from the SCW into the IC where

an OOK demodulator drives on-chip samplers and deserializers. The wide bandwidth of the SCW propagation channel implies that simple modulation schemes such as OOK are adequate with wideband mm-wave circuits, and efficient coupling into SCW ensures that the link does not require equalization.

5.2.2 Loss and Group Delay of Sommerfeld Wave

Fig. 5.4 shows the attenuation and effective permittivity of the Sommerfeld mode on SCW (data from [7]). The Sommerfeld-wave mode is low-loss and has flat dispersion across frequency and hence the coupling loss from IC to the Sommerfeld-Wave mode dominates link performance. Given the fact that the Sommerfeld wave is weakly guided by the SCW, a significant portion of the electric field exists in a region outside the wire. Shown in Fig. 5.5 is the simulated electrical field amplitude as a function of radial distance from the SCW, indicating that the electrical field magnitude drops by about 20dB at distances exceeding around 4mm from the SCW. Fig. 5.6 shows the simulated coupling between two SCWs that are ∼8mm apart is below -10dB.

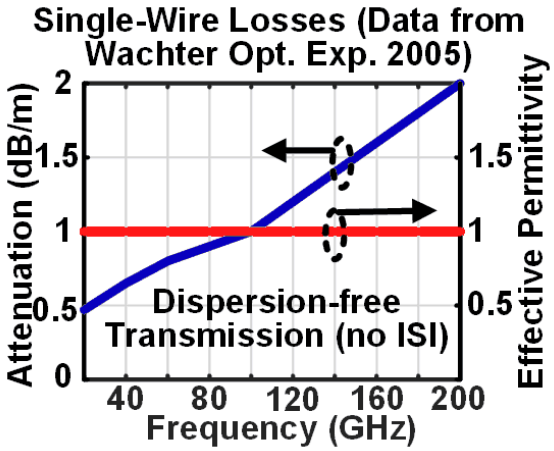

Figure 5.4: The loss and dispersion of the Sommerfeld mode on single conductor wire (data from [7]).

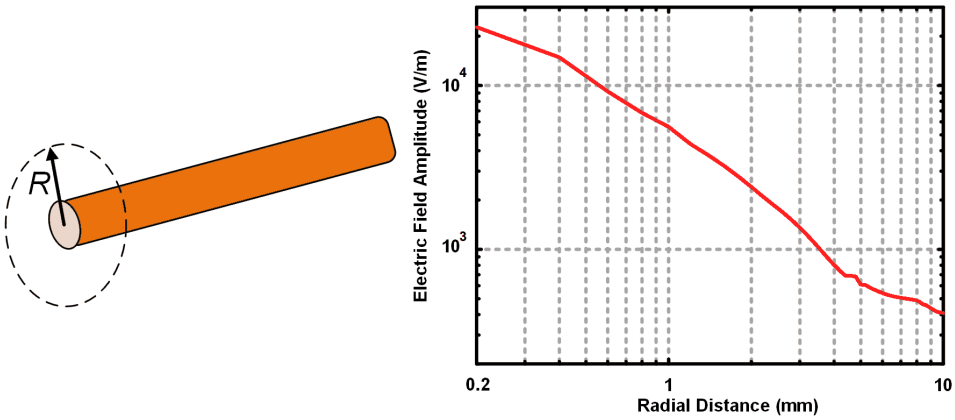

Figure 5.5: Simulated electrical field amplitude as a function of distance from the single conductor wire.

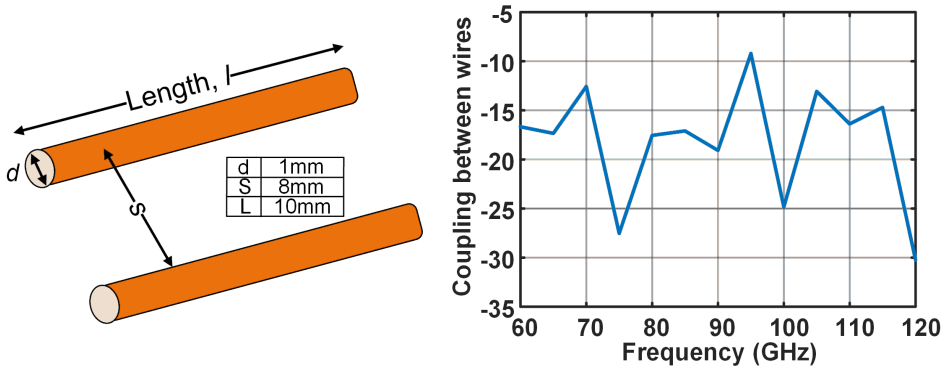

Figure 5.6: Simulated coupling between two single conductor wires that are around 8mm apart.

5.2.3 Radial Mode Antenna Design

Fig. 5.7 shows the proposed on-chip radial mode antenna which is discussed here in the context of the TX, where a radial electric field is desirable to couple effectively to the radial propagation mode on the SCW. An on-chip co-planar waveguide feeds the antenna, which consists of the concentric rings R_{P1}, R_{P2}, R_{P3} (in red) connected to the signal, and R_{N1}, R_{N2} and R_{N3} (in blue) connected to the RF ground. Since the signal is connected to R_{P1} and the ground is connected to R_{N1} (see Fig. 5.7) - electric dipoles are created between $R_{P,k}$ and $R_{N,k}$ as well as between $R_{P,k}$ and $R_{N,k+1}$. However, the

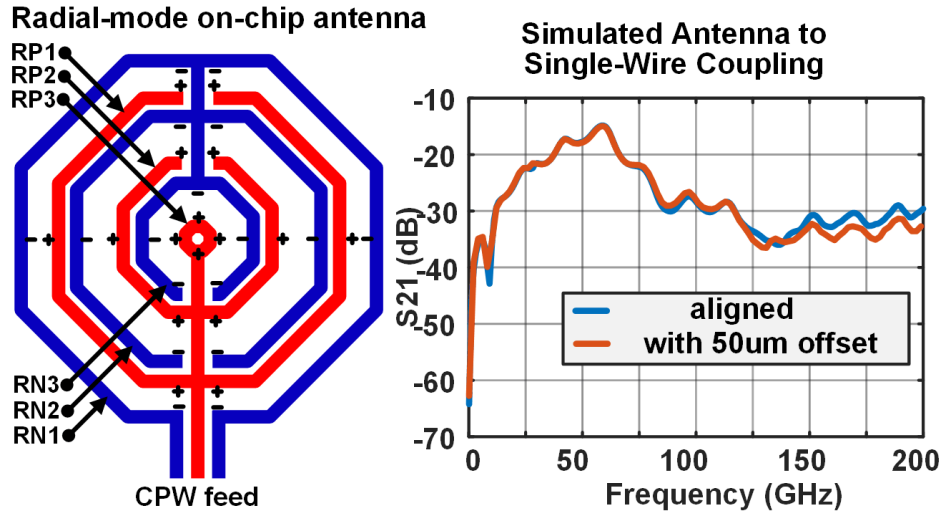

Figure 5.7: (a) Radial antenna approach for coupling mm-wave modulated signal on the IC to the radial Sommerfeld-wave mode on the SCW, (b) Simulated coupling loss from the radial antenna to the SCW.

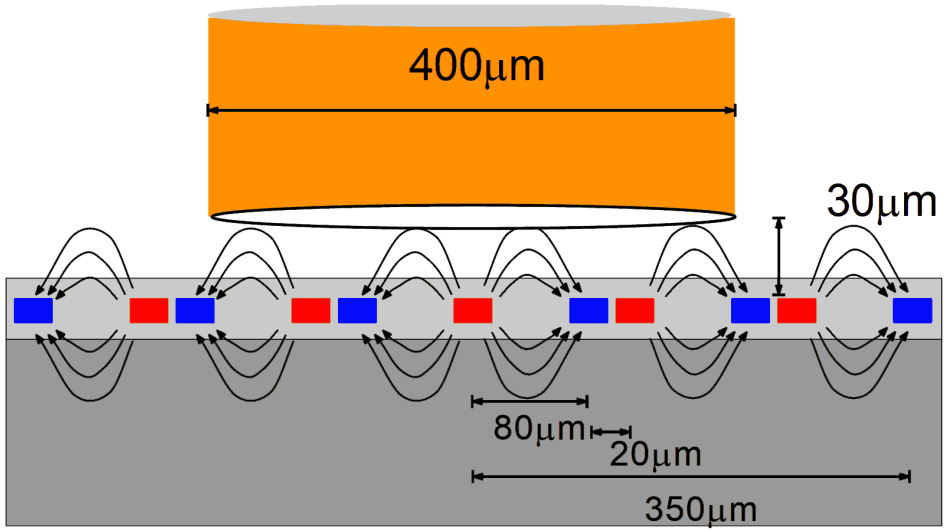

Figure 5.8: Side-view of the radial antenna and the SCW showing the coupling mechanism of electrical fields from the radial antenna to the SCW.

dipoles between R_P and R_N rings that are placed close together do not couple to the wire whereas dipoles created between rings such as $R_{P,k}$ and $R_{N,k}$ result in signal coupling to the wire. Since these dipoles are created all along the antenna, a radial electric field is

created that couples to the radial mode when the single-wire conductor is placed close to the antenna. Additional rings enhance coupling, however, EM simulations suggest little benefit beyond the three ring structure. Fig. 5.8 shows the side-view of electrical fields coupling from the on-chip radial antenna to the SCW. The proposed antenna can tolerate off-center SCW placement to within ± 100 μm. Passivation layer on top of the IC ensures no electrical contact between the wire and the antenna. Notably, the proposed antenna requires the absence of a ground plane underneath - to prevent electrical field lines from the antenna rings to the ground. The IC was packaged using chip-on-board and the ground plane of the PCB is 450 μm away from the part of the IC with the antenna. Fig. 5.7 shows s-parameters based on EM simulations, demonstrating $\sim$-15dB coupling between the IC and the antenna. Coupling loss is dominated by losses in the silicon substrate (10 Ω-cm in this implementation) and hence thinning the substrate and/or using high-resistivity substrate technologies will lead to higher efficiency. The single wire itself has $<$ 1-dB/m loss implying that all signal loss occurs when coupling to/from the IC. The antenna presents an impedance of 25 Ω at 60 GHz.

5.2.4 Fully-Integrated 60GHz TX/RX Design

The CMOS TX/RX implementation is shown in Fig. 5.9. The mm-wave TX consists of a low-power digitally-controlled oscillator (DCO) (tuning range: 57 GHz to 62 GHz) that drives a 60-GHz buffer. OOK modulation is accomplished by a mm-wave switch driven by buffered data. The DCO and buffer are differential and a transformer at the output of the switch drives the single-ended antenna. The transformer is also sized to resonate with the switch to provide a 25-Ω match at 60 GHz and switch transistors are sized to balance the trade-off between power required for data buffers to drive the switch and mm-wave loss. In simulation, the 60-GHz OOK modulator delivers a 0-dBm 60-GHz signal at the radial mode antenna. Fig. 5.10 shows the simulated TX output delivered to the 25Ω SCW coupling antenna. The OOK modulator generates OOK signal with 18dB on-off-ratio.

The 60-GHz LNA uses a transformer-based neutralization scheme that provides higher gain than common-source stages for same power consumption. The 6-stage

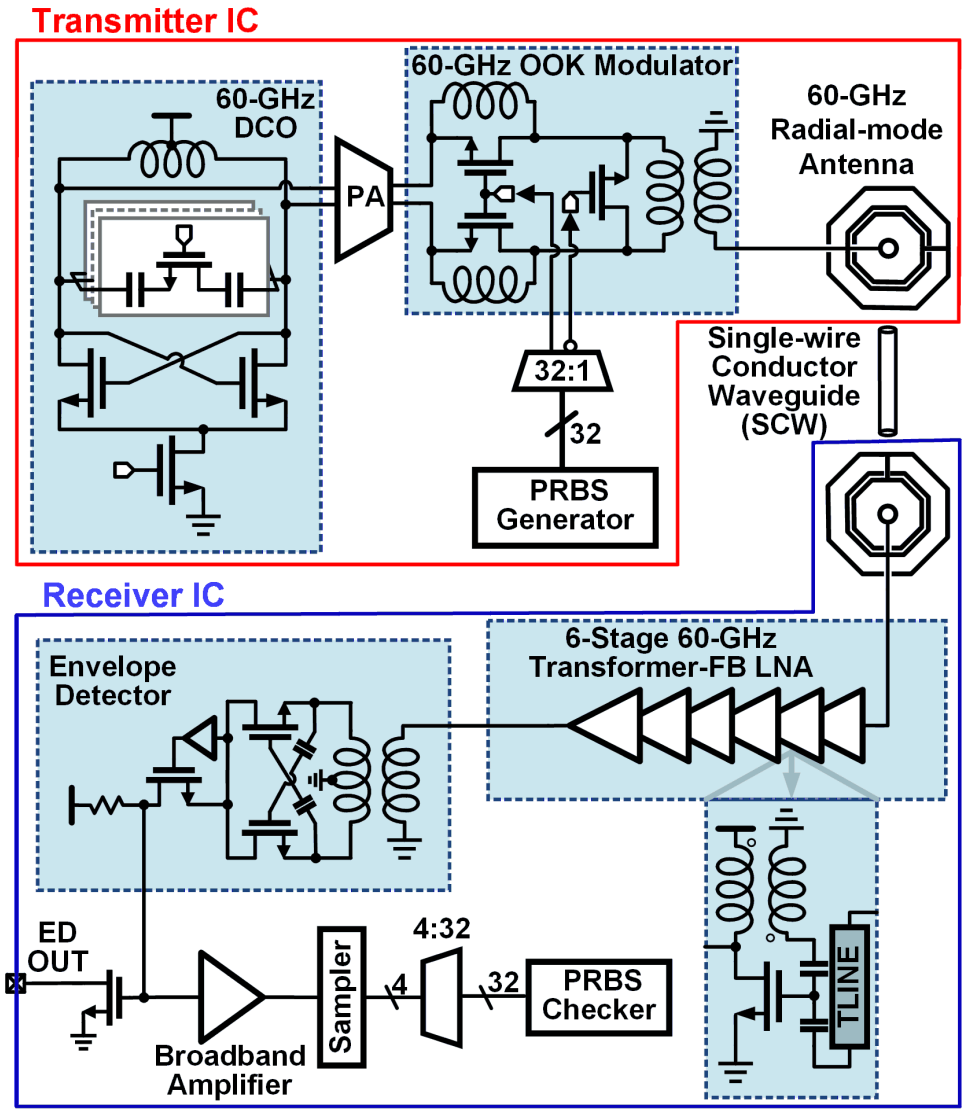

Figure 5.9: Block diagram of the proposed 60-GHz 7 Gb/s transceiver IC with OOK modulator / demodulator and radial-mode antenna.

LNA provides 24-dB gain and 6.2-dB noise figure (NF) in simulation while consuming ∼21 mW and is also matched to 25-Ω antenna input. Fig. 5.11 shows the simulated S21 of the 60GHz LNA. The LNA output is provided to a 60-GHz envelope detector (ED) for OOK signal demodulation, amplification and sampling. In addition, the ED

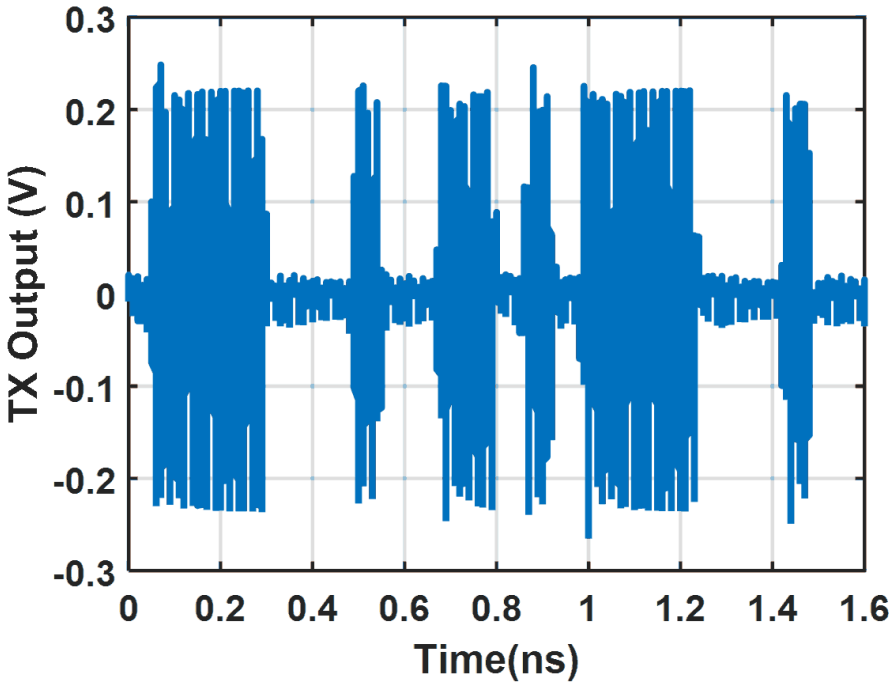

Figure 5.10: Simulated TX output on the 25Ω SCW coupling antenna.

output drives an open-drain buffer for direct measurement.

5.3 Measured Performance of Fully-Integrated Guided Link over SCW

The die micrograph of the 65-nm CMOS implementation of the concept and block level power consumption are shown in Fig. 5.12. The test setup for the SCW link measurements closely follows Fig. 5.3. Bare Cu wire with 400 μm diameter (26AWG) is used as the SCW and is placed in proximity to the antenna on the TX and RX. The 20-cm long wire has an intrinsic bend in the current setup with a radius of $\sim$28 cm. Fig. 5.13 shows the measured pulse response of the entire transceiver including the wire for 10-cm and 20-cm wire lengths and 5 Gb/s and 6 Gb/s pulse widths. For this measurement, 166.67-ps and 200-ps pulses were up-converted in the modulator to 60-GHz carrier, amplified by LNAs and finally received by the envelope detector output. Despite increasing the

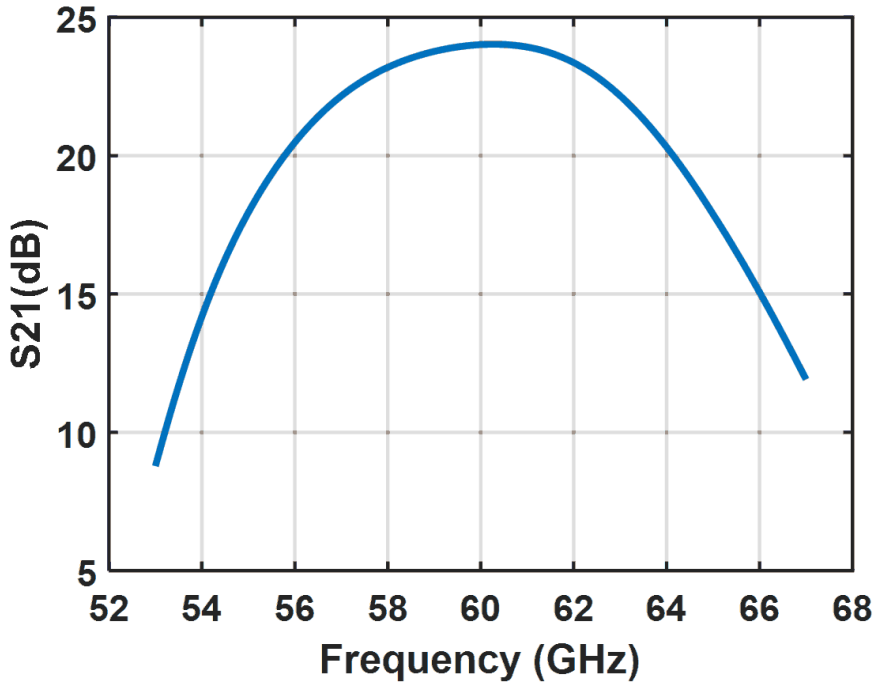

Figure 5.11: Simulated S21 of the 60GHz transformer-feedback LNA used in the OOK demodulator.

wire length by 2x, the measured pulse response shows no change in the pre- and post-cursor ISI. This measurement demonstrates the low loss and wideband nature of the proposed communication channel and the TX-RX 60-GHz front end.

Fig. 5.14 shows the measured buffered ED output (eye diagrams) for 5 Gb/s data rates with 10cm-channel and 20cm-channel. Fig. 5.15 shows the measured buffered ED output for 6 Gb/s and 7 Gb/s data rates for 20cm-channel. Even though the open-drain buffered output has lower bandwidth than the internal ED output node, the eye opening can still be seen at 7 Gb/s for the buffered ED output. Fig. 5.16 shows the measured bathtub plot of the 6Gb/s and 7Gb/s sampled data for 20cm-channel. The proposed transceiver achieves 7 Gb/s data rate for BER $< 10^{-5}$ and 6 Gb/s for BER $< 10^{-12}$. The measured bathtub curves at 6 Gb/s and 7 Gb/s are shown in Fig. 5.16. At 6 Gb/s, the received eye opening is 36 ps. The proposed transceiver is compared with the state-of-the-art guided-wave/wireless link approaches in Table 5.1. Notably, the SCW link

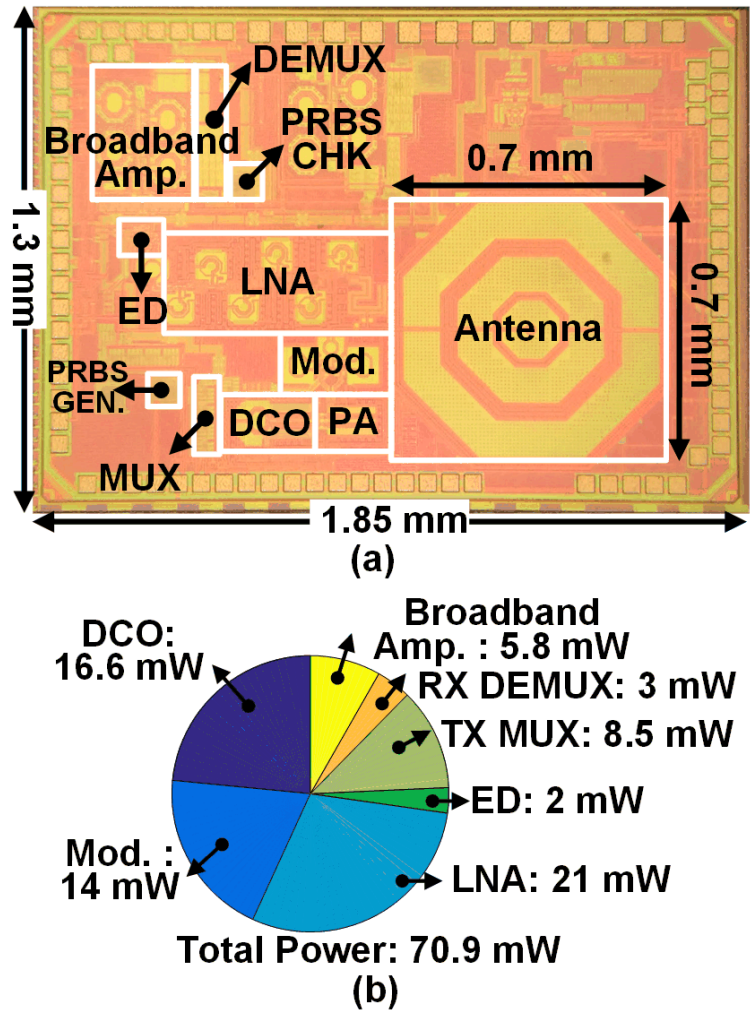

Figure 5.12: (a) Die photograph of the proposed transceiver in 65-nm CMOS; (b) Summary of transceiver power consumption.

in this work is fully integrated and does not require any off-chip/bondwire components while achieving comparable energy efficiency even with 65-nm CMOS.

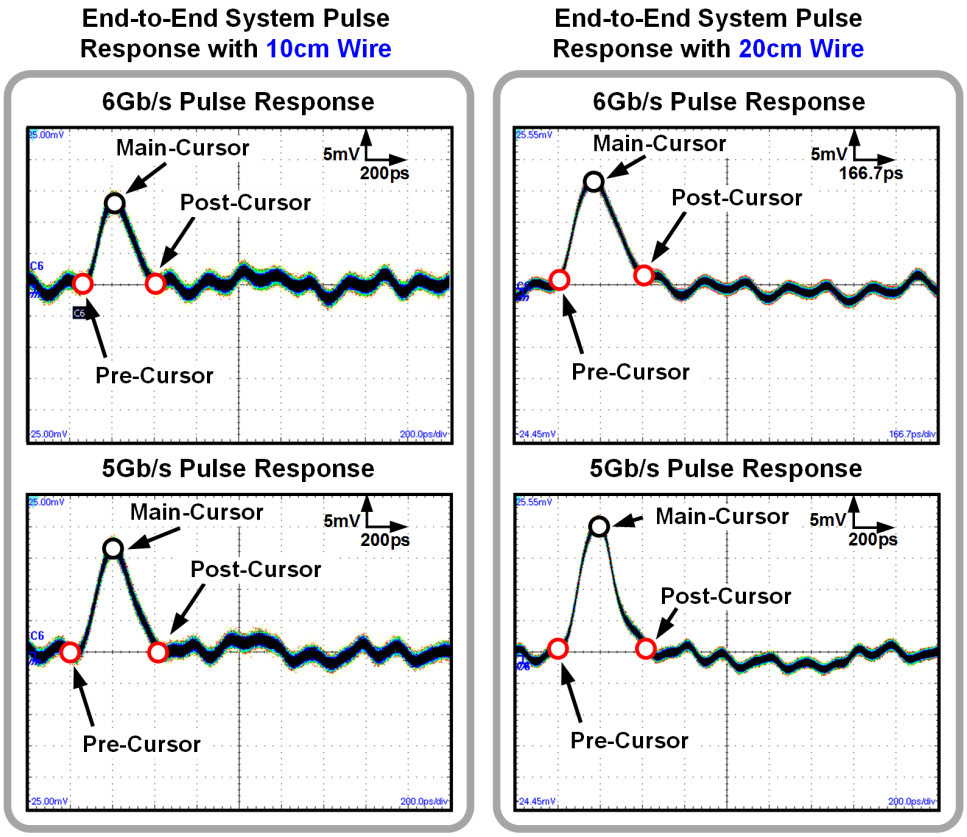

Figure 5.13: Measured end-to-end system pulse response for 10-cm wire and 20-cm wire lengths demonstrating a low-loss and dispersion free channel.

5.4 Conclusion to Fully-Integrated Guided Link over SCW

The chapter presents the first demonstration of a mm-wave data link using Sommerfeld-wave propagation on a single conductor wire. A fully-integrated end-to-end prototype is presented to demonstrate the feasibility of energy-efficient high data rate links over the low-loss and low-dispersion waveguide. The 65-nm CMOS prototype achieves 7 Gb/s data rate over 20-cm channel length with energy efficiency of $\sim$10 pJ/bit. Future work includes achieving higher data rates using the SCW by increasing carrier frequency and investigating multi-lane mm-wave data links using parallel SCW.

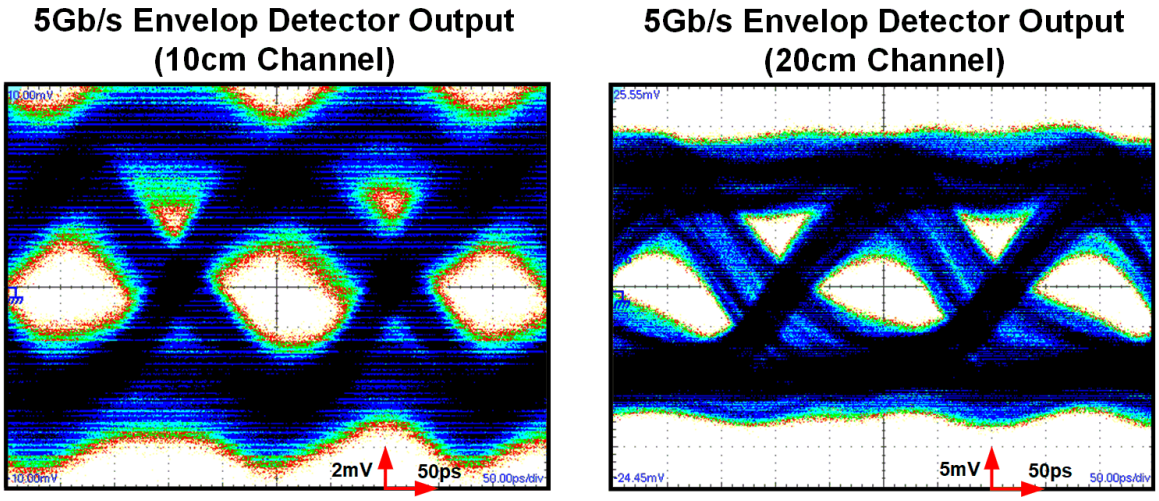

Figure 5.14: Measured 5Gb/s eye diagrams using buffered envelope-detector (ED) output in Fig. 5.9.

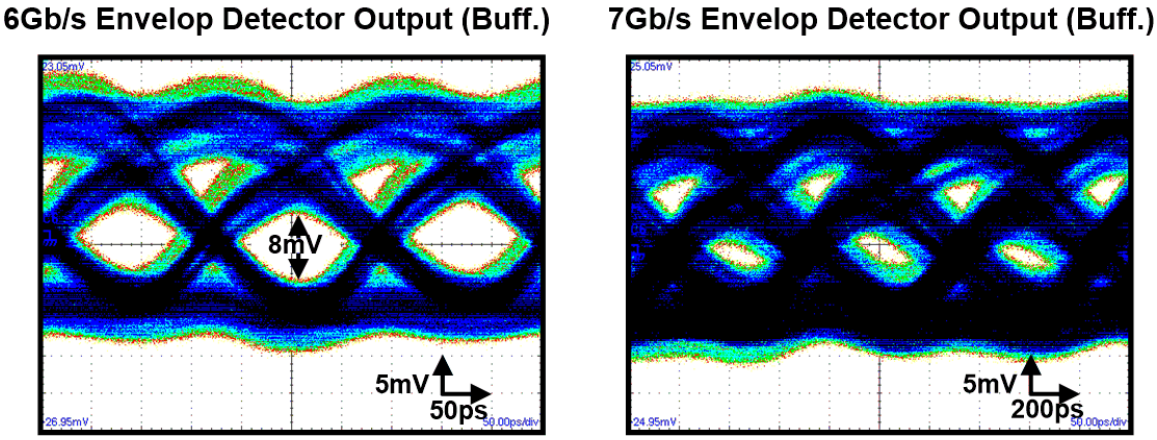

Figure 5.15: Measured 6Gb/s and 7Gb/s eye diagrams using buffered envelope-detector (ED) output in Fig. 5.9. Bandwidth is limited by bondwire from chip to PCB trace.

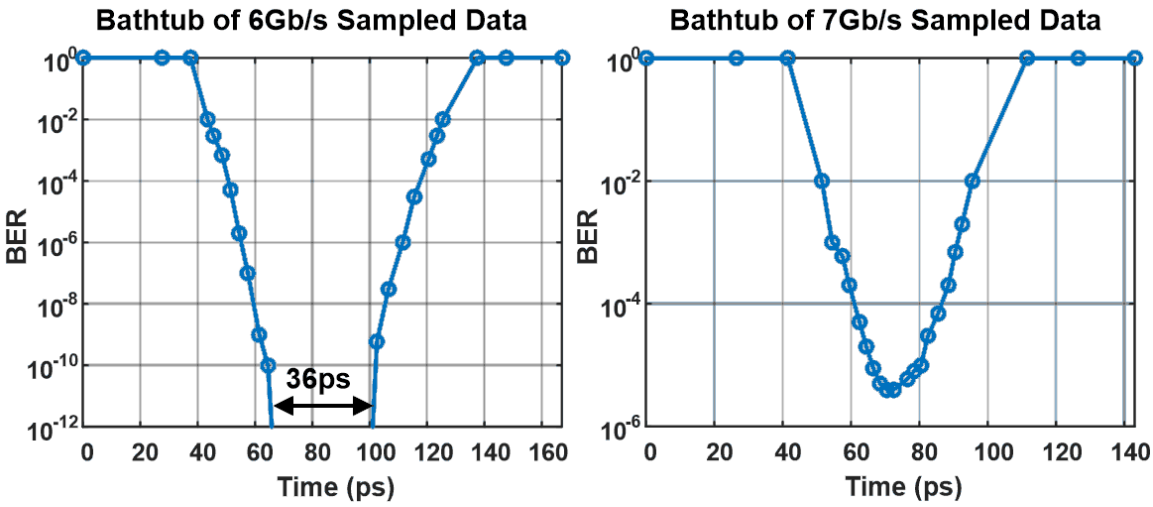

Figure 5.16: Measured bathtub curves at the internal sampler input for 6 Gb/s and 7 Gb/s data rates.

Table 5.1: Comparison of fully-integrated guided-link over SCW to state-of-the-art

	This Work	JSSC 2014	ISSCC 2015	JSSC 2011	ISSCC 2016
Technology	**65-nm CMOS**	32-nm SOI	40-nm CMOS	40-nm CMOS	14-nm CMOS
Area (mm^2)	**0.95(tot.)/ 0.77(Mod /Demod, TRX, Ant)**	4.62	0.48	0.21	9.6/38.4
Channel	**0.4 mm Bare Copper Single wire**	Air	2mm×1mm PTFE Tube	1mm×8mm PS Tube	Air
Coupling	**On-chip Radial Antenna**	On-chip Dipole	On-chip dipole (TX), bondwire ant.(RX)	Off-chip Quasi-Yagi	Capacitive
Freq./Mod.	**60-GHz OOK**	210-GHz OOK	120-GHz CPFSK	57-GHz OOK	NA
Data Rate/Range	**7 Gb/s @1e-5, 6 Gb/s @1e-12, 20 cm**	10 Gb/s (NA)	12.7 Gb/s, 1 m	15 Gb/s, 10 cm	8 Gb/s×4, 0.8 mm
Integration	**Serializer, TX, RX, Sampler, Deserializer, Clocking**	TX, RX	TX/RX	TX/RX	Serializer, TX/RX, Deserializer, Clocking
Power (mW)	**70.9 (total), 54 (Mod, TRX, Demod) @7Gb/s**	308	61	71	32×4
Efficiency (pJ/b)	**10.1 (total) / 7.7 (Mod, TRX, Demod) @7Gb/s**	30	4.8	4.7	4

Chapter 6: A CPFSK Guided mm-Wave Communication Link over Two-Metal-Wire Waveguide

6.1 Introduction to Guided mm-Wave Link over Two-Metal-Wire

The first demonstration of a fully-integrated end-to-end 7Gb/s 60GHz communication link over single-conductor-wire (SCW) waveguide utilizing Sommerfeld wave propagation is presented in chapter 5 [53]. Such guided mm-wave link over SCW can be a promising solution for achieving energy-efficient high data rate interconnects. But the Sommerfeld wave is weakly guided by the SCW and thus relatively sensitive to bending loss. The coupling between two SCWs also limits the multiplexing of multiple SCWs in parallel.

Investigation of other metal-wire waveguides that potentially support low-loss and relatively flat dispersion modes at mm-wave while providing better bend loss and lower coupling to adjacent channels is of great interest. Fig. 6.1 shows the overview of potential multi-lane mm-wave links over parallel two-metal-wire (TMW) waveguides. A two-metal-wire waveguide is consisting of two cylindrical metal wire with diameter d that are closely placed with spacing s in air. The electrical fields of the TEM model are mostly distributed in the air gap between the two wires. Fig. 6.1 shows the simulated electrical fields in the cross section of two-metal-wire and four-metal-wire waveguides. With the proper choice of wire diameter, wire spacing and the spacing between two-metal-wires, it is possible to configure such multi-lane two-metal-wire waveguides for achieving energy efficient high data-rate communications.

6.2 Design of CPFSK Guided mm-Wave Link over Two-Metal-Wire

Fig. 6.2(a) shows the simulated loss and group delay of the TEM model on an ideal two-metal-wire waveguide. The loss is limited by skin-effect and the dispersion is relative

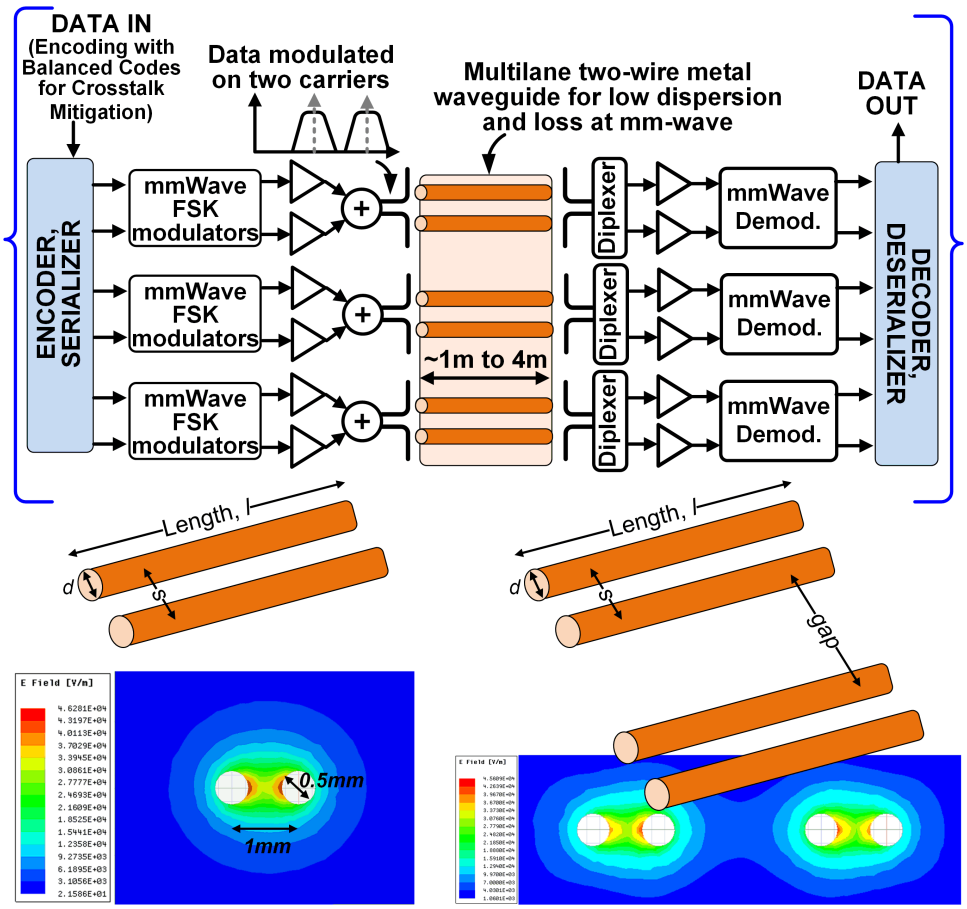

Figure 6.1: Overview of multi-lane mm-wave data link over parallel two-metal-wire waveguides.

flat since most of the electrical fields are guided in free space. Fig. 6.2(b) shows the simulated loss of a system with one dipole exciting the TEM mode and another dipole picking up the TEM mode from the 1m two-metal-wire waveguide.

The CPFSK modulation scheme is choose because the low complexity and non-coherent demodulation method available. The CPFSK modulation also allows possible concurrent communication in multi-lane two-metal-wire waveguides with offset frequencies. Fig. 6.3 shows the block diagram of the proposed 60GHz transceiver IC for the guided link over two-metal-wire waveguide. A high-speed multiplexer serializes incoming data generated from on-chip PRBS generator and drives a switch at the DCO cap

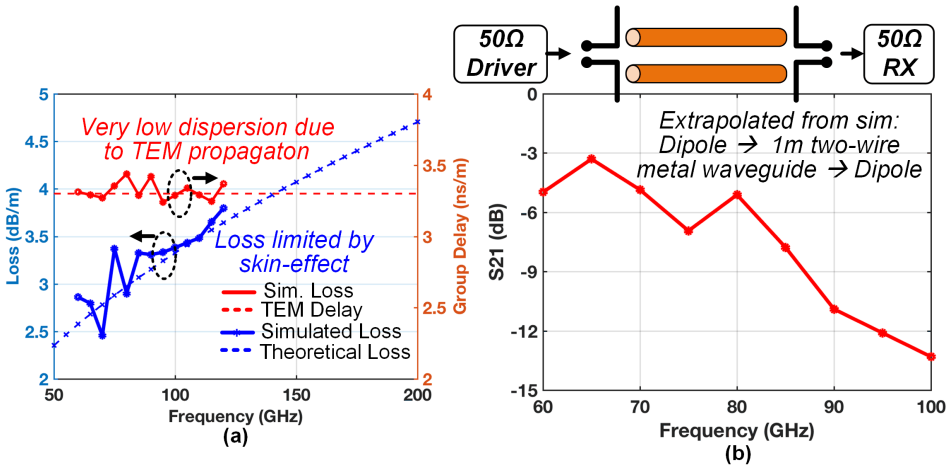

Figure 6.2: Simulated loss and group delay of the TEM model on two-metal-wire waveguide.

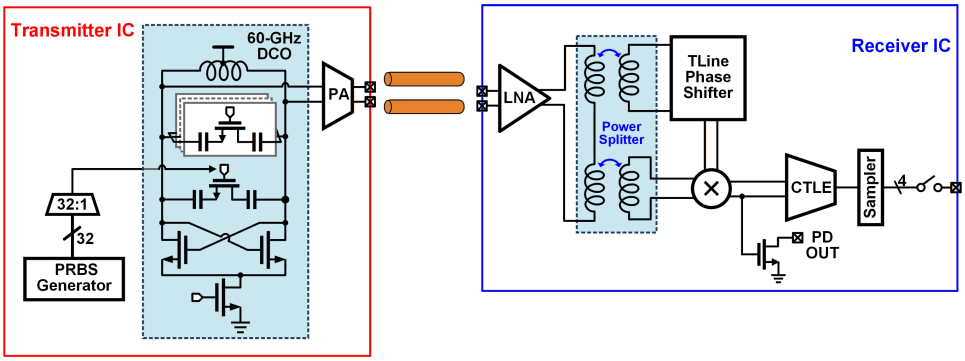

Figure 6.3: Block diagram of the proposed 60GHz transceiver IC with CPFSK modulation for achieving guided link over two-metal-wire waveguide.

bank to toggle the frequency of the DCO, thus generating CPFSK signal. The DCO output is send to a class-AB differential PA with cross-coupled capacitor for neutralization and the PA delivers 0dBm into the 100Ω differential impedance. On the RX, a six-stage wideband 60GHz LNA with low-k transformer matching network and cross-coupled capacitor neutralization amplifies the received signal. A transformer based power splitter split the signal into two parts, one directly goes to the input of the phase detector, the other one goes to a meander transmission line based phase shifter then goes to the other input of the phase detector. The transmission line based phase shifter creates frequency

dependent phase shifts and can convert the frequency information into phase information. The phase detector demodulate the CPFSK signal and drives a CTLE and then a demultiplexer and a sampler. The phase detector (PD) output also drives an open-drain buffer for direct measurement. The output of PA and the input of LNA are both using 100μm spacing GSGSG pads, enabling probe level test and guided link test with chip-on-board packaging.

6.3 Measurements of CPFSK Guided mm-Wave Link over Two-Metal-Wire

Fig. 6.4 shows the die photo of the 60GHz CPFSK transceiver occupying 1.17mm^2 implemented in 65nm CMOS and the corresponding PCB for guided link test. Two IC can be placed on each PCB using chip-on-board approach enabling possible two-lane two-metal-wire links. Table 6.1 shows the measured power consumption of the 60GHz CPFSK transceiver implemented in 65nm CMOS. The total power consumption of the transceiver is 73.3mW including mm-wave TX/RX, PRBS generator, Mux, Demux,CTLE and Sampler. Fig. 6.5 shows the measured PA output power and frequency tuning curve using probe level test. Such measurements shows the TX can generating CPFSK signal at 63.43GHz/57.57GHz and can be tuned up to 65.05GHz/58.71GHz with four-bits static switches. The power at lower frequency is $>$2dBm while the power at high frequency is slightly lower with $>$-5dBm.

In order to measured the channel loss of the proposed two-metal-wire waveguide, a wideband Marchand Balun is implemented on Rogers 4350B laminate (Fig. 6.6) and the single-ended port can be connectorized with a V-band end launcher for channel loss characterization using VNA. Fig. 6.6 also shows the measured performance of the Balun showing $\sim$178° phase difference of the differential port and $\sim$1dB gain mismatch between the differential port.

The loss of differential two-trace on Rogers 4350B is first characterized and the measurement result is shown in Fig. 6.7. Both ends of the differential two-trace are connected to VNA through a V-band connector, CPWG routing and the Marchand Balun.

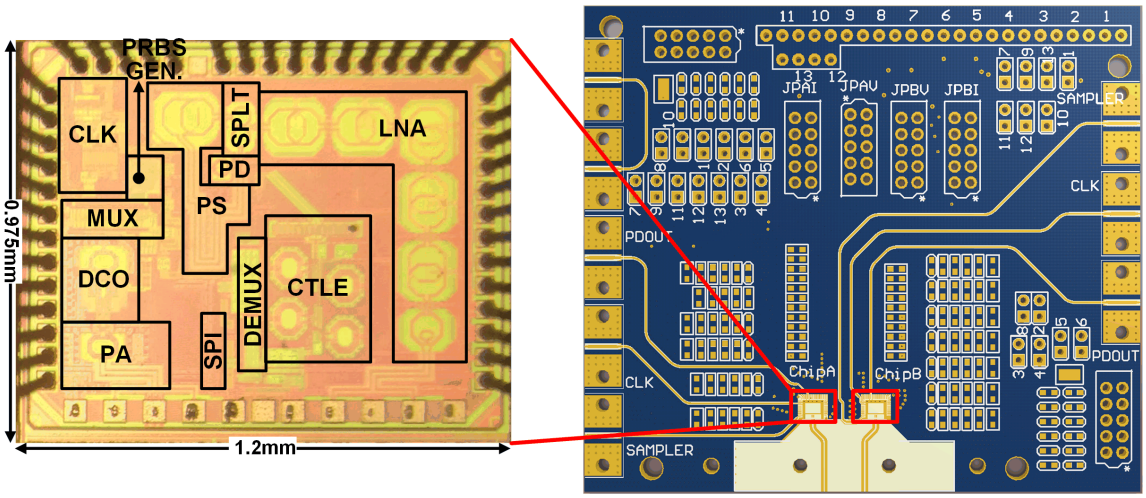

Figure 6.4: Die photograph of the proposed transceiver in 65nm CMOS and the corresponding PCB with option of two IC being packaged on board.

Table 6.1: Summary of measured power consumption of the 60GHz CPFSK transceiver.

	Power (mW)
PRBS Gen.	0.055
Mux	4.4
DCO	16.96
PA	7.06
LNA&PS	29.1
PD	3.059
CTLE	11.97
Demux & Sampler	0.64
mm-wave TX	24
mm-wave RX	32.2
Total	73.3

The measurements was repeated for different two-trace channels with various length. The loss of such differential two-trace on Rogers 4350B is about 0.9dB/cm at 60GHz.

The measured channel loss of the proposed two-metal-wire waveguide is shown in Fig. 6.8 and Fig. 6.9. The two-metal-wire waveguide can be fabricated using AWG copper wires with the similar method that are used to make ribbon cables. Without access to such method or tools, the two-metal-wire waveguide measured here is custom made

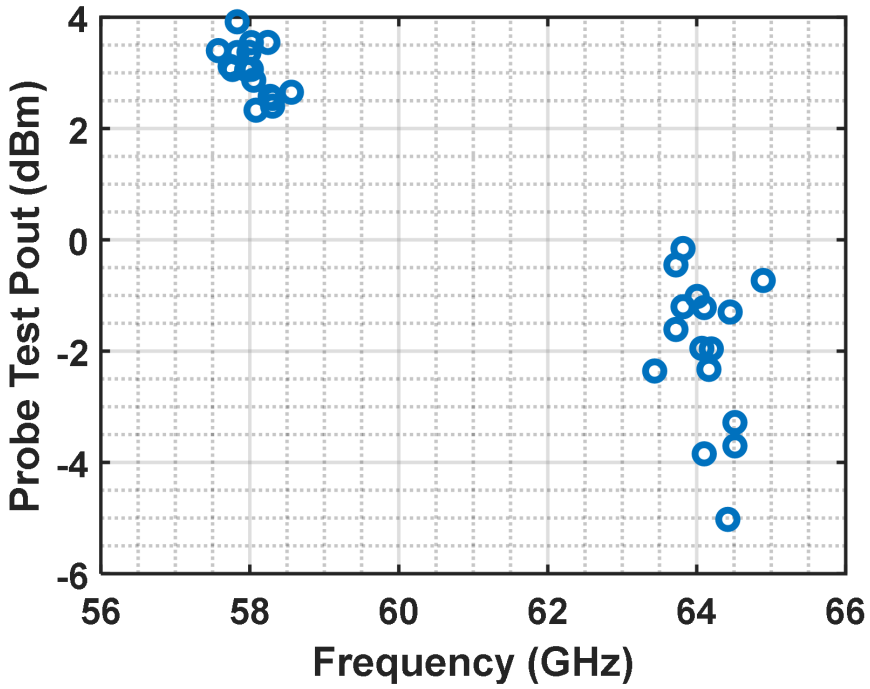

Figure 6.5: Measured PA output power and frequency tuning curve using probe test.

using the approach as following: A long Teflon tape is flip and fixed to the surface of a Styrofoam plate. Three copper wires with the same length L are fixed to the Teflon tape with no gap existing between the wires. The three copper wires used are AWG26 (16mil diameter), AWG31 (9mil diameter) and AWG26 (16mil diameter) respectively. Then the wire in the middle (AWG31) is removed thus creating a two-metal-wire waveguide with wire diameter 16mil and wire spacing 9mil. The electrical fields is expected to be distributed mostly in the 9mil air space between the two-metal-wire. Both ends of the custom-made two-metal-wire waveguide is connected to the differential two-trace on Rogers 4350B using custom made Teflon clip which mechanically press down the two-metal-wire with the two-trace. Then the two-trace was connected to VNA with the Marchand balun on Rogers 4350B and the V-band end launcher. Fig. 6.8 shows the measured loss of a 45cm two-metal-wire channel which is fully fixed to the Teflon tape. Such fully-fixed 45cm two-metal-wire channel has $\sim$13.6dB loss at 60GHz, cor-

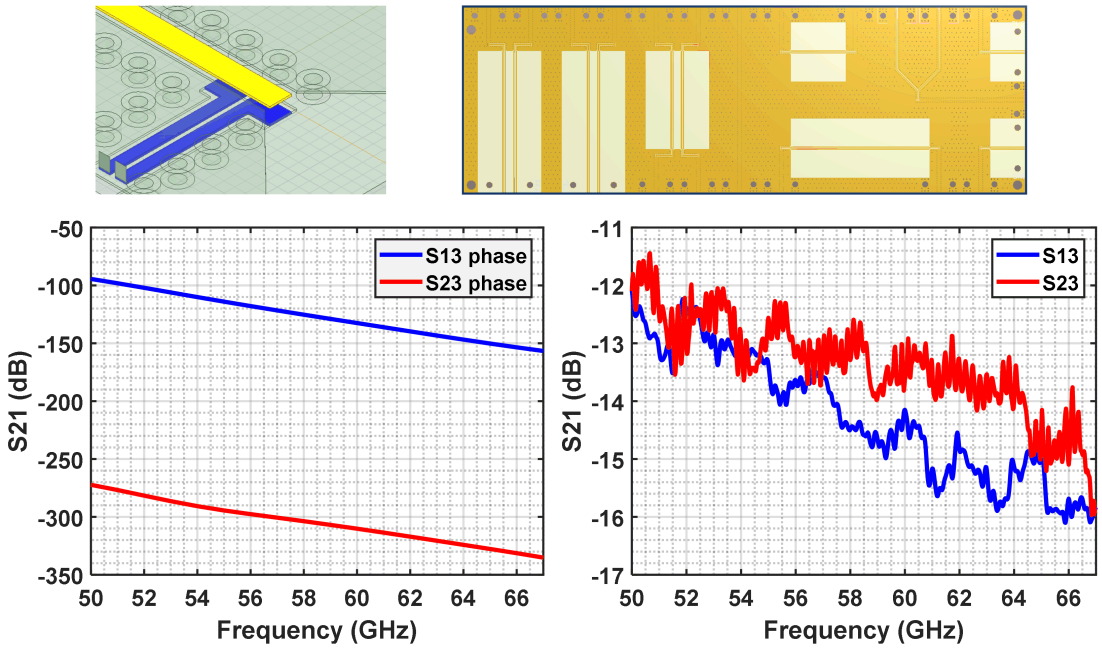

Figure 6.6: Wideband Marchand Balun implemented on Rogers 4350B laminate for channel loss characterization and measured performance of the Balun using VNA.

responding to ∼0.3dB/cm loss at 60GHz. This custom made channel is relative robust since multiple sets of measurements are performed on the same channel with 24 hours separation showing similar loss.

Fig. 6.9 shows the measured loss of a 60cm two-metal-wire channel which is partially fixed to the Teflon tape every 10cm in order to reduce the loss caused by the Teflon tape. Such partially-fixed 60cm two-metal-wire channel has 12.1dB loss at 60GHz, corresponding to ∼0.2dB/cm loss at 60GHz. Despite the lower loss comparing to the full-fixed version, the partially-fixed two-metal-wire waveguide is less robust over time because the wire spacing is potentially varying along the channel, which cause discontinuity, extra loss and loss variations.

The measured loss of custom made two-metal-wire waveguide is ∼0.2dB/cm at 60GHz, which is 4.5X smaller than the ∼0.9dB/cm loss of two-trace on Rogers 4350B laminate.

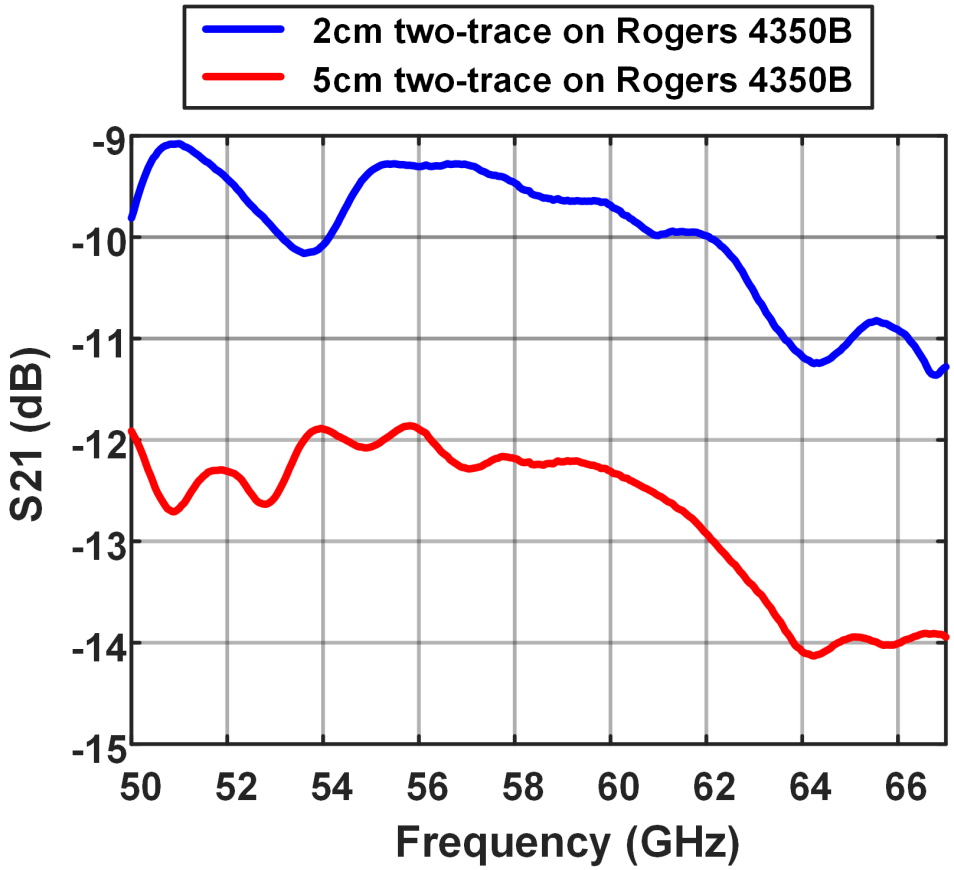

Figure 6.7: Measured channel loss of two-trace printed on Rogers 4350B.

6.4 Conclusion to Guided mm-Wave Link over Two-Metal-Wire

The two-metal-wire waveguide has the loss of ∼0.2dB/cm at 60GHz and is a promising low lost and relative flat dispersion channel that can potentially enable multi-lane energy efficient high data rate guided mm-wave links. Despite the low loss of such channel, it is extremely challenging to establish a robust link with good eye diagram and BER of $< 10^{-12}$ due to the limitation on measurements setup, the robustness of custom-made two-metal-wire waveguide and the coupling mechanism from the IC to the channel. The small section of two-trace on the IT-180TC PCB adds extra loss at both the TX and RX sides. The coupling mechanism from the IC to the channel we used on the measurements setup relies on the press-on contact of two-metal-wire with trace on PCB using

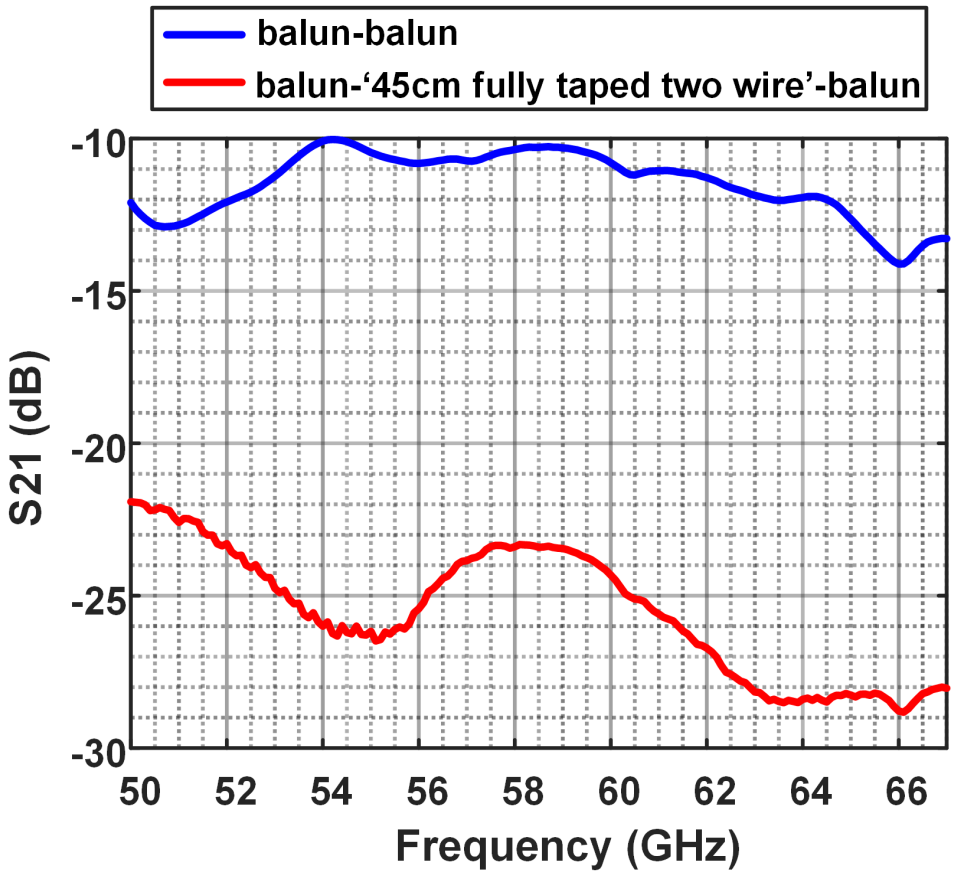

Figure 6.8: Measured channel loss of the proposed custom-made two-metal-wire waveguide with 45cm length.

Teflon tape. Such coupling mechanism is relatively ineffective and lack of robustness. The custom-made two-metal-wire channel also lack of robustness and is mechanically instable.

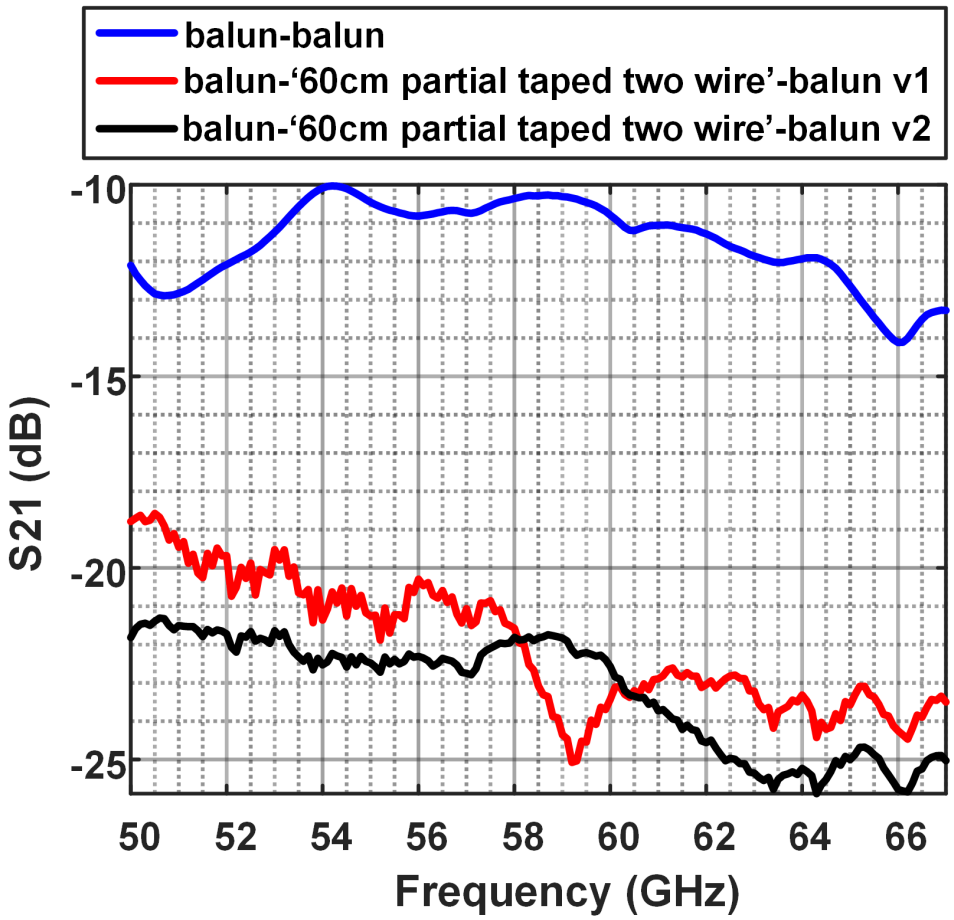

Figure 6.9: Measured channel loss of the proposed custom-made two-metal-wire waveguide with 60cm length.

Chapter 7: Conclusion

Spatial modulation or spatial shift keying is a promising technique to improve energy efficiency in relatively slowly-varying channels by leverage diversity of spatial parameters and embedding information in antennas switching or transmission directions switching. Such spatial modulation can be combined with frequency-shift keying in a low-power transceiver to further improve energy-efficiency of short-range mm-wave links. Low-power DCO based approach can provide pulsed FSK operation and phase shift through relative delay of DCO trigger signals. A two-element 68GHz FSK-SSK TX prototype is implemented in 65-nm CMOS and is packaged with aperture coupled patch antennas on PCB. The TX prototype demonstrates 3Gb/s data rates with 2-FSK and 4-SSK and achieves energy efficiency of 7.1pJ/bit and EIRP of 6dBm [4]. Low-power mm-wave two-element RX with capability to demodulate both FSK and SSK for short-range FSK-SSK links are implemented in 65nm CMOS using both series-FSK-SSK and parallel-FSK-SSK demodulation techniques. An end-to-end 68GHz FSK-SSK link operating at 2Gb/s data rates (1Gb/s FSK and 1Gb/s SSK) over 6cm reflective channel with integrated CMOS TX and RX demonstrating the first SSK-FSK link [39]. Such link demonstration shows the feasibility of using SSK in addition to other energy-efficient modulation schemes to improve overall energy efficiency of short range wireless links. Possible future work includes building large scale spatial modulation MIMO systems of N-element TX and N-element RX with the benefits of higher EIRP (longer link range), higher spatial resolutions and higher spatial modulation depth; Including energy efficient power amplifier capable of multi-Gb/s pulsed operation in the SSK TX in order to increase the link range; Combining spatial modulation with higher-order FSK or code domain modulation [16] to further increase the data rates of the link.

Single-metal-wire or multi-metal-wires waveguides with low loss and relative flat dispersion modes are promising channels for achieving energy efficient high data rate guided mm-wave links. The first demonstration of a mm-wave data link using Sommerfeld-

wave propagation on a single conductor wire is presented. A fully-integrated end-to-end prototype implemented in 65nm CMOS is presented to demonstrate the feasibility of energy-efficient high data rate guided mm-wave links over the single conductor wire. Such prototype achieves 7 Gb/s data rate over 20-cm single wire channel length with energy efficiency of $\sim$10 pJ/bit [53]. The two-metal-wire waveguide also has the low loss that are measured to be $\sim$0.2dB/cm at 60GHz and relative flat group delays. A 60GHz CPFSK transceiver is implemented in 65nm CMOS as a prototype to potentially enable energy-efficient high data rates guided mm-wave links over two-metal-wire and multi-lane two-metal-wire waveguides. Possible future work includes achieving higher data rates over single conductor wire by (a) increasing carrier frequency, (b) improving PA output power and LNA gain to accommodate coupling loss due to non-idealities, (c) improving the mechanical mechanism to support single conductor wire extended to longer channel length. Further investigation of multi-lane two-metal-wire guided links by optimizing the coupling loss from IC to two-metal-wire waveguide and improving robustness of the channel is also promising.

Power amplifier (PA) is the vital part in a millimeter-wave beamsteering systems and PA with high output power is essential for increasing link range and compensating signal path loss especially at mm-wave. Improving the energy efficiency of PA while maintaining the output power level and linearity has the most significant impact on improving the overall transceiver energy efficiency. Possible future work includes designing energy efficient high linearity and high output power PA and particularly using such PA in a mm-wave beamsteering systems with reduced hardware complexity by taking advantage of lens antenna sub-array [54].

Bibliography

[1] G. Wang, K. Zhan, T. Kamgaing, R. Khanna, H. Liu, and A. Natarajan, "Measurement-based channel modeling for mmWave wireless links in enclosed server platforms," in *IEEE Radio and Wireless Symposium (RWS)*, Jan. 2017, pp. 141–143.

[2] M. Di Renzo, H. Haas, A. Ghrayeb, S. Sugiura, and L. Hanzo, "Spatial modulation for generalized MIMO: Challenges, opportunities, and implementation," *Proceedings of the IEEE*, vol. 102, no. 1, pp. 56–103, Jan. 2014.

[3] A. Tork and A. Natarajan, "Reconfigurable X-band 4×4 Butler array in 32nm CMOS SOI for angle-reject arrays," in *IEEE MTT-S International Microwave Symposium (IMS)*, May 2016, pp. 1–4.

[4] K. Zhan, J. Kang, G. Wang, T. Kamgaing, R. Khanna, G. Dogiamis, H. Liu, and A. Natarajan, "A low-power FSK/spatial modulation transmitter for mm-wave wireless links," in *IEEE MTT-S International Microwave Symposium (IMS)*, Jun. 2017.

[5] X. Yu, H. Rashtian, S. Mirabbasi, P. P. Pande, and D. Heo, "An 18.7-Gb/s 60-GHz OOK demodulator in 65-nm CMOS for wireless network-on-chip," *IEEE Transactions on Circuits and Systems I: Regular Papers*, vol. 62, no. 3, pp. 799–806, Mar. 2015.

[6] N. Dolatsha, C. Chen, and A. Arbabian, "Loss and dispersion limitations in mm-wave dielectric waveguides for high-speed links," *IEEE Transactions on Terahertz Science and Technology*, vol. 6, no. 4, pp. 637–640, Jul. 2016.

[7] M. Wåchter, M. Nagel, and H. Kurz, "Frequency-dependent characterization of THz Sommerfeld wave propagation on single-wires," *Optics Express*, vol. 13, no. 26, pp. 10 815–10 822, Dec 2005. [Online]. Available: http://www.opticsexpress.org/abstract.cfm?URI=oe-13-26-10815

[8] S. Vashi, J. Ram, J. Modi, S. Verma, and C. Prakash, "Internet of things (IoT): A vision, architectural elements, and security issues," in *International Conference on I-SMAC (IoT in Social, Mobile, Analytics and Cloud)*, 2017.

[9] T. S. Rappaport, Y. Xing, G. R. MacCartney, A. F. Molisch, E. Mellios, and J. Zhang, "Overview of millimeter wave communications for fifth-generation (5G) wireless networks—with a focus on propagation models," *IEEE Transactions on Antennas and Propagation*, vol. 65, no. 12, pp. 6213–6230, Dec. 2017.

[10] D. S. Linthicum, "Making sense of AI in public clouds," *IEEE Cloud Computing*, vol. 4, no. 6, pp. 70–72, Nov. 2017.

[11] K. Kibaroglu, M. Sayginer, and G. M. Rebeiz, "A low-cost scalable 32-element 28-GHz phased array transceiver for 5G communication links based on a 2×2 beamformer flip-chip unit cell," *IEEE Journal of Solid-State Circuits*, vol. 53, no. 5, pp. 1260–1274, May 2018.

[12] D. Guermandi, Q. Shi, A. Dewilde, V. Derudder, U. Ahmad, A. Spagnolo, I. Ocket, A. Bourdoux, P. Wambacq, J. Craninckx, and W. Van Thillo, "A 79-GHz 2×2 MIMO PMCW radar SoC in 28-nm CMOS," *IEEE Journal of Solid-State Circuits*, vol. 52, no. 10, pp. 2613–2626, Oct. 2017.

[13] "IEEE standard for information technology–telecommunications and information exchange between systems–local and metropolitan area networks–specific requirements-part 11: Wireless LAN medium access control (MAC) and physical layer (PHY) specifications amendment 3: Enhancements for very high throughput in the 60 GHz band," *as amended by IEEE Std 802.11ae-2012 and IEEE Std 802.11aa-2012) IEEE Std 802.11ad-2012 (Amendment to IEEE Std 802.11-2012*, pp. 1–628, Dec. 2012.

[14] Y. Ghasempour, C. R. C. M. da Silva, C. Cordeiro, and E. W. Knightly, "IEEE 802.11ay: Next-generation 60 GHz communication for 100 Gb/s Wi-Fi," *IEEE Communications Magazine*, vol. 55, no. 12, pp. 186–192, Dec. 2017.

[15] P. Zhou, K. Cheng, X. Han, X. Fang, Y. Fang, R. He, Y. Long, and Y. Liu, "IEEE 802.11ay-based mmwave WLANs: Design challenges and solutions," *IEEE Communications Surveys Tutorials*, vol. 20, no. 3, pp. 1654–1681, 2018.

[16] M. Johnson, A. Dascurcu, K. Zhan, A. Galioglu, N. Adepu, S. Jain, H. Karishnaswamy, and A. Natarajan, "A 4-element 28GHz millimeter-wave MIMO array with single-wire interface using code-domain multiplexing in 65nm CMOS," in *IEEE Radio Frequency Integrated Circuits Symposium (RFIC)*, 2019.

[17] Z. Wang, P. Y. Chiang, P. Nazari, C. C. Wang, Z. Chen, and P. Heydari, "A CMOS 210-GHz fundamental transceiver with OOK modulation," *IEEE Journal of Solid-State Circuits*, vol. 49, no. 3, pp. 564–580, Mar. 2014.

[18] C. W. Byeon, C. H. Yoon, and C. S. Park, "A 67-mW 10.7-Gb/s 60-GHz OOK CMOS transceiver for short-range wireless communications," *IEEE Transactions on Microwave Theory and Techniques*, vol. 61, no. 9, pp. 3391–3401, Sep. 2013.

[19] F. Zhu, W. Hong, W. Liang, J. Chen, X. Jiang, P. Yan, and K. Wu, "A low-power low-cost 45-GHz OOK transceiver system in 90-nm CMOS for multi-Gb/s transmission," *IEEE Transactions on Microwave Theory and Techniques*, vol. 62, no. 9, pp. 2105–2117, Sep. 2014.

[20] K. Kawasaki, Y. Akiyama, K. Komori, M. Uno, H. Takeuchi, T. Itagaki, Y. Hino, Y. Kawasaki, K. Ito, and A. Hajimiri, "A millimeter-wave intra-connect solution," in *International Solid-State Circuits Conference (ISSCC)*, Feb. 2010, pp. 414–415.

[21] H. Wang, M. H. Hung, Y. C. Yeh, and J. Lee, "A 60-GHz FSK transceiver with automatically-calibrated demodulator in 90-nm CMOS," in *Proc. Symp. VLSI Circuits*, Jun. 2010, pp. 95–96.

[22] W. Volkaerts, N. V. Thienen, and P. Reynaert, "An FSK plastic waveguide communication link in 40nm CMOS," in *IEEE International Solid-State Circuits Conference (ISSCC)*, Feb. 2015, pp. 1–3.

[23] A. Arbabian, S. Callender, S. Kang, M. Rangwala, and A. M. Niknejad, "A 94 GHz mm-Wave-to-baseband pulsed-radar transceiver with applications in imaging and gesture recognition," *IEEE Journal of Solid-State Circuits*, vol. 48, no. 4, pp. 1055–1071, Apr. 2013.

[24] B. P. Ginsburg, S. M. Ramaswamy, V. Rentala, E. Seok, S. Sankaran, and B. Haroun, "A 160 GHz pulsed radar transceiver in 65 nm CMOS," *IEEE Journal of Solid-State Circuits*, vol. 49, no. 4, pp. 984–995, Apr. 2014.

[25] S. Fukuda, Y. Hino, S. Ohashi, T. Takeda, H. Yamagishi, S. Shinke, K. Komori, M. Uno, Y. Akiyama, K. Kawasaki, and A. Hajimiri, "A 12.5+12.5 Gb/s full-duplex plastic waveguide interconnect," *IEEE Journal of Solid-State Circuits*, vol. 46, no. 12, pp. 3113–3125, Dec. 2011.

[26] K. Wang and D. M. Mittleman, "Metal wires for terahertz wave guiding," *Nature*, vol. 432, no. 7015, pp. 376–379, Nov. 2004.

[27] J. S. Jo, T. Jeon, and D. R. Grischkowsky, "Prototype 250 GHz bandwidth chip to chip electrical interconnect, characterized with ultrafast optoelectronics," *IEEE Transactions on Terahertz Science and Technology*, vol. 3, no. 4, pp. 453–460, Jul. 2013.

[28] L. Kong and E. Alon, "A 21.5mW 10+Gb/s mm-wave phased-array transmitter in 65nm CMOS," in *Symposium on VLSI Circuits (VLSIC)*, Jun. 2012, pp. 52–53.

[29] Y. Wang, Y. Liu, A. Agrawal, and A. Natarajan, "A 74.6GHz–83.6GHz digitally controlled oscillator with 370kHz frequency resolution in 65nm CMOS," in *IEEE Radio and Wireless Symposium (RWS)*, Jan. 2016, pp. 176–178.

[30] T. LaRocca, J. Liu, F. Wang, D. Murphy, and F. Chang, "CMOS digital controlled oscillator with embedded DiCAD resonator for 58-64GHz linear frequency tuning and low phase noise," in *IEEE MTT-S International Microwave Symposium (IMS)*, Jun. 2009, pp. 685–688.

[31] J. Kang, C. Patrick, and A. Natarajan, "A 3.6 cm^2 wirelessly-powered UWB SoC with -30.7 dBm rectifier sensitivity and sub-10cm range resolution," in *IEEE Radio Frequency Integrated Circuits Symposium (RFIC)*, Jun. 2015, pp. 255–258.

[32] G. Liu, A. Trasser, A. Çağri Ulusoy, and H. Schumacher, "Low-loss, low-cost, IC-to-board bondwire interconnects for millimeter-wave applications," in *IEEE MTT-S International Microwave Symposium (IMS)*, Jun. 2011, pp. 1–4.

[33] Y. Liu and A. Natarajan, "Millimeter-wave IC-antenna cointegration for integrated transmitters and receivers," *IEEE Antennas and Wireless Propagation Letters*, vol. 15, p. 1848–1852, March 2016.

[34] Y. Liu and A. Natarajan, "60 GHz concurrent dual-polarization RX front-end in SiGe with antenna-IC co-integration," in *IEEE Bipolar/BiCMOS Circuits and Technology Meeting (BCTM)*, Oct. 2017, pp. 42–45.

[35] Y. Liu and A. Natarajan, "A 60 GHz polarization-Duplex TX/RX front-end with dual-Pol antenna-IC co-integration in SiGe BiCMOS," in *IEEE Radio Frequency Integrated Circuits Symposium (RFIC)*, June 2019.

[36] Y. Liu, "IC-antenna co-integration for efficient and scalable millimeter-wave antenna interfaces," Ph.D. dissertation, Oregon State University, 2019.

[37] H. Lee, J. G. Lee, C. J. Lee, C. S. Park, and H. J. Kim, "An 20-Gb/s W-band OOK CMOS receiver for high-speed wireless interconnect," *IEEE Microwave and Wireless Components Letters*, vol. 26, no. 10, pp. 840–842, Oct. 2016.

[38] N. Van Thienen, Y. Zhang, M. De Wit, and P. Reynaert, "An 18Gbps polymer microwave fiber (PMF) communication link in 40nm CMOS," in *Proc. ESSCIRC Conf. 2016: 42nd European Solid-State Circuits Conf*, Sep. 2016, pp. 483–486.

[39] K. Zhan, Y. Liu, T. Kamgaing, R. Khanna, G. Dogiamis, H. Liu, and A. Natarajan, "A low-power FSK/spatial modulation receiver for short-range mm-wave wireless links," in *IEEE MTT-S International Microwave Symposium (IMS)*, 2019.

[40] E. Cohen, O. Degani, and D. Ritter, "A wideband gain-boosting 8mW LNA with 23dB gain and 4dB NF in 65nm CMOS process for 60 GHz applications," in *IEEE Radio Frequency Integrated Circuits Symposium (RFIC)*, Jun. 2012, pp. 207–210.

[41] J. Kang, S. Rao, P. Chiang, and A. Natarajan, "Area-constrained wirelessly-powered UWB SoC design for small insect localization," in *IEEE Topical Conference on Wireless Sensors and Sensor Networks (WiSNet)*, Jan. 2016, pp. 18–20.

[42] K. R. Sadagopan, J. Kang, Y. Ramadass, and A. Natarajan, "A 960pW co-integrated-antenna wireless energy harvester for WiFi backchannel wireless powering," in *IEEE International Solid-State Circuits Conference (ISSCC)*, Feb. 2018, pp. 136–138.

[43] J. Kang, S. Rao, P. Chiang, and A. Natarajan, "Design and optimization of area-constrained wirelessly powered CMOS UWB SoC for localization applications," *IEEE Transactions on Microwave Theory and Techniques*, vol. 64, no. 4, pp. 1042–1054, April 2016.

[44] K. R. Sadagopan, J. Kang, Y. Ramadass, and A. Natarajan, "A cm-scale 2.4-GHz wireless energy harvester with nanowatt boost converter and antenna-rectifier resonance for WiFi powering of sensor nodes," *IEEE Journal of Solid-State Circuits*, vol. 53, no. 12, pp. 3396–3406, Dec 2018.

[45] J. Kang, P. Chiang, and A. Natarajan, "A 1.2 cm^2 2.4 GHz self-oscillating rectifier-antenna achieving -34.5 dBm sensitivity for wirelessly powered sensors," in *IEEE International Solid-State Circuits Conference (ISSCC)*, Jan. 2016, pp. 374–375.

[46] K. R. Sadagopan, J. Kang, S. Jain, Y. Ramadass, and A. Natarajan, "A 365nW -61.5 dBm sensitivity 1.875 cm^2 2.4 GHz wake-up receiver with rectifier-antenna

co-design for passive gain," in *IEEE Radio Frequency Integrated Circuits Symposium (RFIC)*, June 2017, pp. 180–183.

[47] K. R. Sadagopan, J. Kang, and A. Natarajan, "Education session 4 - low power IoT wireless powering for ultra low power batteryless IoT sensing and communication," in *IEEE Custom Integrated Circuits Conference (CICC)*, April 2018, pp. 1–40.

[48] J. Kang, "Wirelessly powered cm-scale sensor for small insect localization application," PhD dissertation, School of Electrical Engineering and Computer Science, Oregon State University, 2018.

[49] J. Kang, P. Chiang, and A. Natarajan, "Bootstrapped rectifier-antenna co-integration for increased sensitivity in wirelessly-powered sensors," *IEEE Transactions on Microwave Theory and Techniques*, vol. 66, no. 11, pp. 5031–5041, Nov 2018.

[50] C. Thakkar, S. Sen, J. E. Jaussi, and B. Casper, "A 32Gb/s bidirectional 4-channel 4pJ/b capacitively coupled link in 14nm CMOS for proximity communication," in *International Solid-State Circuits Conference (ISSCC)*, Jan. 2016, pp. 400–401.

[51] N. Van Thienen, W. Volkaerts, and P. Reynaert, "A multi-Gigabit CPFSK polymer microwave fiber communication link in 40 nm CMOS," *IEEE Journal of Solid-State Circuits*, vol. 51, no. 8, pp. 1952–1958, Aug. 2016.

[52] M. King and J. Wiltse, "Surface-wave propagation on coated or uncoated metal wires at millimeter wavelengths," *IRE Transactions on Antennas and Propagation*, vol. 10, no. 3, pp. 246–254, May 1962.

[53] K. Zhan, A. Agrawal, M. Johnson, A. Ramachandran, T. Anand, and A. Natarajan, "An integrated 7-Gb/s 60-GHz communication link over single conductor wire using Sommerfeld wave propagation in 65-nm CMOS," in *IEEE MTT-S International Microwave Symposium (IMS)*, Jun. 2017, pp. 797–800.

[54] G. Mumcu, M. Kacar, and J. Mendoza, "Mm-wave beam steering antenna with reduced hardware complexity using lens antenna subarrays," *IEEE Antennas and Wireless Propagation Letters*, vol. 17, no. 9, pp. 1603–1607, Sep. 2018.